Symmetry, Hierarchy, and an Alternative Paradigm for Analyzing Neutrino Oscillations

By

Bernadette Kafwimbi Cogswell

Dissertation
Submitted to the Faculty of the
Graduate School of Vanderbilt University
in partial fulfillment of the requirements
for the degree of
DOCTOR OF PHILOSOPHY
in
Physics
December, 2014
Nashville, Tennessee

Approved:
David J. Ernst, Ph.D.
Paul D. Sheldon, Ph.D.
Sait A. Umar, Ph.D.
M. Shane Hutson, Ph.D.

TABLE OF CONTENTS

Page

Appendix

LIST OF TABLES

Table Page

LIST OF FIGURES

CHAPTER I

REVIEW OF NEUTRINO OSCILLATIONS

In this chapter we review the current standard three-flavor neutrino oscillation paradigm and the experimental data used to extract phenomenological parameters as well as the remaining open phenomenological questions in three-neutrino oscillation physics.

Modeling Neutrino Oscillations

We begin with a review of the standard three active flavor neutrinos paradigm.

Core Physics

For now, we focus on the core physics concepts that define the standard neutrino oscillation picture, relegating the more mathematically intensive discussions to the two following chapters devoted to expanding this standard framework.

Vacuum Oscillations

It has been shown mathematically and verified experimentally that the weak neutrino flavor states are linear combinations of neutrino mass eigenstates (see [1], [2]). For the observed number of neutrino flavors v_α ($\alpha = e, \mu, \tau$) comprised of three mass eigenstates m_j (j = 1, 2, 3), this relationship can be expressed in the neutrino flavor basis by

$$| \nu_\alpha(0) \rangle = \sum_{j=1}^{3} U_{\alpha j}^{*} \left|m_j\right\rangle , \quad \alpha = e, \mu, \tau \tag{1}$$

where U is a unitary matrix that mixes states [3]

$$U = \begin{pmatrix} c_{13}c_{12} & s_{12}c_{13} & s_{13}e^{-i\delta} \\ -s_{12}c_{23} - s_{23}s_{13}c_{12}e^{i\delta} & c_{23}c_{12} - s_{23}s_{13}s_{12}e^{i\delta} & s_{23}c_{13} \\ s_{23}s_{12} - s_{13}c_{23}c_{12}e^{i\delta} & -s_{23}c_{12} - s_{13}s_{12}c_{23}e^{i\delta} & c_{23}c_{13} \end{pmatrix} \tag{2}$$

where $c_{jk} \equiv \cos\theta_{jk}$ and $s_{jk} \equiv \sin\theta_{jk}$ with mixing angles θ_{jk} between mass eigenstates j and k, and δ is a possible CP-violating phase. Neutrino oscillations result from the quantum mechanical mixing of mass eigenstates as neutrinos propagate [3]. If the neutrino propagates, then the initial neutrino flavor state given by Eq. (1) will evolve into the flavor state ν_β ($\beta = e, \mu, \tau$)

$$\left| \nu_\beta(\vec{L}, t) \right\rangle = e^{-i(p_0 t - \vec{p}\cdot\vec{L})} | \nu_\alpha(0) \rangle , \quad \alpha, \beta = e, \mu, \tau \tag{3}$$

where $\vec{L}$ is the distance travelled by the neutrino, t is the time of propagation, and $\overrightarrow{p} = \left(p_0, \vec{p}\right) = (E_j , \overrightarrow{p_j})$ is the relativistic energy-momentum four vector.

Two standard approximations are used to calculate the above expression: (1) treat the neutrinos as relativistic, assume the same momentum for all mass eigenstates, $p_j \equiv p \approx E$, and the neutrino propagation time and distance are equivalent, $t \approx L$; and (2) expand the energies in Eq. (3) using

$$E_j = \sqrt{p^2 + m_j^2} \approx p\left(1 + \frac{m_j^2}{2p^2}\right) \tag{4}$$

so that the exponential phase becomes

$$E_j\, t - p_j L \approx \left(E_j - p_j\right) L \approx -\frac{m_j^2}{2E} L \tag{5}$$

Combining the above framework gives the exact vacuum oscillation probability $P_{\alpha\beta}$ between any two flavor states α and β

$$P_{\alpha\beta} = \left|\langle \nu_\beta (\vec{L}) \mid \nu_\alpha(0) \rangle\right|^2 \tag{6}$$

$$P_{\alpha\beta} = \delta_{\alpha\beta} + 2\sum_{j>k} \mathrm{Re}\left[U_{\beta j}U^*_{\alpha j}U^*_{\beta k}U_{\alpha k}\left(e^{-i\frac{\Delta m^2_{jk}}{2E}L} - 1\right)\right]. \tag{7}$$

Eq. (7) contains all the necessary information to calculate the oscillation probability between any two (anti)neutrino flavor states.

Eq. (7) shows that the oscillation probability depends on five independent oscillation parameters known as the mixing parameters: three mixing angles θ_{jk} and two mass-squared differences Δm^2_{jk} , where the third mass-squared difference is determined via the relation $\Delta m^2_{ik} = \Delta m^2_{ij} + \Delta m^2_{jk}$. A dependence on a sixth independent parameter, the *CP*-violating phase δ_{CP}, may also exist. Eq. (7) also shows that the oscillation probability depends on two physical parameters: the baseline length L between the neutrino creation and detection points and the neutrino energy E. The hallmark of the existence of neutrino oscillations is this baseline and neutrino energy dependence of the neutrino survival and oscillation probabilities.

Since the oscillation probability depends on the mass-squared differences, rather than the absolute masses of the neutrino mass eigenstates, determining the values of Δm^2_{21} (commonly known as the solar mass scale) and Δm^2_{32} (commonly known as the atmospheric mass scale) does not indicate whether state m_1 or m_3 is the absolute largest or smallest. However, only two possibilities exist, see Figure 1: (1) the case where m_1 is the lightest mass state known as the normal hierarchy, or (2) the case where m_3 is the lightest mass state known as the inverse hierarchy. Since the mass-squared differences appear as phases in the oscillation probability the fundamental hallmark of hierarchy effects is a change in the nature of the interference effects between the two mass scales on the oscillation probability. In vacuum these differences are quite small.

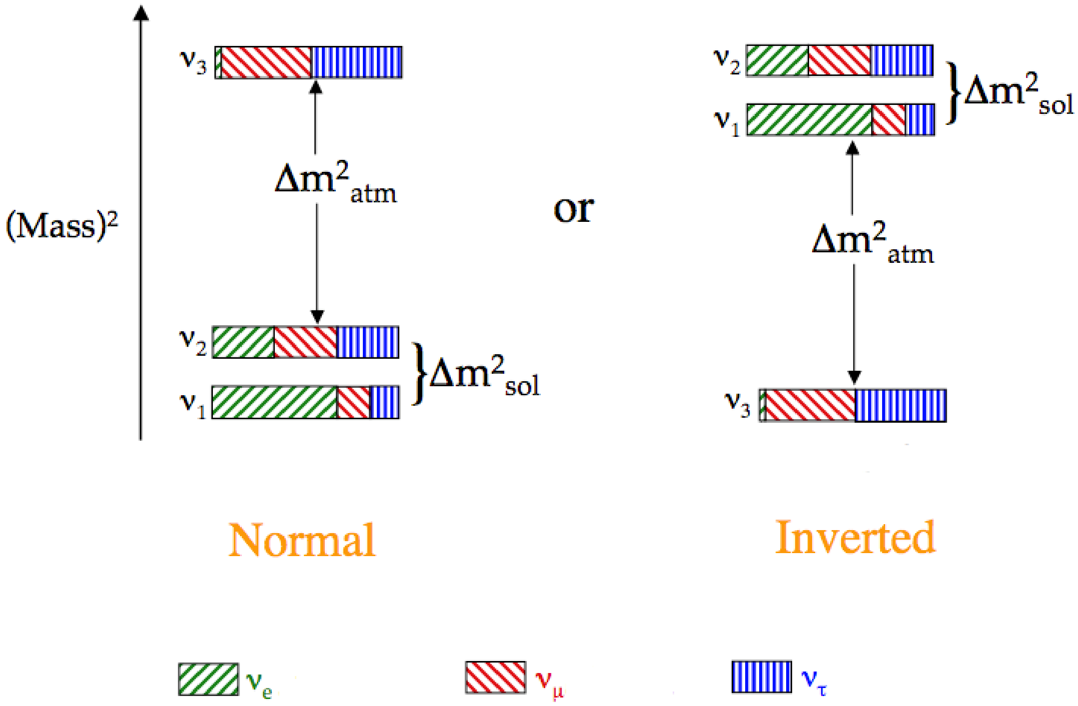

Figure 1. Two possible neutrino mass hierarchies in the standard three-flavor picture. Adapted from: B. Kayser [4].

CP-Violation

The most general $N \times N$ Dirac mixing matrix is a unitary matrix whose elements can be complex and that can be written as a product of three rotation matrices U_{ij} [3]. In the case of *CP*-conservation the elements of U are all real. Then, to be physical, U must be an orthogonal matrix, which means it contains real independent parameters. For three neutrino generations this translates into a 3 × 3 orthogonal matrix that depends on three real mixing angles, one mixing angle for each rotation plane. In the case of *CP*-violation the elements of U can be complex. This means U can also depend on complex phases, as well as the three real mixing angles. Not all of these phases are physically meaningful, i.e., most of these phases can be written away by a re-phasing of the neutrino fields which leaves the standard model interactions unchanged and, hence, these phases are not observable. However, the complex phase rewriting must satisfy certain mathematical constraints. As a result, for three neutrino generations, after re-phasing, there remains one possible physically observable *CP*-phase, which in the standard parameterization is usually included in the mixing matrix by being attached to the 1-3 mixing sector. Should it exist, the primary hallmark of neutrino *CP*-violation would be an asymmetry between the neutrino and antineutrino probabilities, which would no longer be equivalent due to the existence of a non-zero, complex *CP*-phase. A secondary hallmark of *CP*-violation would be a modulation of the amplitude of the oscillation probability via *CP* terms appearing in the flavor survival and conversion probabilities.

Matter Oscillations

Neutrino oscillations can be enhanced or suppressed by coherent forward scattering as neutrinos pass through matter (see [5], [6]). These matter effects can be included in the oscillation theory by adding a matter potential V to the diagonalized vacuum Hamiltonian H_{vac} to obtain the neutrino Hamiltonian in matter H_{matter}. For example, for electron neutrinos

$$H_{matter} = UH_{vac}U^{\dagger} + V \tag{8}$$

where

$$V = \sqrt{2}G_F n_e \tag{9}$$

G_F is the Fermi constant and n_e is the electron density of the medium in which the neutrinos propagate. Diagonalizing the matter Hamiltonian yields a new mixing matrix that contains the effective matter mixing angles and effective matter mass-squared differences. For a constant matter density, the resulting matter oscillation probability retains the exact form expressed in Eq. (7), but with the mixing angles and mass-squared differences replaced by effective values in matter. Again, all matter (anti)neutrino oscillation probabilities can be calculated from the general form in Eq. (7). To obtain the antineutrino oscillation probabilities in matter, the additional change of $V \rightarrow -V$ must also be made in Eqs. (8) and (9).

Neutrinos can interact with matter via charged current (CC) interactions, neutral current (NC) interactions, and electron elastic scattering (ES) interactions [3]. Although the neutrino-matter cross-section is in general small, $O(10^{-42}\ \text{cm}^2 \times E_\nu\ /\text{GeV})$, for long propagation lengths and in dense enough matter interactions between neutrinos and the medium can lead to appreciable effects on the survival and oscillation probabilities. Neutrino flavor states interact via CC interactions with their like-flavor leptonic counterparts and via NC and ES interactions with all other leptons. Earth (and solar) matter contains electrons, but few muons or taus. Therefore, neutrino-matter interactions are mostly restricted to CC, NC, and ES interactions between electron neutrinos and electrons, NC interactions between electrons, protons, and neutrons and all active neutrino flavors, and ES interactions between electrons and all active neutrino flavors.

Since NC and ES interactions affect all neutrino flavors equally these yield no cumulative effect on the oscillation probability. However, the electron neutrino component undergoes additional scattering, relative to the muon neutrino and tau neutrino components, via CC interactions as a neutrino mass state propagates through matter. This additional scattering effectively acts as additional electron neutrino mass. This matter-induced added electron neutrino mass leads to an effective change in the mass-squared differences in matter, which, in turn, impacts the oscillation probability. In particular, it affects the $P_{e\beta}$ channels (and their time-conjugate counterparts). The asymmetries between the vacuum and matter oscillation probability that can result, usually due to the presence of electrons in a medium and, hence, mostly affecting electron neutrino channels, are collectively known as matter effects. The most useful aspect of matter effects is that they enhance the difference between the oscillation probabilities resulting from each mass hierarchy because they predominantly affect m_1, which is mostly composed of electron neutrino flavor, see Figure 1. Therefore, the interaction of matter mass hierarchy effects has a more powerful signature than vacuum mass hierarchy effects, making matter effects instrumental for investigating the neutrino mass hierarchy.

Lastly, it should be noted that because matter effects only impact the electron neutrino flavor component, and not the electron antineutrino component, matter effects can confound an attempt to assess the existence of *CP*-violation by comparing a set of $P_{e\beta}$ and $P_{\bar{e}\bar{\beta}}$ channels. The ability to distinguish the two effects, *CP* versus matter, stems from the capacity to resolve the energy-dependent nature of the signature: *CP* effects are energy independent while matter effects are energy dependent.

Subtle Physics

Next we examine additional subtle neutrino oscillation physics that is neutrino energy dependent and can impact the estimation of neutrino oscillation parameters when analyzing neutrino oscillation experiments.

MSW Matter Resonances

A well-known feature of neutrino-matter effects is the appearance of Mikheev-Smirnov-Wolfenstein (MSW) matter resonances [1]. The appearance of these resonances depends on the neutrino energy, the mass hierarchy, and the baseline. Given the right combination of those three elements there can be a significant enhancement of the oscillation probability as a result of coherent forward scattering of neutrinos in matter. This occurs only for electron neutrinos in earth's matter, via charged current interactions, and leads to a bump in the oscillation probability over a small spectral window. The energy dependence of this resonance depends on the specific density of matter. To a first approximation the earth can be treated as two layers, a lower density outer mantle surrounding a higher density inner core, with the core being roughly twice the density of the mantle. As a result, MSW resonances for electron neutrinos traversing the earth exist for both the mantle and core respectively. For the mantle these resonances occur for ~ 3 GeV neutrinos, for the core they occur for ~7 GeV neutrinos. Observationally, the hallmark of these resonances is an increase of the electron neutrino conversion probability near the critical neutrino energy for a given matter density. The signature of

MSW resonance effects have been observed in both solar neutrino data and terrestrial atmospheric data.

Parametric Matter Resonances

There also exists a secondary type of matter resonance known as parametric resonance (see [7], [8]). These resonances are the result of correlations between an oscillating parameter, in this case the density of matter, and fundamental neutrino parameters that are also distance-dependent, namely the matter mixing angles and masses. In essence, as the neutrino traverses variable density layers the minimum possible oscillation probability gets boosted by the modulation of the matter density, such that while the overall probability within the layer reaches the same maximum, the baseline starting probability is varied with density. Given a long enough traversal distance this leads to an accumulating enhancement of the electron neutrino flavor conversion probability. In the earth, because the core density is twice the mantle density, parametric resonance can develop into a detectable size effect for neutrino traversing both the earth's mantle and core.

A key difference between MSW and parametric matter resonances is that MSW resonances occur in single-density layers while parametric resonances require at last two different density layers to develop. As a result, where there are parametric resonances there are automatically MSW resonances, such as for atmospheric neutrinos traversing the entire earth's radius; while there may be MSW resonances without the existence of parametric resonances, such as for beam neutrinos traversing a portion of the earth's mantle. Furthermore, the maximum possible probability is greater for parametric resonance in multiple density layers than for MSW resonance in a single constant density layer. Therefore, in cases where parametric resonance can develop, this can lead to significant changes in the conversion probability.

Parameter Degeneracies

Finally we mention the subtle physics of parameter degeneracies. As already mentioned, one method for testing *CP*-violation in neutrino oscillations is to look for an asymmetry between the neutrino and antineutrino survival or oscillation probability in the same channel. Any statistically significant deviation from zero difference then represents the appearance of *CP*-violation. This was originally one of the preferred methods in discussions of modes for probing neutrino *CP*-violation as well as for assessing neutrino mixing parameters. This involved generating measurements of the neutrino and antineutrino probabilities in the same channel at the same baseline and energy and then comparing the results. However, it was noted early on [9] that a significant complication of this approach was the appearance of degeneracies between mixing solutions, i.e., there exist as many as eight degenerate sets of oscillation parameters for each set of $P_{\alpha\beta}$ and $P_{\bar{\alpha}\bar{\beta}}$ measurements.

There are three possible degeneracies: a *CP* degeneracy, a mass hierarchy degeneracy, and a θ_{23} degeneracy. These degeneracies exist for a monoenergetic measurement, taken in the same neutrino and antineutrino channel at a single baseline. The *CP* degeneracy exists between pairs of $\{\delta_{CP}, \theta_{13}\}$ solutions; the mass hierarchy degeneracy exists between $\mathrm{sgn}(\Delta m^2_{31})$ solutions, approximating the normal hierarchy by $+\Delta m^2_{31}$ and the inverse hierarchy by $-\Delta m^2_{31}$, for each pair of $\{\delta_{CP}, \theta_{13}\}$ solutions; and the octant of θ_{23} degeneracy, for θ_{23} less than or greater than $\pi/4$ where $\pi/4$ gives maximal 2-3 mixing, exists for $\{\theta_{23}, \pi\text{-}\theta_{23}\}$, $\{\delta_{CP}, \theta_{13}\}$ pairs, and $\{+\Delta m^2_{31}, -\Delta m^2_{31}\}$ pairs. Therefore, in total, up to an eightfold degeneracy can exist for a pair of $\{\delta_{CP}, \theta_{13}\}$ solutions that is also doubly degenerate in the neutrino mass hierarchy and doubly degenerate in the octant of θ_{23}. The ironic feature of these degeneracies is that they can obscure precisely what a pair of monoenergetic $\{P_{\alpha\beta}, P_{\bar{\alpha}\bar{\beta}}\}$ measurements are designed to measure, *CP* violation. This is because all three degeneracies mix *CP*-conserving and *CP*-violating solutions: for particular values of $P_{\alpha\beta}\,(E, L)$ it is possible to have a set of degenerate solutions, one of which is *CP*-conserving and one of which is *CP*-violating. This mixing of *CP*-conserving and *CP*-violating solutions is the hallmark of what is traditionally meant by mixing parameter degeneracies.

Determining Mixing Parameters

We now turn to examining the body of work that has contributed to our current knowledge of neutrino oscillation parameters. Of the five fundamental mixing parameters, all five have been estimated and four are known to good precision. By devising experiments at a given L/E and using various neutrino sources and detection methods neutrino oscillation parameters can be extracted by comparing measurements of observed neutrino oscillation events of a particular flavor to the expected value given no oscillations. Any deviations from the expected value both confirm the neutrino oscillation picture and provide a way to determine, by statistical analysis, the phenomenological parameters that best fit the oscillation model to the observed neutrino event rate. This experimental and analytical method has been applied to four types of data: nuclear reactor data, accelerator beam data, solar neutrino data, and atmospheric neutrino data. We will discuss the nature and contribution of each data set in turn to the current phenomenological oscillation picture. For brevity, we restrict our discussion to those data sets which contributed to the completion of this work, rather than a comprehensive review of all data sets.

Basics of Oscillation Experiments

The present knowledge of oscillation parameters comes from neutrino oscillation experiments. Regardless of the particular neutrino source or detection method, oscillations are detected by comparing the observed number of neutrinos of one flavor-type to the number of neutrinos expected if oscillation between flavors occurs from source to detector, i.e., by comparing the observed number to the predicted number of signal events. If neutrinos of a flavor-type different from the flavor of the source neutrino flux are observed the results are identified as neutrino appearance and measure an oscillation probability. Whereas, if fewer neutrinos of the same flavor are seen than expected the results are known as neutrino disappearance and measure a survival probability. In general, the predicted number of signal events, $s(\theta_{jk}, \Delta m^2_{jk})$, depends on the oscillation probability:

$$s(\theta_{jk}, \Delta m^2_{jk}) = \int_{E\ min}^{E\ max} \epsilon(E)\phi_{\nu_\alpha}(E)P_{\alpha\beta}(E, \theta_{jk}, \Delta m^2_{jk})\, dE \tag{10}$$

where $E_{min/max}$ are the lower and upper neutrino energy bounds, $\epsilon(E)$ is the detection efficiency as a function of neutrino energy, $\phi_{\nu_\alpha}(E)$ is the source neutrino flavor flux as a function of energy, and $P_{\alpha\beta}$ is the oscillation probability as a function of the neutrino energy and mixing parameters. Eq. (10) illustrates that the sensitivity of an experiment to neutrino oscillation parameters will be determined by its baseline, average neutrino energy (via $P_{\alpha\beta}$), and detection efficiency. Furthermore, systematic errors of any type will decrease an experiment's sensitivity to oscillation physics, especially to subtle effects such as mass hierarchy, *CP*-violation, or matter effects.

Next we review the key experiments that currently define the world values of the neutrino mixing parameters, summarized in Table 1, and whose analyses were numerically reproduced as preparation for the present work.

Reactor and Accelerator Measurements: θ_{13}

Measurements of electron antineutrino survival probabilities can be used to determine the value of θ_{13}. Conventional reactors generate electron antineutrinos via the decay of uranium and plutonium fuel rod parent nuclei as fission takes place. Liquid scintillator detectors then detect this antineutrino flux via the inverse beta decay reaction $\overline{\nu}_e + p \rightarrow e^+ + n$. This is a good probe of electron antineutrino fluxes in the energy range 3 to 12 MeV. Reactor-detector baselines on the order of 1 km are well-suited to measure θ_{13}. To reduce systematic errors due to theoretical predictions of the reactor flux a two detector method is preferred. By comparing fluxes at functionally identical near and far detectors, errors can be greatly reduced, improving the measurement of the mixing parameter of interest. The design of reactor experiments is such that matter effects plays a negligible role: the baselines are too short for matter effects to develop and the detectors are rarely built very deeply underground such that the neutrino flux traverses very little matter.

The set of reactor experiments Daya Bay [10], RENO [11], and Double Chooz [12] were all designed specifically to measure θ_{13}. Daya Bay has three near and three far detectors measuring the flux from a complex of six reactors cores. The detectors are immersed in an ultrapure water vessel lined with photomultiplier tubes that is used to reduce backgrounds. Gadolinium doped and undoped liquid scintillator regions make up the fiducial detector volume, collecting light from inverse beta decay reactions via photomultiplier tubes lining the acrylic housing vessel. Daya Bay's extensive complex of reactors and detectors gives it the highest statistics and greatest precision of all the reactor experiments and it therefore sets the current world value for θ_{13}.

RENO also measures the flux from six reactors, with one near and one far detector. This reduces error by allowing the flux to be normalized, but also reduces its statistics relative to Daya Bay due to the presence of fewer detectors. Like Daya Bay, the detection technology is gadolinium doped and undoped liquid scintillator. Unlike Daya Bay, RENO's detectors are immersed in mineral oil and its outer region is lined with photomultipliers tubes, which serve as a veto shield for background events. Finally, the Double Chooz experiment has also estimated θ_{13}. Double Chooz is currently measuring the antineutrino flux from two reactors using a single near detector (a second far detector is under construction). Double Chooz's smaller reactor complex reduces its overall statistics, making it the least stringent constraint on a measurement of θ_{13}. Furthermore, because it is currently using only one near detector the antineutrino flux cannot be normalized, which introduces additional percent level errors not seen in the Daya Bay and RENO experiments. Despite the larger error bars and reduced statistics for the RENO and Double Chooz experiments relative to Daya Bay, all three reactor determinations of θ_{13} are in good agreement. Furthermore, all three experiments continue to run and reduce their errors while improving their statistics.

Reactor experiments are restricted by having low energy MeV neutrinos and restricted baselines, as the reactor flux drops off like $1/r^2$. To obtain higher GeV neutrino energies and longer baselines, accelerator neutrino beam experiments were built. Measurements of neutrino survival and oscillation probabilities using a near and far detector set-up and a neutrino beam constitute the accelerator data set and can be used to help constrain or measure all known mixing parameters, including θ_{13}. Conventional beam experiments create a secondary neutrino beam as a result of the decay of kaons and pions created by shining a primary proton beam on a graphite target. The resulting stream of charged pions are steered in the desired beam direction by magnetic focusing horns. This effectively steers the neutrino beam along a path between the near and far detector. The detectors, surrounded by a veto shield, are functionally equivalent and measurements taken in both can be used to normalize the flux and reduce errors.

The conventional neutrino beam is not monochromatic but a combination of mostly muon neutrino flavor with some electron neutrino flavor as well as muon and electron antineutrinos. This permits beam measurements to contribute to the determination of a wide variety of parameters as well as allowing comparisons between neutrino and antineutrino oscillation probabilities. The primary challenge of beam experiments is that while they have well constrained systematic errors the flux is quite low, averaging 1-10 neutrinos per year in a far detector. This significantly reduces their statistics and requires a much longer running time than reactor experiments before being able to publish significant findings, ~3-5 years on average for beam set-ups as compared to ~1 year for reactor set-ups. The main advantage to beam experiments over reactor experiments is that they have long baselines and their beam and detectors are buried far below ground leading to the appearance of matter effects. Both the just completed MINOS experiment and the still running T2K experiment have contributed to the current knowledge of θ_{13}.

MINOS is a long baseline, L = 735 km, accelerator experiment designed to measure muon neutrino disappearance at the peak neutrino energy of 3 GeV with a 0 to 100 GeV range [13]. It produces a clean on-axis beam of 98.7% $\nu_\mu + \bar{\nu}_\mu$ and 1.3% $\nu_e + \bar{\nu}_e$ that is incident on a 0.98 kton iron calorimeter near detector. The neutrino beam then travels an additional 735 km, where it is incident on the far detector located 700 m below ground. Like the near detector, the far detector is an iron calorimeter. However, the far detector has a fiducial mass of 5.4 ktons and a two-layer thick scintillator veto shield located over the top and sides. Despite structural differences, the near and far detectors are functionally identical, which reduces systematic error and allows the neutrino flux to be normalized.

MINOS is able to distinguish neutrino flavors by distinguishing among CC, NC, and ES interactions between beam neutrinos and the target detector material. Each flavor interaction has a unique topological signature: long multi-detector plane tracks for muon (anti)neutrino interactions; short diffuse showers for electron (anti)neutrino interactions. The event topology combined with energy information from calorimetry allow neutrino events to be identified and sorted and provides the means to veto non-beam and inherent-beam backgrounds to various MINOS data sets. MINOS measured the first confirmed signal in the muon to electron neutrino oscillation channel which allowed it to constrain

θ_{13} [13]. It also published a joint analysis with electron antineutrino appearance from its brief run in antineutrino mode [14]. It should be noted that its beam antineutrino mode is severely constrained by inherent beam background: in antineutrino mode MINOS produces an “antineutrino beam” of 58.1% ν_μ, 39.9% $\bar{\nu}_\mu$, and 2.0% $\nu_e + \bar{\nu}_e$.

The long baseline accelerator electron neutrino appearance data from T2K also puts bounds on θ_{13} [15]. This experiment has a two detector, 2.5° off-axis beam design. The off-axis set-up reduces inherent beam backgrounds and reduces the energy spread of the beam, improving T2K’s sensitivity to θ_{13}. T2K has a baseline of L = 295 km with a peak energy of 0.6 GeV and a 0.1-2.5 GeV spectrum. The near detector complex primarily uses calorimetry to characterize the beam, while the far detector uses existing technology from the Super-Kamiokande (Super-K) atmospheric neutrino oscillation experiment to measure the final flux.

Super-Kamiokande is a 50 kt water Cherenkov detector located 1000 m underground. It contains ultrapure water surrounded by photomultiplier tubes. ES interactions between the charged lepton partners of passing neutrinos of all flavors and electrons in the water produce Cherenkov rings, rings of delayed light created by the de-excitation of electrons displaced by the passage of charged particles through the water. Neutrino flavors can again be identified by the event topology: the passage of muon (anti)neutrinos produces sharp rings while the passage of electron (anti)neutrinos through the detector produces diffuse rings.

Atmospheric and Accelerator Constraints: θ_{23} and the Large Mass Splitting

Measurements of the flux of atmospheric neutrinos incident on the earth's surface and/or traversing the earth's mantle/core can be used to constrain the value of θ_{23} as well as the large, or atmospheric, mass splitting. Atmospheric neutrinos are created by the interaction of cosmic rays with particles in the earth's atmosphere. These interactions produce a shower of pions and kaons that, as in accelerator experiments, decay to produce neutrinos of all flavors with a broad array of energies.

The already mentioned Super-K experiment was originally built to confirm the existence of neutrino oscillations [16] and is the longest running neutrino oscillation experiment: it continues to run after having taken data for more than two decades. Because Super-K uses ES interactions, which do not have a low energy threshold, it is sensitive to a wide neutrino energy range. Furthermore, atmospherically produced neutrinos are free to enter the Super-K detector from all incident angles, overhead, along glancing paths through the earth's mantle, across deep core-crossing trajectories through the earth's radius, and so on. This gives Super-K sensitivity to the widest L/E range of all neutrino oscillation experiments, including to the L/E that maximizes the signal from θ_{23} and the large mass splitting driven muon neutrino oscillations.

Furthermore, as indicated in the earlier discussion on θ_{13}, both MINOS and T2K can measure muon neutrinos and, hence, muon neutrino survival probabilities, which can be used to estimate θ_{23} and the atmospheric mass splitting. Unlike in the case of θ_{13}, for the atmospheric mass splitting MINOS is currently the stronger experiment, having a larger set of data after 5 years of running. However, T2K has recently produced disappearance data that is beginning to surpass MINOS' precision and T2K is well poised to supersede both the long-standing Super-K and the recently contributed MINOS' constraints on the 2-3 mixing parameters.

Solar and Accelerator Data: θ_{12} and the Small Mass Splitting

Solar neutrinos are produced as a by-product of fusion reactions in the interior of the sun and come in all active flavors. These neutrinos oscillate extensively along the journey between the earth and the sun. Radiochemcial detectors are sensitive to the full spectrum of neutrino flavors through CC, NC, and ES reactions between these low-energy, ~ 1 – 15 MeV, solar neutrinos and target nuclei in large liquid chemical detectors containing argon, chlorine, heavy water or other target atoms. Early radiochemical measurements of the flux of solar neutrinos, including those done by Homestake [17], GALLEX [18], GNO [19], and SNO [20], combined with short baseline, L ~ 1 km, accelerator data from the KamLAND [21] experiment were able to help definitively estimate the value of the mixing angle θ_{12} as well the Δm^2_{21} small, or solar, mass splitting. The good precision on the 1-2 mixing parameters stems from the combination of experiment types, which reduces the influence of systematic errors on the final results, and the high solar flux and lengthy run time of the solar neutrino experiments, ~ 10+ years, despite the inherent uncertainties in estimating the precise flux of solar neutrinos.

Global Analyses: Estimates of All Oscillation Properties

Global analyses, which combine data sets from multiple sectors to simultaneously extract various mixing parameters as well as attempt to assess other neutrino oscillation properties such as the mass ordering and *CP*-phase, have also contributed to our current understanding of the standard three neutrino paradigm. We review here three well-cited published global analyses by leading collaborations in the field of neutrino oscillation phenomenology. While global analyses are not generally capable of determining mixing parameter values, they are instrumental in helping determine the source of dominant mixing parameter constraints as well as for seeking signatures of subtle physics in neutrino oscillation data, which can often be obscured by systematic errors in individual data sets, but may be hinted at by a combination of data sets.

Forero et al. Global Analysis 2012

Forero *et al.* [22] analyzed the following set of experiments: Daya Bay, Double Chooz, RENO, Homestake, GALLEX/GNO, SAGE [23], Borexino [24], Super-Kamiokande 1-3, SNO 1-3, KamLAND, MINOS (appearance, disappearance, neutrino, and antineutrino), and T2K (appearance and disappearance). Furthermore, they modeled the reactor and solar data using various published reactor flux models and published solar flux models. Moreover, rather than model Super-K (atmospheric data) they included the published Super-K analysis in their results.

Forero *et al.* found that reactor data establishes nonzero θ_{13} and that Daya Bay dominates the determination of θ_{13}. $\theta_{13} = 0$ is excluded by their analysis at 10.2σ. Their analysis also indicated that MINOS and T2K show a preference for non-maximal θ_{23}, i.e., $\theta_{23} < \pi/4$. Lastly for individual experiments, they found Δm^2_{31} is set by MINOS disappearance data. Other parameters are well determined by the combination of solar and KamLAND data. When examining combinations of data sets their analysis showed little preference for either hierarchy or to the *CP*-phase. Sensitivity to δ_{CP} in their analysis was only due to long baseline data, and none from atmospheric data, as might be expected, because of the approximations used in modeling the atmospheric data.

Forero *et al.* found maximal θ_{23} to be slightly rejected, a trend that was weaker for the normal hierarchy than the inverse hierarchy. Non-maximal θ_{23} appeared to be driven by MINOS. Identifying the octant stemmed from the interplay of long baseline, atmospheric, and reactor data. MINOS alone is insensitive to the octant because matter effects are too small to break the octant symmetry. However, adding reactor antineutrino data breaks the octant degeneracy and gives a preference for $\theta_{23} < \pi/4$. Additionally, adding in atmospheric data also gives a preference for second octant, non-maximal mixing.

Fogli et al. Global Analysis 2012

Fogli *et al.* [25] included in their global analysis the experiments T2K (appearance and disappearance), MINOS (appearance, disappearance, neutrino and antineutrino), SNO, Borexino, KamLAND, and Super-K 1-4 without the neutrino/anti neutrino separation data. They also included Chooz, Double Chooz, Daya Bay, and RENO grouped as short baseline data using older fluxes [26] for single detector models.

They did not reproduce Daya Bay and RENO, but included the results of both experiments as Gaussian constraints on $\sin^2 \theta_{13}$.

Regarding θ_{23}, Fogli *et al.* found that the long baseline muon neutrino disappearance and appearance, $P_{\mu e}$ and $P_{\mu\mu}$ respectively, dominant Δm^2 terms are octant symmetric. However, these two data sets also have Δm^2 matter terms that can help lift the octant degeneracy and are sensitive to the mass hierarchy and δ_{CP}. Long baseline electron neutrino appearance data gives an anti-correlation between the mixing angles θ_{13}-θ_{23} while reactor electron antineutrino survival data is sensitive to θ_{13} at the large mass splitting scale and subdominant P_{ee} Δm^2 terms are sensitive to the mass hierarchy and θ_{12}. Because of the anti-correlation that they found between θ_{13}-θ_{23}, reactor-driven knowledge of θ_{13} can help lift the octant degeneracy coming from degenerate (θ_{23}, θ_{13}) solutions in different octants. Super-K alone is not good at solid hints for physics such as the mass hierarchy or *CP*-phase because subdominant three neutrino physics is spread out over a wide spectra and can be accounted for by systematics. There is a hint from atmospheric data for $\delta_{\mathrm{CP}} \sim \pi$ due to a “slight electron excess…at sub-GeV energies” (p. 3).

Fogli *et al.*, found that long baseline disappearance data disfavors maximal θ_{23} mixing. A combination of solar and KamLAND prefers a value of θ_{13} which picks out the first (second) octant for normal (inverse) hierarchy. However, there is negligible statistical difference between θ_{23} solutions for the expanded combination of long baseline, solar, and KamLAND data. Adding in short baseline data selects large θ_{13}, leading to a first octant θ_{23} preference. Adding in atmospheric data does not affect θ_{13}, but contributes to a preference for first octant θ_{23}. Similarly, the combination of long baseline, solar, KamLAND, and short baseline experiments leads to preferred δ_{CP} ranges. Adding in atmospheric then gives a preference for $\delta_{\mathrm{CP}} = \pi$, though the δ_{CP} preference is not statistically significant. They found no strong mass hierarchy preference. Long and short baseline data together prefer the inverse hierarchy while long baseline, short baseline, and atmospheric data combined prefer the normal hierarchy.

Gonzalez-Garcia et al. Global Analysis 2012

Gonzalez-Garcia *et al*. [27] used an extensive data set: Super-K 1-4, K2K [28], MINOS (appearance, disappearance, neutrino, and antineutrino), T2K (appearance and disappeareance), Chooz [29], Palo Verde [30], Double Chooz, Daya Bay, RENO, KamLAND, Homestake Chlorine, GALLEX/GNO, SAGE, Super-K electron scattering data, SNO 1-3, Borexino, and lastly a set of older reactor experiments referred to as short baseline data including Bugey 4 [31], Bugey 3 [32], ROVNO4 [33], Krasnoyarsk [34], ILL [35], Goesgen [36], SRP [37], and ROVNO88 [38]. For single detector reactor experiments they modeled the data using both older [39] and newer [40] reactor fluxes.

In agreement with previous experimental and global findings, Gonzalez-Garcia *et al.* found $\theta_{13} = 0$ is disfavored by Daya Bay, Double Chooz, and RENO and that the main uncertainty in θ_{13} remains due to uncertainty on reactor fluxes in single detector ($L < 100$ m baseline) experiments. Non-maximal θ_{23} mixing was disfavored for both mass hierarchies and independent of reactor flux used. The preference for hierarchy changes with reactor flux used, but either way stays negligible at roughly $\sim 0.7\sigma$ level. *CP*-phase preferences were found at less than $\sim 2\sigma$ level for either mass hierarchy. Also, their analysis showed that $L \sim 1$ km experiments, i.e., reactor experiments, are sensitive to

Δm^2_{31}, but with high error until the data include spectral, not just rate-only, information. Though, in principle, long baseline combined with reactor data should be able to resolve the θ_{23} octant degeneracy, they found this does not yet play out. Resolving the octant requires atmospheric data to be included. The combination of long baseline and reactor data are somewhat sensitive to the *CP*-phase, more so if the mass hierarchy and octant are well constrained by other data. Again, in their analysis this sensitivity grew when atmospheric data was included.

Gonzalez-Garcia *et al*. attribute the global first octant preference to a "zenith-angle independent event excess in sub-GeV *e*-like data in" (p. 14) atmospheric data. Atmospheric data's choice of θ_{13} limits the long baseline and reactor allowed parameter space, which gives a preference for δ_{CP}. Hence, they attribute θ_{23} and δ_{CP} hints to subdominant effects in atmospheric data. They also conclude that non-maximal θ_{23} is driven by MINOS muon neutrino disappearance, in agreement with Fogli *et al*. and Forero *et al*., but does not play out in a global analysis, only atmospheric data reinforces this preference. Overall, they conclude that long baseline and reactor data combined should be able to disentangle the octant and contribute to identifying the *CP*-phase, when these two data sets improve their statistics. They attribute any global preference to θ_{23} or δ_{CP} as being due to the interplay of atmospheric data with parameter constraints from other data sets. Lastly, they cite the preference for δ_{CP} as being driven by a complex interplay: MINOS muon neutrino disappearance drives θ_{13}; atmospheric data disfavors θ_{23} maximal; and long baseline electron neutrino appearance and reactors set θ_{13}; the combination of which restrict the allowed δ_{CP} parameter space.

Assessing Next Steps

Finally, we summarize the status of the current three-neutrino paradigm, including the values of the known mixing parameters, as well as review the open questions and challenges to completing the standard oscillation picture.

Summary of Oscillation Properties

In Table 1 we summarize measurements of mixing parameters from experimental data and indications of mixing parameters and oscillation properties from global analyses. In brief, all of the independent mixing parameters have been estimated, but there is, as yet, no convergent estimate of the neutrino mass hierarchy or *CP*-phase.

Table 1. Summary table of extracted mixing properties by collaboration. Parameters are cited as reported in the source publication. NH: normal hierarchy; IH: inverse hierarchy. If no δ_{CP} value is listed then analysis was for $\delta_{CP}=0$.

Collaboration	Angle / Phase [rads]	Mass Splitting [eV^2]	Errors
MINOS [41] $P\,(\nu_\mu \rightarrow \nu_e)$	NH: $2\sin^2\theta_{23}\sin^2 2\theta_{13} = 0.041^{+0.047}_{-0.031}$ IH : $2\sin^2\theta_{23}\sin^2 2\theta_{13} = 0.079^{+0.071}_{-0.053}$	---	68% C. L.
MINOS [42] $P\,(\nu_\mu \rightarrow \nu_\mu)$	$\sin^2 2\theta > 0.90$	$\lvert\Delta m^2\rvert = 2.32^{+0.12}_{-0.08}\times 10^{-3}$	90% C.L.
MINOS [43] $P\,(\nu_\mu \rightarrow \nu_\mu)$ + $P\,(\bar{\nu}_\mu \rightarrow \bar{\nu}_\mu)$	$\bar{\nu}$: $\sin^2 2\bar{\theta} = 0.97^{+0.03}_{-0.08}$ ν : $\sin^2 2\theta = 0.950^{+0.035}_{-0.036}$	$\bar{\nu}$: $\lvert\Delta \bar{m}^2\rvert = 2.50^{+0.23}_{-0.25}\times 10^{-3}$ ν : $\lvert\Delta m^2\rvert = 2.41^{+0.09}_{-0.10}\times 10^{-3}$	86% C.L.

Collaboration	Angle / Phase [rads]	Mass Splitting [eV^2]	Errors
MINOS [14] $P(\nu_\mu \rightarrow \nu_e)$ + $P(\bar{\nu}_\mu \rightarrow \bar{\nu}_e)$	NH, 1st octant: $2\sin^2\theta_{23}\sin^2 2\theta_{13} = 0.051^{+0.038}_{-0.030}$ IH, 1st octant: $2\sin^2\theta_{23}\sin^2 2\theta_{13} = 0.093^{+0.054}_{-0.049}$	---	68% C. L.
T2K [15] $P(\nu_\mu \rightarrow \nu_e)$	NH: $\sin^2 2\theta_{13} = 0.140^{+0.038}_{-0.032}$ IH : $\sin^2 2\theta_{13} = 0.170^{+0.045}_{-0.037}$	---	68% C.L.
T2K [44] $P(\nu_\mu \rightarrow \nu_\mu)$	NH: $\sin^2\theta_{23} = 0.514^{+0.055}_{-0.056}$ IH : $\sin^2\theta_{23} = 0.511^{+0.055}_{-0.055}$	NH: $\Delta m^2_{32} = 2.51^{+0.10}_{-0.10} \times 10^{-3}$ IH : $\Delta m^2_{31} = 2.48^{+0.10}_{-0.10} \times 10^{-3}$	68% C.L.
Daya Bay [10]	$\sin^2 2\theta_{13} = 0.090^{+0.008}_{-0.009}$	NH: $\Delta m^2_{32} = 2.54^{+0.19}_{-0.20} \times 10^{-3}$ IH : $\Delta m^2_{32} = 2.64^{+0.19}_{-0.20} \times 10^{-3}$	68.3% C.L.
RENO [11]	$\sin^2 2\theta_{13} = 0.113^{+0.019}_{-0.019}$	---	1σ
Double Chooz [45]	$\sin^2 2\theta_{13} = 0.086^{+0.030}_{-0.030}$	---	68% C. L.
Super-K [46]	NH: $\sin^2\theta_{23} = 0.425^{+0.391}_{-0.619}$ IH : $\sin^2\theta_{23} = 0.575^{+0.393}_{-0.630}$	NH: $\Delta m^2_{32} = 2.66^{+0.15}_{-0.40} \times 10^{-3}$ IH : $\Delta m^2_{32} = 2.66^{+0.17}_{-0.23} \times 10^{-3}$	90% C.L.
KamLAND + Solar [21]	$\tan^2\theta = 0.40^{+0.10}_{-0.07}$	$\Delta m^2 = 7.9^{+0.6}_{-0.5} \times 10^{-5}$	1σ

Collaboration	Angle / Phase [rads]	Mass Splitting [eV^2]	Errors
Gonzalez-Garcia *et al.* [1] [27]	Marginalized over mass orderings $\sin^2\theta_{12} = 0.302^{+0.013}_{-0.012}$ $\sin^2\theta_{13} = 0.0227^{+0.0023}_{-0.0024}$ $\delta_{CP} = 300°\,^{+66°}_{-138°}$ 1st octant min: $\sin^2\theta_{23} = 0.413^{+0.037}_{-0.025}$ 2nd octant min: $\sin^2\theta_{23} = 0.594^{+0.021}_{-0.022}$	$\Delta m^2_{21} = 7.50^{+0.18}_{-0.19}\times 10^{-5}$ NH: $\Delta m^2_{31} = +2.473^{+0.070}_{-0.067}\times 10^{-3}$ IH : $\Delta m^2_{32} = -2.427^{+0.042}_{-0.065}\times 10^{-3}$	1σ
Fogli *et al.* [25]	$\sin^2\theta_{12} = 0.307^{0.325}_{0.291}$ NH : $\sin^2\theta_{23} = 0.386^{0.410}_{0.365}$ $\sin^2\theta_{13} = 0.0241^{0.0266}_{0.0216}$ $\delta_{CP} = 1.08\pi^{1.36\pi}_{0.77\pi}$ IH : $\sin^2\theta_{23} = 0.392^{0.431}_{0.370}$ $\sin^2\theta_{13} = 0.0244^{0.0267}_{0.0219}$ $\delta_{CP} = 1.09\pi^{1.47\pi}_{0.83\pi}$	$\delta m^2 = 7.54^{7.80}_{7.32}\times 10^{-5}$ NH: $\Delta m^2 = 2.43^{2.49}_{2.33}\times 10^{-3}$ IH : $\Delta m^2 = 2.42^{2.49}_{2.31}\times 10^{-3}$ $\Delta m^2 = m_3^2 - \frac{\left(m_1^2 + m_2^2\right)}{2}$	1σ range
Forero *et al.* [22]	$\sin^2\theta_{12} = 0.320^{0.336}_{0.303}$ NH : $\sin^2\theta_{13} = 0.0246^{0.0275}_{0.0218}$ $\delta_{CP} = 0.80\pi^{2\pi}_{0}$ NH local min: $\sin^2\theta_{23} = 0.427^{0.461}_{0.400}$ NH global min: $\sin^2\theta_{23} = 0.613^{0.635}_{0.573}$ IH : $\sin^2\theta_{13} = 0.0250^{0.0276}_{0.0223}$ $\delta_{CP} = -0.03\pi^{2\pi}_{0}$ $\sin^2\theta_{23} = 0.600^{0.626}_{0.569}$	$\Delta m^2_{21} = 7.62^{7.81}_{7.43}\times 10^{-5}$ NH: $\Delta m^2_{31} = 2.55^{2.61}_{2.46}\times 10^{-3}$ IH : $\Delta m^2_{31} = 2.43^{2.50}_{2.37}\times 10^{-3}$	1σ range

---

[1] Quoted “Free Fluxes” values that include reactor short baseline data, rather than “Huber Fluxes” values which neglect reactor short baseline data.

Open Questions and Challenges in the Field

A review of recent talks (see [47], [48], [49], [50]) on challenges facing the completion of the neutrino picture lead to a number of issues. Many authors make interesting points regarding the paradigmatic approach to analyzing neutrino oscillation data. H. Minakata [47] stresses the need to pursue "double coverage," i.e., verifying elements of the three-neutrino mixing framework via convergent answers from different sources. Aspects of the model that have already been successfully double covered include: Δm^2 (large/atmospheric mass-squared difference) and θ_{23} from atmospheric and accelerator data; δm^2 (small/solar mass-squared difference) and θ_{12} from solar and KamLAND data; and θ_{13} from reactor and accelerator data. Fogli *et al.* [25] point out that, particularly, "accelerator experiments are urged to abandon any 2ν approximation in the interpretation of their…data, and focus on full-fledged 3ν combinations" (p. 3) in order to retain sensitivity to subtle physics, or "sub-leading effects," in the data. Furthermore they stress that "the success story of the indications of $\theta_{13} > 0$…shows that discussions of $\sim 2\sigma$ effects may…have some interest" (p. 3). In other words, more rigorous treatments and greater attention to detail, are in order. In addition to these overarching points, most agree that three open questions remain, discussed below in order of expected resolution.

Mass Hierarchy

The first question to be answered is, what is the correct neutrino mass ordering? The recently measured, large value of θ_{13} improves the possibility of determining the mass hierarchy via matter effects in a single experiment. The current challenge facing a hierarchy determination is that no relevant experimental data exists. As a result, most knowledge of the mass hierarchy comes in the form of indications obtained by conducting side-by-side analyses fitted to global data, one analysis for each possible hierarchy. However, the presence of low statistics and large experimental errors, especially on energy resolutions, has traditionally washed out even a medium-sized signal of a preference for either hierarchy. On the positive front, the NOνA [51] experiment, which just began taking data, will have sensitivity to the mass hierarchy because of its extended baseline, which increases the influence of matter effects. Furthermore, future Super-K data may yield insight into the hierarchy if statistics increase in the lower energy bins and energy resolutions improve.

In a recent talk, H. Minakata [47] gave a comprehensive overview of paths toward determining the mass hierarchy. With high enough statistics NOνA or T2K could determine the mass hierarchy for specific values of the *CP*-phase. However, as K. Nishikawa [48] points out, 50% of δ_{CP} values will cancel out mass hierarchy effects in NOνA likely making it impossible to determine the hierarchy with this experiment alone. H. Minakata goes on to say that the combination of neutrino + antineutrino accelerator and atmospheric data could determine the correct hierarchy for any δ_{CP} with small enough systematics. An alternative route would be to assess the sign difference between the vacuum Δm^2 from electron and muon neutrino disappearance. For the normal hierarchy the sign difference is positive, for the inverse hierarchy it is negative. However, this would require sub-percent level accuracy.

It is also possible to look for phase differences in the oscillations between the solar- and atmospheric-driven mass scales and determine the hierarchy, given an energy resolution of a few percent. For the normal hierarchy the phase of atmospheric oscillations is advanced, for the inverse the phase is retarded, relative to the solar mass scale oscillations. Furthermore, core-crossing atmospheric data alone could measure the mass hierarchy, without accelerator data, given very high statistics. This depends somewhat on θ_{23}, since the primary atmospheric experiment, Super-K, uses a water Cerenkov detector whose sensitivity to the hierarchy is governed by θ_{23}, i.e., it is better for larger θ_{23}. Overall, continued difficulties in gaining high enough statistics and reducing systematic errors do not yield a positive outlook for assessing the mass hierarchy in the immediate future. As H. Minakata urges, the current state of affairs, "stimulates [us]…to invent new ideas and necessitates [a] quantitative reexamination of practical ways to explore [the mass hierarchy]" (p. 173).

Octant of θ_{23}

The second question to be answered is, what is the octant of θ_{23}? Individual experiments are subject to the octant degeneracy and hence cannot assess θ_{23}. Additionally, there appears to be no near-term resolution of the octant by relying on global analyses either. As Forero *et al.* [22] pointed out, there is consistently disagreement among global analyses about θ_{23} and the source of that "discrepancy" is unknown. The results of their analysis imply, however, that the interplay of accelerator + reactor + atmospheric data can lead to a preference for θ_{23}, albeit one highly sensitive to the details of the analysis. This understanding is supported by the results of both Fogli *et* *al*. [25] and Gonzalez-Garcia *et al*. [27]. Taken together, this suggests that the current source of the discrepancy may stem from a lack of consensus about how to treat one or more data sets used in global analyses. Barger *et al.* [9] points out that, in principle, the only measurements that can definitively determine the octant of θ_{23} are a comparison of $P(\nu_\mu \to \nu_e)$ and $P(\nu_e \to \nu_\tau)$, which have leading terms in $\sin\theta_{23}$ and $\cos\theta_{23}$, respectively. Unfortunately, measurements of ν_τ require a neutrino factory, technology which is some years off.

CP-Phase

The third and final question to be answered in order to complete the three-neutrino picture is, what is the value of the neutrino Dirac *CP*-phase? The recently measured, large value of θ_{13} permits, but does not improve, the possibility of measuring δ_{CP}. So far, global and individual experimental analysis curves show there is no physics at play to constrain δ_{CP}, i.e., most of the *CP*-phase space is still allowed and very little of it is excluded. H. Minakata suggests that the combination of reactor + accelerator data may be able to determine the sign of δ_{CP} to 1σ in ~5 years. He also points out that to truly constrain δ_{CP} we will likely need to build a dedicated experiment to measure δ_{CP} in the future.

K. Nishikawa [48] supplements this picture with a subtle point: we need to distinguish a measurement of δ_{CP} from a measurement of *CP*-violation. In principle, it is possible that there are other sources of *CP*-violation in neutrino oscillations, not just that amount due to the *CP*-phase. So it is important to remember that in measuring the *CP*-phase, a zero measurement would not automatically rule-out *CP*-violation in the three-neutrino picture. A measurement of $\delta_{CP} = 0$ could mean that *CP*-violation occurs through some non-standard mechanism, which would require additional theoretical and experimental work to assess.

Lastly, Barger *et al*.'s [9] work on parameter degeneracies, which occur for sets of mixing parameters in a measurement of the same neutrino/antineutrino channel at a single kinematical phase $\Delta m^2 L/E$, is important to recall. A key challenge of these degeneracies is that *CP*-conserving and *CP*-violating solutions can be degenerate. "[In] principle there can be as much as an eightfold ambiguity in determining δ_{CP} and θ_{13} from $P\,(\nu_\mu \rightarrow \nu_e)$ and $P(\bar{\nu}_\mu \rightarrow \bar{\nu}_e)$ at a single L and E_ν …Measurements at multiple L and E_ν can be used to help discriminate" (p. 8). In other words, there is continued support for seeking out double coverage to ensure that degeneracies are resolved. And again, K. Nishikawa reminds us of a subtle detail. In any measurement of δ_{CP} based on earth matter effects there will exist the need to distinguish between a neutrino/antineutrino matter-induced asymmetry and a neutrino/antineutrino *CP*-violation-induced asymmetry. The confusion between the source of the asymmetry exists only in the $P_{\mu e}$ channel and stems from the fact that matter effects occur for electron neutrinos (with electrons in ordinary earth matter) but not for electron antineutrinos (since positrons do not exist to a significant fraction in ordinary earth matter). Unfortunately, the $P_{\mu e}$ channel is the only channel for which *CP*-phase terms survive in the oscillation probability. Fortunately, matter and *CP* effects have different energy dependencies providing a way to distinguish between them, so long as an experiment has excellent energy resolution.

Moving Forward

In summary, the big picture status of neutrino oscillation phenomenology is as follows: The immediate goal of the field is to determine the correct neutrino mass hierarchy, followed by determining the correct octant of θ_{23} and the value of the *CP*-phase. Current experimental challenges to extracting these properties, namely limited neutrino energy resolution, low statistics, and high backgrounds, continue to be reduced in current and future experimental designs. Within the next five years more precise data sensitive to subtle physics—the mass hierarchy, octant, and *CP*-phase—will become available. Although this data will be more precise, inherent limitations in experimental design will prevent these observations from definitively assessing the mass hierarchy, octant, or *CP*-phase. In addition, existing discrepancies between current analyses of the data published by various groups are likely to propagate into the future. There exists a need to improve the extraction of subtle physics from multiple types of experimental data, in order to maximize future observations. Furthermore, there is a need to reach a field-consensus about how the standard three-flavor oscillation model should be treated when analyzing and interpreting the data. Motivated by these existing challenges to the field, we followed-up on previous work we had done (see [52], [53]), which showed promise in providing a useful and timely contribution to addressing these two needs.

CHAPTER II

RE-FRAMING THE ANALYSIS PARADIGM

In this chapter we review work previously done by our collaboration to extract neutrino mixing parameters using a novel set of bounds on the mixing angle θ_{13}. In the first few sections we discuss the existence and features of the oscillation parameters and oscillation probability under the re-framing of the bounds on θ_{13}. This is followed by a review of our previous findings regarding θ_{13} and the mass hierarchy using this new paradigm. We also briefly review a few other relevant works such as our examination of correlations between the mixing angles θ_{13} and θ_{23} using the new paradigm, as these will be useful for later. Lastly, we summarize this chapter with a discussion of the implications of using this novel paradigm to re-analyze the world's data, which motivated the present work.

Alternative Paradigm: Bounds on the Mixing Angle θ_{13}

In this section we discuss the bounds used on the mass-squared differences and mixing angles in our analysis. These are not the popularly used bounds (see, for example, [22], [25], [27]); in fact, to our knowledge, they have been referenced only by our group and one other group [54]. However, as succeeding sections will demonstrate, these bounds elicit an important connection between the mixing angle θ_{13} and the neutrino mass hierarchy making them useful. Furthermore, they are a computationally convenient choice. We begin by discussing the mass hierarchy and bounds on the mass-squared differences, followed by our bounds on the mixing angles and *CP*-phase. We then go on to discuss physical features of the oscillation probability relevant to the extraction of mixing parameters that are the result of this particular choice of bounds.

Bounds on Mass-Squared Differences and Mass Ordering

The goal of the present section is to remind ourselves of the effects of changing the hierarchy on the mass-squared differences. What we wish to do is understand how to correctly define the Δm_{ij}^2 in the three-neutrino framework in order to understand how the hierarchy is correctly included and interchanged in a calculation of the oscillation probability. We begin with the normal hierarchy as illustrated in Figure 2.

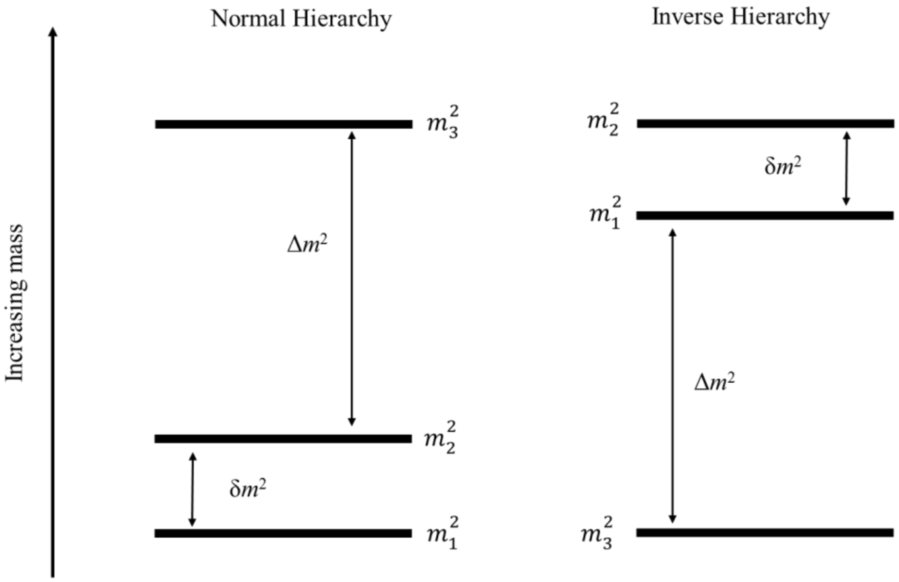

Figure 2. Mass ordering schemes for three neutrino flavors.

By convention, we define m_1^2 as the lighter of the two mass states of Δm_{21}^2. More precisely, we define it as the lighter of the two states m_1^2 and m_2^2. Even more precisely, we define m_1^2 as the lighter of the two mass states driving solar oscillations (historically, the first measured neutrino oscillations). The solar mass splitting, Δm_{21}^2 turned out to be the smaller of the two observed splittings. Hence, we can ever more precisely define m_1^2 as the lighter of the two mass states that determine the small mass splitting, where the other mass states are increasingly heavy. By convention, this puts the splitting Δm_{32}^2 on top of Δm_{21}^2 and m_1^2 is the lightest mass state while m_3^2 is the heaviest. Δm_{32}^2 is determined from and drives atmospheric oscillations. Since the index labels *ij* are all by convention, but the size of the mass splittings is fixed, we can alternatively refer to the small mass splitting δm^2 as that which drives the solar oscillations and the large mass splitting Δm^2 as that which drives atmospheric oscillations. This makes δm^2 and Δm^2, since they refer to the magnitude of the splittings, convention-independent and, hence, hierarchy-independent (or invariant under a change in the hierarchy).

Generally speaking, all parameters have a mathematical definition, an allowed range of values, and a sign, which in combination give the complete definition of a parameter. Therefore our next goal is to clearly define the Δm_{ij}^2 in each hierarchy, beginning with the normal hierarchy. Based on the convention given above and using the figure it is simple enough to write down the full definition for the mass eigenstate splittings in the normal hierarchy:

Normal hierarchy mass parameter definitions

$$\Delta m_{ij}^2 \equiv m_i^2 - m_j^2 \tag{11}$$

$$m_1^2 \ll m_2^2 \ll m_3^2 \tag{12}$$

Normal hierarchy mass parameter signs

$$\Delta m_{21}^2 > 0 \tag{13}$$

$$\Delta m_{32}^2 > 0 \tag{14}$$

$$\Delta m_{31}^2 > 0 \tag{15}$$

Normal hierarchy mass parameter bounds

$$\Delta m_{21}^2 = [0, +\infty) \tag{16}$$

$$\Delta m_{32}^2 = \left(\Delta m_{21}^2, +\infty\right) \tag{17}$$

$$\Delta m_{31}^2 \equiv \Delta m_{21}^2 + \Delta m_{32}^2 \tag{18}$$

Note that, as a result of the above conventional definition, we can define,

Small mass splitting

$$\delta m^2 \equiv \left|\Delta m_{21}^2\right| \tag{19}$$

Large mass splitting

$$\Delta m^2 \equiv \left|\Delta m_{32}^2\right| \tag{20}$$

thus,

$$\delta m^2 \ll \Delta m^2 \tag{21}$$

Now we can generate the same definition set for the inverse hierarchy. We start by noting that m_1^2 less than m_2^2 is set by convention, and by convention is defined to be hierarchy invariant. Also, to maintain an internally consistent physics framework requires that δm^2 be less than Δm^2 and for this relationship to also be hierarchy-invariant.

Since we cannot change δm^2 the only remaining option is to re-order the mass splittings. This forces m_3^2 to become the lightest mass state and m_2^2 the heaviest. Hence the full definition of the Δm_{ij}^2's in the inverse hierarchy is:

Inverse hierarchy mass parameter definitions

$$\Delta m_{ij}^2 \equiv m_i^2 - m_j^2 \tag{22}$$

$$m_3^2 \ll m_1^2 \ll m_2^2 \tag{23}$$

Inverse hierarchy mass parameter signs

$$\Delta m_{23}^2 > 0 \tag{24}$$

$$\Delta m_{21}^2 > 0 \tag{25}$$

$$\Delta m_{13}^2 > 0 \tag{26}$$

Inverse hierarchy mass parameter bounds

$$\Delta m_{21}^2 = (0, +\infty) \tag{27}$$

$$\Delta m_{13}^2 = \left(\Delta m_{21}^2, +\infty\right) \tag{28}$$

$$\Delta m_{23}^2 \equiv \Delta m_{21}^2 + \Delta m_{13}^2 \tag{29}$$

This indicates that the labelled splittings Δm_{ij}^2 do not have the same meaning in each hierarchy. In the normal hierarchy Δm_{32}^2 is the larger splitting and Δm_{31}^2 is the full splitting; in the inverse hierarchy Δm_{32}^2 is the full splitting and Δm_{31}^2 is the larger mass splitting. Also, Δm_{31}^2 and Δm_{32}^2 undergo a sign change in going from the normal hierarchy to the inverse hierarchy:

Normal → Inverse hierarchy mass parameter mapping

$$\Delta m_{31}^2 \rightarrow \Delta m_{23}^2 = -\Delta m_{32}^2 \tag{30}$$

$$\Delta m_{32}^2 \rightarrow \Delta m_{13}^2 = -\Delta m_{31}^2 \tag{31}$$

$$\Delta m_{21}^2 \rightarrow \Delta m_{21}^2 \tag{32}$$

This means that experimental measurements of the mass splittings measure the magnitude of $|\Delta m_{ij}^2|$, but the Δm_{ij}^2 to which the measurement is assigned depends on the hierarchy used in the fit. Therefore, a full interchange in hierarchies requires a simultaneous mapping of two parameters, the large and small mass-splittings, which changes both their value and sign. Since the larger mass splitting is two orders of magnitude larger than the small one it dominates the full splitting. For this reason it is common to approximate the hierarchy by freely interchanging Δm_{31}^2 and Δm_{32}^2 and using a positive sign for normal hierarchy and a negative sign for the inverse hierarchy.

So long as the terms in the oscillation probability do not strongly depend on linear effects or interference terms this approximation is harmless. However, it would not be valid for a case where linear, mixed Δm_{31}^2 and Δm_{32}^2 terms appear as you would induce an artificial sign change when there should be none.[2] This approximation is also unwise when the magnitude of effects between Δm_{31}^2 and Δm_{32}^2 are important. In summary, it is possible to think about the hierarchy conceptually as follows: the hierarchy keeps all the three-neutrino physics (magnitude of the mass splittings) the same it just (1) puts it in a different channel (*ij* relabeling) and (2) suppresses/enhances the associated linear effects (sign change on linear, pure mass scale terms).

---

[2] This problem is avoided by rewriting oscillation equations in terms of just two independent mass-squared differences and eliminating the third. In this case a hierarchy change is fully captured by changing the sign on the larger mass-squared difference.

Bounds on Mixing Angles and *CP*-Phase

The overall goal of this section is to determine the remaining allowed parameter space for the fundamental mixing parameters in the three neutrino framework: Δm_{ij}^2, θ_{ij}, and δ_{CP}. We have already identified the allowed bounds for the mass splittings in both hierarchies when we discussed the mass orderings. This leaves the allowed bounds on the mixing angles and leptonic Dirac phase. Identifying the allowed bounds and alternative conventions for defining the bounds is crucial to the analysis presented in this work: the bounds used here are not those implemented in similar analyses. We stress that this discussion is somewhat general and relies only on assuming a neutrino oscillation model where flavor states are linear combinations of mass eigenstates, i.e., it is does not depend on a particular parameterization. For simplicity we will present a general, logical argument for the bounds here using in particular the oscillation probability $P_{\mu e}$ for illustration. Previous work has demonstrated using either group theory [55] or tensor analysis [54] the validity of the bounds shown in this section are generally true for the parameterization presented here, for any oscillation probability, and in either vacuum or matter.

We begin our illustration with a simplified model of two flavor oscillations. In this framework we have the following mixing matrix, U, and oscillation probabilities, $P_{\alpha\beta}$,

$$U = \begin{pmatrix} c_{12}c_{13} & s_{12}c_{13} & s_{13}e^{-i\delta_{CP}} \\ -s_{12}c_{23}-c_{12}s_{13}s_{23}e^{i\delta_{CP}} & c_{12}c_{23}-s_{12}s_{13}s_{23}e^{i\delta_{CP}} & c_{13}s_{23} \\ s_{12}s_{23}-c_{12}s_{13}c_{23}e^{i\delta_{CP}} & -c_{12}s_{23}-s_{12}s_{13}c_{23}e^{i\delta_{\mathrm{CP}}} & c_{13}c_{23} \end{pmatrix} \tag{33}$$

$$P_{\alpha\beta} = \delta_{\alpha\beta} - 4 \sum_{k>j} \mathrm{Re}\left[U^*_{\alpha k} U_{\beta k} U_{\alpha j} U^*_{\beta j}\right] \sin^2\left(\frac{\Delta m^2_{kj} L}{4E}\right)$$

$$+ 2 \sum_{k>j} \mathrm{Im}\left[U^*_{\alpha k} U_{\beta k} U_{\alpha j} U^*_{\beta j}\right] \sin\left(\frac{\Delta m^2_{kj} L}{2E}\right) \tag{34}$$

where $s_{ij} \equiv \sin\theta_{ij}$ and $c_{ij} \equiv \cos\theta_{ij}$, and we know that physicality requires that $0 < P_{\alpha\beta} < 1$. Since the model is written in terms of sines and cosines it is impossible for any lone contribution to exceed one, so we need only worry about sums of terms exceeding one, which is ensured by the unitarity of the mixing matrix. Hence, in principle, arguments containing either θ_{ij} or Δm^2_{ij} can range between 0 and 2π. However, since the mixing parameters appear in periodic functions and our observable is linked to the total oscillation probability a simple way to reduce the range to that of physical interest is to neglect repeating solutions, i.e., to restrict the bounds to one period of the relevant functions. For the two neutrino case we have a $\sin^2\theta_{ij}$ term with a period of $\pi/2$, see Figure 3,

$$P_{\alpha\alpha} = 1 - P_{\alpha\beta} = 1 - \sin^2 2\theta \sin^2 \frac{\Delta m^2 L}{4E} \tag{35}$$

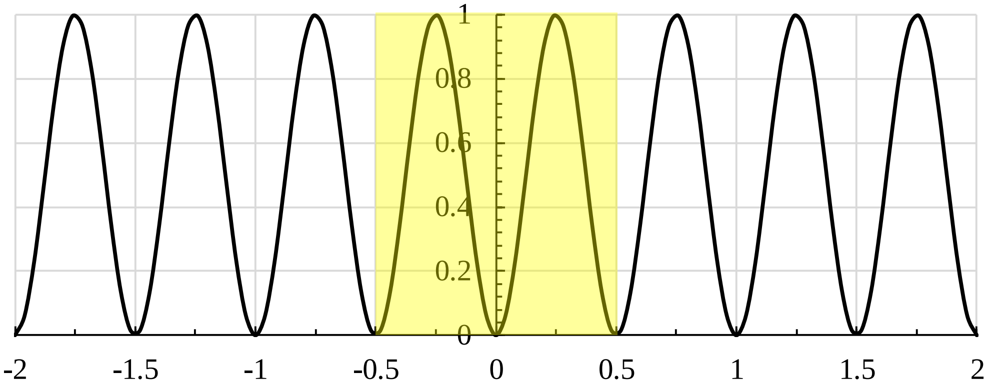

Figure 3. Plot of $\sin^2 2x$ as a function of x/π with region from $-\pi/2$ to $+\pi/2$ highlighted.

However, we note that we only need half of the period since the numeric values of the argument are the same (there is a numeric symmetry about $\pi/4$). Therefore the range of physical interest is $0 \le \theta_{ij} < \frac{\pi}{4}$, where we neglect the upper endpoint since the solutions repeat and keep the lower as more physically intuitive, i.e., that the physics does not exist for a zero parameter value while the physics does exist for a nonzero parameter value. The mass splitting argument goes like $\frac{\Delta m^2 L}{4E}$ so its period is larger giving a range of physical interest of $0 \le \frac{\Delta m^2 L}{4E} < 4\pi$. Given this and the conventions set on the mass orderings gives the hierarchy-independent, allowed mass-squared difference bounds in Table 2 (where, when possible, we have neglected repeating zero solutions).

Table 2. Conventions on bounds on mass-squared differences.

Convention	δm^2 Bounds	Δm^2 Bounds
1	$\left[0, +4\pi\frac{E}{L}\right)$	$\left[\delta m^2, +4\pi\frac{E}{L}\right)$

The usual way to go from two to three neutrinos is to parameterize the three neutrino mixing matrix as a product of three different two-neutrino mixings. As a result it is tempting to simply "add up" the bounds as a set of six parameters characterized by parameters in the two-neutrino case. However, this is not valid because of the appearance of linear terms. For linear sine functions the period is 2π, see Figure 4.

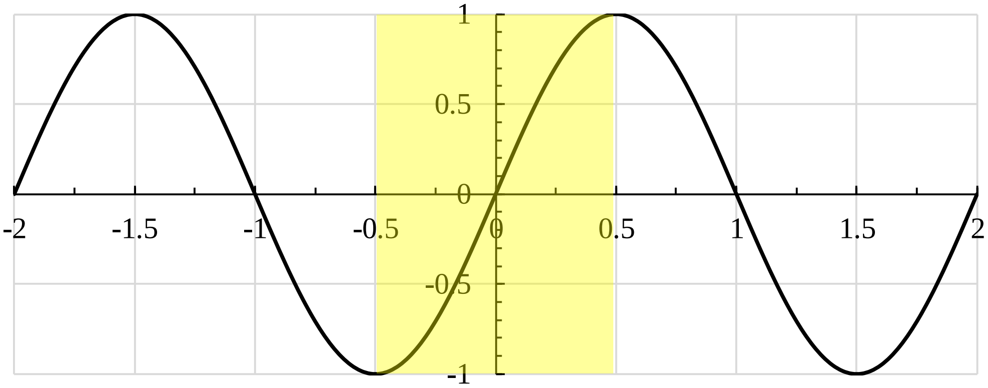

Figure 4. Sin *x* as a function of x/π with unique region from $-\pi/2$ to $+\pi/2$ highlighted.

However, this repeats numeric solutions. We also have the addition of sign information which is now relevant as sine is an odd function. The easiest way to capture all of the possible parameter space is to run the bounds from $-\pi/2$ to $\pi/2$ (with the endpoints included as they represent maximal mixings but with opposite signs) where, while the numerical value of the sine terms remains the same, the appearance of linear terms in the oscillation probability means that these represent different solutions, i.e., they affect the quantity ($P_{\alpha\beta}$) relevant to the final observable (N_α for disappearance experiments or N_β for appearance experiments). We could run the parameter space over only positive values from 0 to $3\pi/2$ but that doubles up on some of the parameter space and contains two zero points[3], which unnecessarily clutter the analysis results. It is cleaner to include only one zero and the full sign/value allowed angular space.

We note that the appearance of negative solutions is a direct result of moving to a three neutrino framework where linear angular terms appear (true for any θ_{ij} and for δ_{CP}), independent of whether or not a *CP*-phase is included. We can apply simple logic to see this: The oscillation probability depends on quartic products of the mixing matrix elements. Looking at the mixing matrix shows that angular functions appear in pairs or fours (if we include the *CP*-phase in the angles counted), such as in U_{e2} and $U_{\mu 2}$. Furthermore, looking at the full $P_{\mu e}$ probability will verify that terms linear in the mixing angles survive, hence, negative solutions are not trivial. Therefore, to affect a sign change in a quartic product requires at most a sign change in one angle: changing that of two or four angles cancels the effect, changing the sign of one angle has the same effect as changing that of three, and taking products of elements at most cancels the effect. This means that to capture the full allowed space we need only run one angle over a negative

---

[3] One could also use two disconnected parameter spaces from 0 to $\pi/2$ and π to $3\pi/2$. This requires running two analyses with disjointed graphs to capture the whole space.

parameter space. The convention has been to keep θ_{12} and θ_{23} positive valued, as well as θ_{13}, and leave negative values for the *CP*-phase. However, since we cannot guarantee the existence of *CP*-violation in neutrino oscillations, but we have confirmed three-neutrino mixing, and since, even without a nonzero *CP*-phase, negative valued solutions exist, this convention is potentially dangerous. If the *CP*-phase proves to be zero there is still a residual negative parameter space that must be explored.

As a result, there are six conventions which offer full coverage of the mixing angle-*CP* phase space, see Table 3. Only one mixing angle needs the cited bounds, the other two may run from 0 to $\pi/2$, and we are free to choose which mixing angle contains the negative-parameter space (again, when possible, we have neglected repeating zero solutions).

Table 3. Alternative conventions on θ_{13}-δ_{CP} space.

Convention	θ_{ij} Bounds	δ_{CP} Bounds
1	$\left[-\frac{\pi}{2}, +\frac{\pi}{2}\right]$	$\left[-\frac{\pi}{2}, +\frac{\pi}{2}\right]$
2	$\left[-\frac{\pi}{2}, +\frac{\pi}{2}\right]$	$[0, \pi)$
3	$\left[0, +\frac{3\pi}{2}\right]$	$[0, +2\pi)$
4	$\left[0, +\frac{3\pi}{2}\right]$	$(-\pi, +\pi)$
5	$\left[0, +\frac{\pi}{2}\right]$ and $\left(+\pi, +\frac{3\pi}{2}\right]$	$[0, +2\pi)$
6	$\left[0, +\frac{\pi}{2}\right]$ and $\left(+\pi, +\frac{3\pi}{2}\right]$	$(-\pi, +\pi)$

We note that most references cite the allowed θ_{ij} space as 0 to $\pi/2$, which neglects the negative-valued solutions. These negative solutions are, however, usually retained for δ_{CP} where the convention is to run δ_{CP} over 0 to 2π or $-\pi$ to π. This, however, introduces a degeneracy between $(-\delta_{CP}, +\theta_{13})$ and $(+\delta_{CP}, -\theta_{13})$ solutions and neglects $(-\theta_{13}, -\delta_{CP})$ solutions all together, i.e., it drops a third of the allowed parameter space. It is also possible to accidentally neglect half the parameter space using this option (the $-\theta_{13}$ solutions for the case of no *CP*-violation), though this is avoided if a purely quadratic oscillation approximation is used or if linear effects are negligible in the region of interest. For the vacuum case we also note that there is a resulting degeneracy between $\{(-\theta_{13}, \text{NH}), (+\theta_{13}, \text{IH})\}$ and likewise $\{(-\theta_{13}, \text{IH}), (+\theta_{13}, \text{NH})\}$ pairs because of the sign change when switching between hierarchies. We will discuss this much more later.[4] We also point out that there is no successful transformation between the conventions for $\theta_{ij} \in \langle -\pi/2, \pi/2\rangle$ and $\delta_{CP} \in \langle 0, \pi\rangle$ and $\theta_{ij} \in \langle 0, \pi/2\rangle$ and either $\delta_{CP} \in \langle 0, 2\pi\rangle$ or $\delta_{CP} \in \langle -\pi, 2\pi\rangle$ as these do not represent the same allowed space (the second is physically reduced) and there is a degeneracy between joint regions of interchanging sign of θ_{13} and sign of δ_{CP} that cannot be lifted without additional physics being included (namely matter effects, as we shall show later).

---

[4] We note that both Gluza and Zralek [54] and Latimer and Ernst [55] make statements when discussing the bounds on the mixing angles that hint at the existence of this additional symmetry between the mixing angle and mass-squared difference, but neither set of authors follows up on the implications in their publication. This was additional motivation for the present work.

Summary of Bounds and Mappings

For the present work we choose to use the following convention for our bounds and mappings:

Table 4. New bounds and mapping conventions used in this work.

Mixing Property	New Convention Used in This Work
θ_{13}	$\langle -\pi/2 , \pi/2\rangle$
θ_{12}, θ_{23}	$\langle 0 , \pi/2\rangle$
δ_{CP}	$\langle 0 , \pi\rangle$
$\left\|\Delta m_{ij}^2\right\|$	$\langle 0 , \infty\rangle$
Normal Hierarchy	$\Delta m_{31}^2 = \Delta m_{31}^2$
Inverse Hierarchy	$\Delta m_{31}^2 = -\Delta m_{31}^2 + \Delta m_{21}^2$

In comparison, the bounds traditionally seen in the neutrino oscillation phenomenology literature are:

Table 5. Traditional bounds and mapping found in the literature.

Mixing Property	Traditional Convention Used in Literature
θ_{13}	$\langle 0 , \pi/2\rangle$
θ_{12}, θ_{23}	$\langle 0 , \pi/2\rangle$
δ_{CP}	$\langle 0 , 2\pi\rangle$
$\left\|\Delta m_{ij}^2\right\|$	$\langle 0 , \infty\rangle$
Normal Hierarchy	$\Delta m_{31}^2 = \Delta m_{31}^2$
Inverse Hierarchy	$\Delta m_{31}^2 = -\Delta m_{31}^2$

However, as Harari *et al.* [56] pointed out when they first established what may be called the traditional bounds in the analogous quark mixing case: “A clever selection of a specific set of angles and phases has no fundamental theoretical importance. All choices are mathematically equivalent. A ‘good choice’ is mostly a matter of convenience, but it may also shed some light on important qualitative issues” (p. 123).

Since the convention presented in Table 4 is the simplest way to include the full physics and produces a single, continuous parameter space to search and a single, continuous allowed region when plotting δ_{CP} versus θ_{13} we find it to be the most convenient choice.[5] Therefore, we take bounds on θ_{13} such that the negative solution space is included independent of whether or not the *CP*-phase is nonzero (or included in the analysis). This is particularly useful since linear in θ_{13} terms are well-known and since the value of θ_{13} has been shown to be larger than expected so the effect of sign information in θ_{13} is discernible in the oscillation probability. In other words, our knowledge of the existence of helpful qualitative features further inspired us to use the conventions in Table 4 rather than those traditionally found in the literature. On that note, we now turn to reviewing some of the interesting qualitative features that our use of novel bounds in an analysis brought to light in our earlier work on neutrino mixing parameters.

---

[5] We also note, again, that the conventions presented in both tables are equally valid in both vacuum and matter [55].

Review: Previous Work Using New Paradigm

In our earlier work (see [57], [58], [59], [60], [61], [62], [63]), based on these new bounds, we noticed a number of novel features of the oscillation probability, which in turn impacts the extraction of parameters during analysis. These included linear in θ_{13} effects, the resulting presence of four solutions in the case of *CP*-conservation, and the presence of a hidden symmetry within the four solutions. We go on to discuss each of these features in turn as the interplay between them is what makes this choice of bounds simultaneously sensitive to both the sign of θ_{13} and the neutrino mass hierarchy.

Linear Effects in the Oscillation Probability

Linear terms exist in the neutrino oscillation probability and will play a significant role in the paradigm used to interpret the data later on. Therefore, this section is devoted to a discussion of linear terms that exist and a brief overview of their importance. It also serves as a chronology of our group's work in this area and, by its natural progression, motivates the research undertaken in the present work, which is a natural continuation of our initial exploration of linear effects.

Latimer et al. 2004

Latimer and Ernst conducted the first global analysis using the novel bounds on θ_{13} in 2004 [57]. They analyzed the data in the three-neutrino framework, including the negative θ_{13} space. They included data from: Homestake chlorine, GALLEX/GNO, SAGE, SNO, SNO-salt, Chooz, KamLAND, and K2K in their analysis. Their final results were not symmetric about $\theta_{13} = 0$, indicating the existence of linear effects in θ_{13} that impacted the extraction of this mixing angle from the data. Their χ^2 analysis found two minima: a global minimum in positive θ_{13} and a local minimum in negative θ_{13}. This was a qualitative finding as they stressed that "…we built the model [of our data]…not to extract precise values of the oscillation parameters, but to examine features of the neutrino oscillation phenomenology in a semi-quantitative way…Here we use the model to investigate the role of the negative θ_{13} region" (p. 3). They concluded that "…the region $\theta_{13} < 0$ plays an important role in understanding the oscillation parameters for three-neutrino oscillations" (p. 4). Although their conclusion regarding the existence of a negative θ_{13} region, to which the data was sensitive, was demonstrated by this early work, their conclusion suggesting the negative θ_{13} space was important was not yet supported by concrete evidence.

Latimer et al. 2005

Therefore, the next logical step was to examine in more depth the existence and relevance of the negative θ_{13} region in the neutrino data available at that time. The results of this work were published by Latimer and Ernst [58] shortly after their initial pre-print noting the existence of a negative θ_{13} region for the *CP*-conserving case. This time they demonstrated that $P_{e\mu}$ and $P_{\mu\mu}$ exhibit significant linear dependence on θ_{13} in the limit of vacuum oscillations. For this work they conducted an analytical study of $P_{\alpha\beta}$ terms that are linear (first order) in θ_{13}. These terms are also proportional to sin δ_{CP} or cos δ_{CP}. Their study of the oscillation probability showed that at certain values of L/E δ_{CP} effects are suppressed for $\delta_{CP} = 0$ or π while θ_{13} linear effects are maximized.

They went on demonstrate that sign of θ_{13} effects are maximal when sin ϕ_{21} [$\phi_{21} = 1.267\Delta m^2_{21}L/E$] is maximal for cos $\delta_{CP} \sim 1$, i.e., CP is conserved. Hence, the maximal linear dependence of $P_{e\mu}$ and $P_{\mu\mu}$ on θ_{13} occurs at $\phi_{21} = \pi/2, 3\pi/2$. More importantly, $P_{e\mu}$ and $P_{\mu\mu}$ are linear in θ_{13} at this maximal ϕ_{21}: the linear terms dominate the quadratic terms at these ϕ_{ij}. As a result, they concluded that $P_{e\mu}$ and $P_{\mu\mu}$ have linear in θ_{13} effects. It should be noted that they focused much of their discussion on the region where these effects are maximal (L = 80km, E = 5-50 MeV), not at a baseline and energy matching experiments at that time.[6] Still, this work demonstrated where one could best measure θ_{13} including its sign, again supporting the conclusion that this region of negative θ_{13} space existed. More interestingly, the authors found that the inclusion of linear terms indicated θ_{13}-θ_{23} correlations that needed exploring, first evidence of the possible importance of this negative θ_{13} region. Also, they again stressed the advantages of using $\pm\theta_{13}$ bounds: (1) measurements of θ_{13} put it in a small asymmetric region around $\theta_{13} = 0$, and (2) doing so keeps δ_{CP} in the first two quadrants such that cos δ_{CP} terms can uniquely determine θ_{13}.

Roa et al. 2009

In Roa *et al*. [60] our group extended our study of linear effects by publishing the results of a full global analysis intended for quantitative extraction of oscillation parameters using our novel bounds on θ_{13}. Although the primary goal of this work was to showcase a new computational tool developed to analyze the atmospheric Super-K data, secondary goals included studying the impact of small effects, especially linear terms, on

---

[6] Though they did include one plot of the results of a χ^2 analysis of the world's data, again showing the two minima: one in each sign region of the θ_{13} parameter space.

extracting θ_{13} from data. Roa *et al.* pointed out that one needs to know θ_{13} for setting the size of effects to determine *CP* and the neutrino mass hierarchy. Therefore, they analyzed Super-K, K2K, MINOS, and Chooz in the *CP*-conserving case.

Their results showed that linear terms and matter effects lead to asymmetric bounds on the mixing angle θ_{13}. The analysis preferred a negative θ_{13} value for a three parameter fit (θ_{13}, θ_{23}, Δm^2_{32}). The source of this result was traced mostly to one angular bin in Super-K, which is long baseline (earth-crossing), low energy data. Linear effects combine constructively in this region for $+\theta_{13}$, but destructively for $-\theta_{13}$. The presence of a slight electron excess (the leptonic interaction partner to passing electron neutrinos actually observed in the Super-K detector) in low energy bins restricts the allowance of $+\theta_{13}$ solutions as it suppresses the extracted neutrino ratio. The linear term is negative in this energy region, hence, negative θ_{13} leads to an enhancement term, rather than a suppression term. In other words, they verified that linear effects, driven by the sign of θ_{13}, play a role in neutrino data. Furthermore, they showed that θ_{13}, at that time, was bounded by atmospheric (Super-K) data for the upper bound and by reactor (Chooz) data for the lower bound, contrary to the wide-spread belief that Chooz set both the lower and upper bound on θ_{13}. They also found that correlations between θ_{13} and θ_{23} were important: different octant solutions for θ_{23} could alternately compensate to enhance or suppress the *e*- excess, rather than θ_{13}. Therefore, this study offered true evidence for the importance of θ_{13} linear effects in the neutrino data. The authors also pointed out in their conclusion that future long baseline (LBL) data would most certainly be sensitive to these linear effects.

Cogswell 2011

This led Cogswell [62] to conduct a more in-depth study of the role played by the Chooz reactor experiment in setting the magnitude of θ_{13} and the long baseline MINOS experiment in setting the level of linear effects, in anticipation of more precise reactor and long baseline data regarding θ_{13} that was expected shortly. This work analyzed MINOS $P_{\mu e}$, Chooz (with the original and a revised electron antineutrino flux under debate at that time), and KamLAND, solar data, and Super-K data constraints, to study the impact of $\pm\theta_{13}$. This was a qualitative, rather than quantitative, exploratory study, as the primary data sets, MINOS and Chooz, were statistically poor (low counts and high backgrounds). However, at this time it was an open question as to whether or not θ_{13} was nonzero, as no data yet showed it to be so at a statistically significant level. As a result, long baseline and reactor data were under intense scrutiny as the best source for hints about θ_{13} and in preparation for a set of LBL and reactor experiments (T2K, Daya Bay, and Double Chooz) designed to measure θ_{13} that were expected to release data the following year.

Cogswell's [62] work showed that all data sets and their combinations indicated nonzero θ_{13}. Again, as with Roa *et al*. [60], Super-K dominated the global result and restricted the upper bound value while the MINOS accelerator data and the Chooz reactor data jointly set the global lower bound value of θ_{13}. While all sub-combinations of data sets involving Super-K preferred negative values of θ_{13}, combinations of the data that did not include Super-K also indicated negative values, suggesting that the global indication of a negative-valued θ_{13} was more than just a preference of the Super-K experiment. Furthermore, there were hints that data sets interacted in counterintuitive ways.

For example, the combination of the MINOS data, which is sensitive to terms linear in θ_{13}, and the Chooz data, which is only sensitive to terms quadratic in θ_{13}, still indicated a preference for negative θ_{13} despite the poor statistical quality of the MINOS data, indicating the power of linear θ_{13} effects (MINOS), provided θ_{13} turned out to be nonzero (Chooz). A second example of a counterintuitive interplay between data sets derived from the interaction between MINOS, Chooz, and the KamLAND+Solar data. Although MINOS and KamLAND+Solar alone indicated a positive value for the mixing angle θ_{13} and Chooz (reactor data) cannot distinguish the sign of θ_{13}, these sets in combination yielded a negative best fit value.

However, the qualitative nature of this study limited its utility as well as the more significant limitation that it only examined the extraction of θ_{13} for the normal hierarchy and not for the inverse hierarchy. Still, the nature of the findings led Cogswell to conclude that "…the inclusion of future, more significant long-baseline accelerator data will greatly enhance the findings from the world's data" (p. 50). It also reinforced the mounting evidence that the novel paradigm implemented within our collaboration of treating the *CP*-conserving case by setting $\delta_{CP} = 0$ and letting θ_{13} run over both positive and negative values might offer a useful way to analyze the world's upcoming, more precise data.

Four Solutions Picture

Our collaboration continued this work by conducting a re-analysis of the world's data when T2K published its first observation of electron neutrino appearance and shortly thereafter Daya Bay, RENO, and Double Chooz definitively measured nonzero θ_{13}.

During routine early work on this analysis we realized that in the *CP*-conserving picture, there exist four solutions.[7] This was a novel finding. To our knowledge previous published work only presented two solutions in the *CP*-conserving picture.

In numerous talks we discussed our preliminary findings as summarized at the time by Ernst *et al*. [52]. While looking at the $P_{\mu e}$ oscillation probability for the LBL data we were analyzing we recognized that T2K and MINOS have a two-fold degeneracy in the limit of $\theta_{13} \rightarrow 0$ in vacuum, see Figure 5 and Figure 6. In each of these Figures, although there are four solutions plotted, we only see two nearly degenerate curves: a blue-green pair (solid, dash) and a red-orange pair (dot, dot-dash). The curves are as follows: blue (solid) is NH and positive θ_{13}; green (dash) is IH and negative θ_{13}; orange (dot-dash) is NH and negative θ_{13}; and red (dot) is IH and positive θ_{13}.

---

[7] With no evidence of *CP*-violation, we chose to set δ_{CP} to zero and fixed all the remaining oscillation parameters to their best estimated values to simplify calculations.

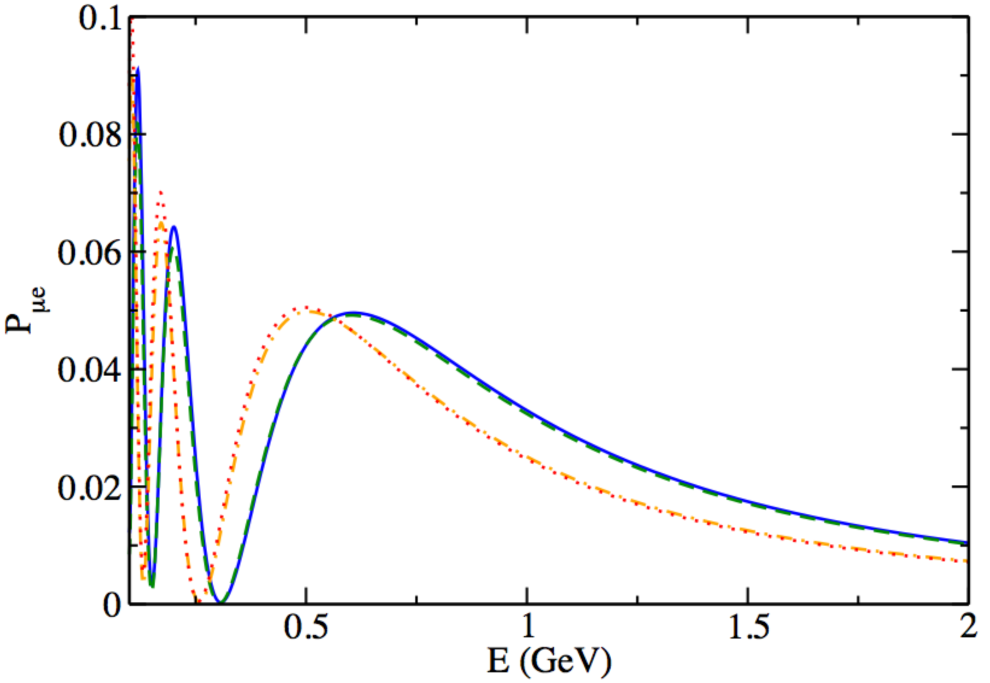

Figure 5. Four solutions for T2K appearance oscillation probability in vacuum. The curves are as follows: blue solid is NH and positive θ_{13}; green dash is IH and negative θ_{13}; orange dot-dash is NH and negative θ_{13}; and red dot is IH and positive θ_{13}.

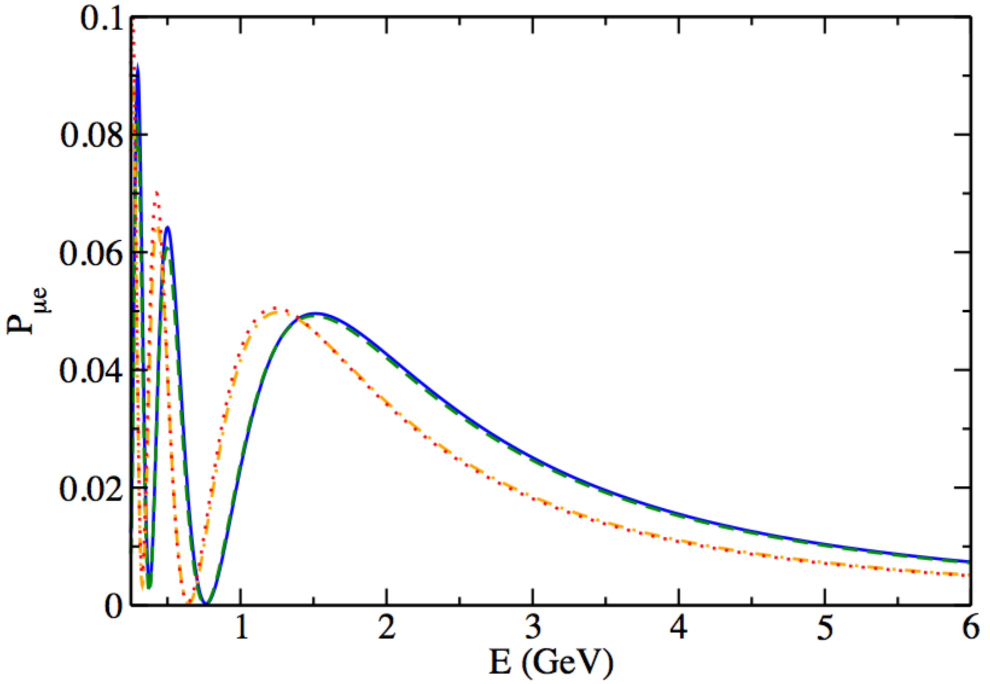

Figure 6. Four solutions for MINOS appearance oscillation probability in vacuum. The curves are as follows: blue solid is NH and positive θ_{13}; green dash is IH and negative θ_{13}; orange dot-dash is NH and negative θ_{13}; and red dot is IH and positive θ_{13}.

For $\theta_{13} = 0$ we would see only one curve, representing a four-fold degeneracy (see Figure 30 in Appendix A). However, as the graphs show, that four-fold degeneracy is partially broken by nonzero θ_{13}, though some degeneracy remains in vacuum. Matter effects break the two, two-fold symmetries as seen in Figure 7 and Figure 8, clearly yielding four possible solutions in the case of *CP*-conservation.

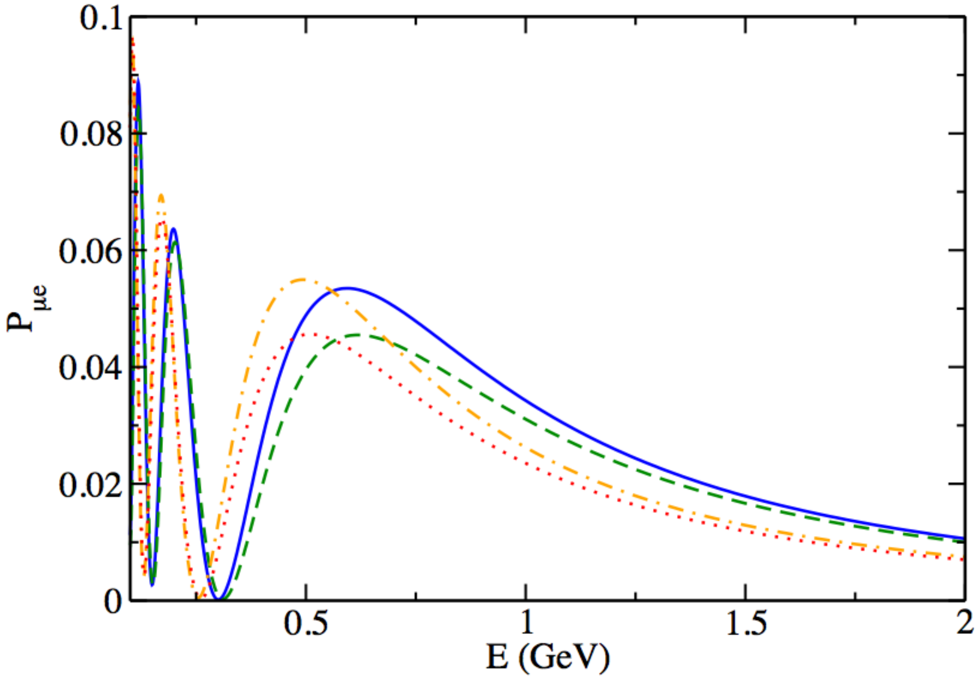

Figure 7. Four solutions for T2K appearance oscillation probability in matter. The curves are as follows: blue solid is NH and positive θ_{13}; green dash is IH and negative θ_{13}; orange dot-dash is NH and negative θ_{13}; and red dot is IH and positive θ_{13}.

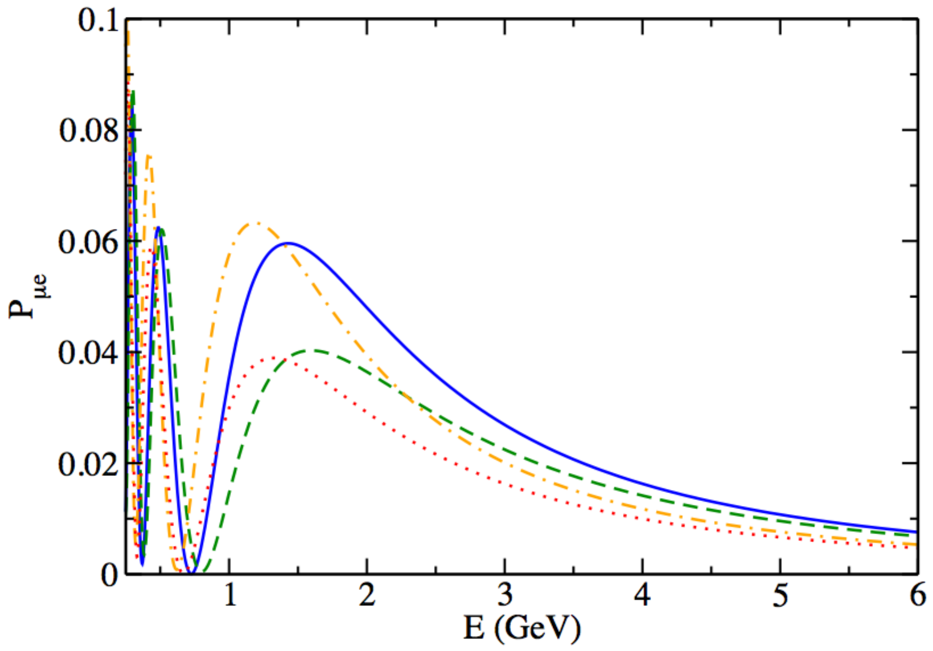

Figure 8. Four solutions for MINOS appearance oscillation probability in matter. The curves are as follows: blue solid is NH and positive θ_{13}; green dash is IH and negative θ_{13}; orange dot-dash is NH and negative θ_{13}; and red dot is IH and positive θ_{13}.

For the LBL data the magnitude of the $P_{\mu e}$ oscillation peaks is sensitive to the hierarchy, while the spectral position of peaks maintains the degeneracy. Including matter effects alters the peak heights, leaving the spectral positions nearly the same. This means that spectral-only information mostly leaves the two-fold vacuum degeneracy intact, identifying between sign of θ_{13} solutions. In contrast, peak height-only information leaves the other two-fold degeneracy nearly intact, identifying between hierarchies. Reactor experiments, measuring P_{ee}, have no sensitivity to the sign of θ_{13} (there are no linear effects because their oscillations are driven purely by the small mass scale) and no hierarchy effects (for the same reason). Furthermore, there are no matter effects in reactor experiments because they measure antineutrinos, so there is no change to peak heights. This makes reactor data insensitive to the four solutions, as seen in Figure 9. However, these experiments do set the magnitude of θ_{13} and so help to set the magnitude of effects that generate the four solutions picture so clearly in the long baseline data.

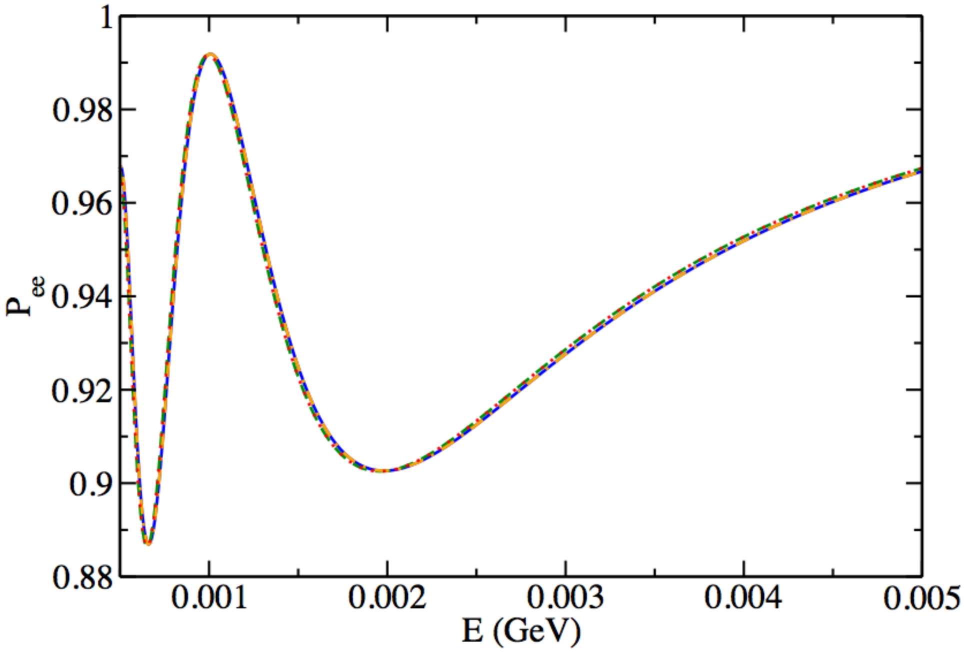

Figure 9. Four solutions for Daya Bay disappearance oscillation probability in matter. The curves are as follows: blue solid is NH and positive θ_{13}; green dash is IH and negative θ_{13}; orange dot-dash is NH and negative θ_{13}; and red dot is IH and positive θ_{13}.

Our findings at that time, as a result of the existence of four solutions and using a combination of T2K, MINOS, Super-K, Daya Bay, RENO, and Double Chooz can be summarized as follows: The statistics for T2K were so low and errors due to background on MINOS were so high that our analysis was unable to distinguish a preferred LBL solution. Our global findings preferred IH over NH solutions, with the IH, negative θ_{13} being most preferred. This result was driven by the preference of atmospheric data for negative θ_{13} and inverse hierarchy. T2K and MINOS are at the smallest L/E where hierarchy and linear effects occur, driven by interference between the two known mass scales. T2K's primary measurement is over the peaks ($E \sim [0.39, 0.9]$ GeV) so it is sensitive to both hierarchy and sign of θ_{13}. MINOS' primary measurement is just off the peak to the right toward higher energies ($E \sim [2, 4.5]$ GeV), so it is sensitive only to hierarchy. The quality of the fit, as captured by the value of the χ^2 at the minimum, was driven by spectral information and the location of the minimum was driven by peak height information. This led us to conclude that since T2K, MINOS, and NOνA are all sensitive to the four solutions, a combination of these data sets in future will make them better able to identify a preferred solution. Also we expected future LBL data with more counts and smaller errors to offer more information, which was a main motivator to continue our study, leading to more extensive work on exploring the existence of the *CP*-conserving four solutions picture.

Symmetries of the Oscillation Probability

The existence of four solutions and the clear degeneracy between solutions that appears in looking at plots of the oscillation probabilities led us to hunt for the underlying symmetry that drove the four solutions picture and was clearly maintained in vacuum and broken in matter. In this section we describe our findings. We also note that for completeness we have generated plots of the oscillation probability to check for symmetries and observe the level of linear and hierarchy effects for all of the experiments included in the global analysis conducted here. However, to streamline the discussion we have included only the most interesting ones in the main text. The remaining set of plots, as well as the details of the input parameters, are relegated to Appendix A.

Although the existence of parameter degeneracies for neutrino oscillation parameters have been studied[8] (see [9], [55], [64]), the existence of possible parameter symmetries involving the sign of trigonometric parameters in the oscillation probability have never been studied. This is understandable in light of the fact that their likelihood of existence was obscured: the unknown mass hierarchy parameter Δm^2 (large mass-splitting) not only changes sign but also magnitude when changing hierarchies, the unknown parameters θ_{13} and δ_{CP} were expected to be exceptionally small or zero, and no work had yet been published pointing out that θ_{13} could be positive or negative valued.

However, recently, θ_{13} was learned to be nonzero and larger than expected (see [10], [11], [12]). While using a parameter analysis that studied positive and negative valued θ_{13} solutions to try and learn the sign of θ_{13} using the new LBL appearance data, we became aware of the existence of possible sign symmetries between Δm^2_{31} and θ_{13}. The breaking of this symmetry showed a distinctive pattern and further study on our part showed that current LBL data was precise enough to distinguish between solutions based on the pattern of symmetry breaking and give insight into the mass hierarchy as well as θ_{13}. As a result of these findings, we undertook a never before done, systematic study of the existence of possible sign symmetries of the unknown remaining neutrino oscillation

---

[8] For degeneracies between $P_{\alpha\beta}$ and $P_{\bar{\alpha}\bar{\beta}}$ see [9]; for symmetries between mass-squared differences in different conventions see [65] and [64]; for symmetries among mixing angles see [55].

parameters (Δm^2_{31}, θ_{13}, and δ_{CP}) in the $P_{\mu e}$ oscillation probability[9] and a study of how those symmetries are broken in vacuum and matter.

Symmetry-Hunting Logic

Based on our previous work, our primary goal was to look for three- (Δm^2_{31} and θ_{13} and δ_{CP}) and two-parameter (all possible pairwise combinations of Δm^2_{31}, θ_{13}, and δ_{CP}) sign symmetries in the exact $P_{\mu e}$ vacuum oscillation probability.

The set of symmetries resulting solely from changing the sign of trigonometric terms in $P_{\mu e}$ can be determined from the bounds on parameters and the known parameter values. There are six oscillation parameters appearing in trigonometric arguments to consider:

1. Δm^2_{31}: Changing the argument of the Δm^2_{31} trigonometric terms is limited to just $\Delta m^2_{31} \rightarrow - \Delta m^2_{31}$ by the fact that Δm^2_{32} has been determined from the LBL disappearance data, which constrains the value of Δm^2_{31}.
2. Δm^2_{21}: The sign of Δm^2_{21} is set by convention as positive and the value of Δm^2_{21} has been determined from the solar data.
3. θ_{12} and θ_{23}: The allowed bounds are $[0, \pi/2]$.
4. θ_{13} and δ_{CP}: There are two different conventions on the bounds. Either $\theta_{13} = [-\pi/2, \pi/2]$ and $\delta_{CP} = [0, \pi)$, or, $\theta_{13} = [0, \pi/2]$ and $\delta_{CP} = [0, 2\pi]$.

Based on this information only seven sign symmetries are possible. These are:

---

[9] The lack of previous evidence of large linear terms in either the reactor $P_{\bar{e}\bar{e}}$ or the accelerator $P_{\mu\mu}$ led us to focus our analytical investigation solely on $P_{\mu e}$.

1. $\Delta m^2_{31} \rightarrow - \Delta m^2_{31}$ and $\theta_{13} \rightarrow - \theta_{13}$ and $\delta_{CP} \rightarrow \pi - \delta_{CP}$
2. $\Delta m^2_{31} \rightarrow - \Delta m^2_{31}$ and $\theta_{13} \rightarrow - \theta_{13}$ and $\delta_{CP} \rightarrow \pi/2 - \delta_{CP}$
3. $\Delta m^2_{31} \rightarrow - \Delta m^2_{31}$ and $\theta_{13} \rightarrow - \theta_{13}$
4. $\Delta m^2_{31} \rightarrow - \Delta m^2_{31}$ and $\delta_{CP} \rightarrow \pi - \delta_{CP}$
5. $\Delta m^2_{31} \rightarrow - \Delta m^2_{31}$ and $\delta_{CP} \rightarrow \pi/2 - \delta_{CP}$
6. $\theta_{13} \rightarrow - \theta_{13}$ and $\delta_{CP} \rightarrow \pi - \delta_{CP}$
7. $\theta_{13} \rightarrow - \theta_{13}$ and $\delta_{CP} \rightarrow \pi/2 - \delta_{CP}$

where $\Delta m^2_{31} \rightarrow - \Delta m^2_{31}$ is approximately the same as a hierarchy change, i.e., NH → IH. There are two trivial symmetries for $\theta_{13} = \pm\pi/2$, but the measurement of $\theta_{13} = 0.15$ rads rules out those solutions.

Examination of Symmetries

We start with the $P_{\mu e}$ vacuum oscillation probability:

$$P^{vac}_{\mu e} = \sin^2 2\theta_{12}\, c^2_{23} c^2_{13} \sin^2 \alpha\Delta \;-\; \frac{1}{2} \sin 2\theta_{12} \sin 2\theta_{13} \sin 2\theta_{23}\, c_{13} \sin \alpha\Delta$$
$$\times \{\sin[(\alpha\text{-}2)\Delta\text{-}\delta_{CP}] + \sin \delta_{CP} \cos \alpha\Delta - \cos 2\theta_{12} \cos \delta_{CP} \sin \alpha\Delta\}$$
$$+ \frac{1}{4} \sin^2 2\theta_{13}\, s^2_{23} [2 - \sin^2 2\theta_{12} \sin^2 \alpha\Delta - 2c^2_{12} \cos 2\Delta - 2s^2_{12} \cos 2(\alpha\text{-}1)\Delta] \tag{36}$$

where,

$$\alpha \equiv \frac{\Delta m^2_{21}}{\Delta m^2_{31}} \tag{37}$$

$$\Delta \equiv \frac{\Delta m^2_{31} L}{4E} \tag{38}$$

The only way to change the sign of sin x or cos x is via the argument x, see Table 6.

Table 6. Effect of argument maps on sine and cosine.

Mapping	Effect on sin x	Effect on cos x
$x \rightarrow -x$	-sin x	cos x
$x \rightarrow \pi + x$	-sin x	-cos x
$x \rightarrow \pi - x$	sin x	-cos x
$x \rightarrow \pi/2 - x$	cos x	sin x

Multiplying out $P_{\mu e}$ terms and using trigonometric substitutions of the form sin(A±B) and cos(A±B) to further expand terms allows us to separate those terms that would be impacted by a sign change in Δm^2_{31}, θ_{13}, or δ_{CP} (contained in the sum term) from those that would not,

$$P^{vac}_{\mu e} = \sin^2 2\theta_{12}\, c^2_{23} c^2_{13} \sin^2 \alpha\Delta \;+\; \frac{1}{4}\sin^2 2\theta_{13}\, s^2_{23}\left[2 - \sin^2 2\theta_{12} \sin^2 \alpha\Delta\right] + \sum_{i=1}^{9} S_i T_i \tag{39}$$

Listing the important sub terms and prefactors for later use gives:

Sign-Independent Prefactors (S_i)

$$S_1 = \frac{1}{2}\sin 2\theta_{12} \sin 2\theta_{23} \sin^2 \alpha\Delta \tag{40}$$

$$S_2 = \frac{1}{2}\sin 2\theta_{12} \sin 2\theta_{23} \sin \alpha\Delta \cos \alpha\Delta \tag{41}$$

$$S_3 = S_2 \tag{42}$$

$$S_4 = S_1 \tag{43}$$

$$S_5 = S_2 \tag{44}$$

$$S_6 = \frac{1}{2}\sin 2\theta_{12} \sin 2\theta_{23} \cos 2\theta_{12} \sin^2 \alpha\Delta \tag{45}$$

$$S_7 = \frac{1}{2}\sin^2 2\theta_{13}\, s_{23}^2 c_{12}^2 \tag{46}$$

$$S_8 = \frac{1}{2}\sin^2 2\theta_{13}\, s_{23}^2 s_{12}^2 \cos 2\alpha\Delta \tag{47}$$

$$S_9 = \frac{1}{2}\sin^2 2\theta_{13}\, s_{23}^2 s_{12}^2 \sin 2\alpha\Delta \tag{48}$$

Sign-Dependent Sub Terms (T_i)

$$T_1 = -\ \sin 2\theta_{13} \cos \theta_{13} \cos 2\Delta \cos \delta_{CP} \tag{49}$$

$$T_2 = +\sin 2\theta_{13} \cos \theta_{13} \sin 2\Delta \cos \delta_{CP} \tag{50}$$

$$T_3 = +\ \sin 2\theta_{13} \cos \theta_{13} \cos 2\Delta \sin \delta_{CP} \tag{51}$$

$$T_4 = +\ \sin 2\theta_{13} \cos \theta_{13} \sin 2\Delta \sin \delta_{CP} \tag{52}$$

$$T_5 = -\ \sin 2\theta_{13} \cos \theta_{13} \sin \delta_{CP} \tag{53}$$

$$T_6 = +\ \sin 2\theta_{13} \cos \theta_{13} \cos \delta_{CP} \tag{54}$$

$$T_7 = +\ \cos 2\Delta \tag{55}$$

$$T_8 = +\ \cos 2\Delta \tag{56}$$

$$T_9 = +\ \sin 2\Delta \tag{57}$$

In the following tables, we systematically check the effect of implementing each of the above mappings on the sub terms of the oscillation probability. Since T_7 and T_8 are of the same form, we only check T_7. The set of possible symmetries are:

1. $\Delta m_{31}^2 \rightarrow -\ \Delta m_{31}^2$ and $\theta_{13} \rightarrow -\ \theta_{13}$ and $\delta_{CP} \rightarrow \pi - \delta_{CP}$
2. $\Delta m_{31}^2 \rightarrow -\ \Delta m_{31}^2$ and $\theta_{13} \rightarrow -\ \theta_{13}$ and $\delta_{CP} \rightarrow \pi/2 - \delta_{CP}$
3. $\Delta m_{31}^2 \rightarrow -\ \Delta m_{31}^2$ and $\theta_{13} \rightarrow -\ \theta_{13}$

4. $\Delta m_{31}^2 \rightarrow - \Delta m_{31}^2$ and $\delta_{CP} \rightarrow \pi - \delta_{CP}$
5. $\Delta m_{31}^2 \rightarrow - \Delta m_{31}^2$ and $\delta_{CP} \rightarrow \pi/2 - \delta_{CP}$
6. $\theta_{13} \rightarrow - \theta_{13}$ and $\delta_{CP} \rightarrow \pi - \delta_{CP}$
7. $\theta_{13} \rightarrow - \theta_{13}$ and $\delta_{CP} \rightarrow \pi/2 - \delta_{CP}$

We list the symmetry tables in order of minimum number of term sign changes and interchanges to maximum number.

Table 7. Symmetry properties of θ_{13} and δ_{CP}.

For $\theta_{13} \rightarrow - \theta_{13}$ and $\delta_{CP} \rightarrow \pi - \delta_{CP}$	
$T_1 \rightarrow T_1$	$T_5 \rightarrow - T_5$
$T_2 \rightarrow T_2$	$T_6 \rightarrow T_6$
$T_3 \rightarrow - T_3$	$T_7 \rightarrow T_7$
$T_4 \rightarrow - T_4$	$T_9 \rightarrow T_9$

Table 8. Symmetry properties of Δm^2, θ_{13}, and δ_{CP}.

For $\Delta m_{31}^2 \rightarrow - \Delta m_{31}^2$ and $\theta_{13} \rightarrow - \theta_{13}$ and $\delta_{CP} \rightarrow \pi - \delta_{CP}$	
$T_1 \rightarrow T_1$	$T_5 \rightarrow - T_5$
$T_2 \rightarrow - T_2$	$T_6 \rightarrow T_6$
$T_3 \rightarrow - T_3$	$T_7 \rightarrow T_7$
$T_4 \rightarrow T_4$	$T_9 \rightarrow - T_9$

Table 9. Symmetry properties of Δm^2 and δ_{CP}.

For $\Delta m^2_{31} \rightarrow - \Delta m^2_{31}$ and $\delta_{CP} \rightarrow \pi - \delta_{CP}$	
$T_1 \rightarrow - T_1$	$T_5 \rightarrow T_5$
$T_2 \rightarrow T_2$	$T_6 \rightarrow - T_6$
$T_3 \rightarrow T_3$	$T_7 \rightarrow T_7$
$T_4 \rightarrow - T_4$	$T_9 \rightarrow - T_9$

Table 10. Symmetry properties of Δm^2 and θ_{13}.

For $\Delta m^2_{31} \rightarrow - \Delta m^2_{31}$ and $\theta_{13} \rightarrow - \theta_{13}$	
$T_1 \rightarrow - T_1$	$T_5 \rightarrow - T_5$
$T_2 \rightarrow T_2$	$T_6 \rightarrow - T_6$
$T_3 \rightarrow - T_3$	$T_7 \rightarrow T_7$
$T_4 \rightarrow T_4$	$T_9 \rightarrow - T_9$

Table 11. Symmetry properties of Δm^2, θ_{13}, and δ_{CP}.

For $\Delta m^2_{31} \rightarrow - \Delta m^2_{31}$ and $\theta_{13} \rightarrow - \theta_{13}$ and $\delta_{CP} \rightarrow \pi/2 - \delta_{CP}$	
$T_1 \rightarrow T_3$	$T_5 \rightarrow T_6$
$T_2 \rightarrow T_4$	$T_6 \rightarrow T_5$
$T_3 \rightarrow T_1$	$T_7 \rightarrow T_7$
$T_4 \rightarrow T_2$	$T_9 \rightarrow - T_9$

Table 12. Symmetry properties of θ_{13} and δ_{CP}.

For $\theta_{13} \rightarrow - \theta_{13}$ and $\delta_{CP} \rightarrow \pi/2 - \delta_{CP}$	
$T_1 \rightarrow T_3$	$T_5 \rightarrow T_6$
$T_2 \rightarrow - T_4$	$T_6 \rightarrow T_5$
$T_3 \rightarrow T_1$	$T_7 \rightarrow T_7$
$T_4 \rightarrow - T_2$	$T_9 \rightarrow T_9$

Table 13. Symmetry properties of Δm^2 and δ_{CP}.

For $\Delta m^2_{31} \rightarrow -\Delta m^2_{31}$ and $\delta_{CP} \rightarrow \pi/2 - \delta_{CP}$	
$T_1 \rightarrow -T_3$	$T_5 \rightarrow -T_6$
$T_2 \rightarrow -T_4$	$T_6 \rightarrow -T_5$
$T_3 \rightarrow -T_1$	$T_7 \rightarrow T_7$
$T_4 \rightarrow -T_2$	$T_9 \rightarrow -T_9$

It is easy to see from the above tables that none of the mappings produce exact symmetries. However, many are capable of producing near-symmetries depending on the size of various terms as determined by the prefactors for each term, as well as by the size of the magnitude difference of Δm^2_{31} in each hierarchy. Also, the variety of effects of each symmetry on $P_{\mu e}$ are different such that the symmetry-breaking pattern is specific to each mapping. The above discussion identifies the possible existence of sign symmetries. These symmetries only survive to the extent that the prefactors of exchanged terms are the same and to the extent that other non-symmetric terms are small. The degree and pattern of symmetry breaking is the information in which we are primarily interested, as it will have the most value when analyzing real data to try and estimate unknown parameters. We discuss the most useful symmetries below.

The most promising symmetries are those involving a combination of $\Delta m^2_{31} \rightarrow -\Delta m^2_{31}$ and $\theta_{13} \rightarrow -\theta_{13}$ and $\delta_{CP} \rightarrow \pi - \delta_{CP}$. These involve sign changes of sub terms in the oscillation probability. The degree of symmetry breaking is therefore determined by the relative size of terms. This means that the breaking of the symmetries will have the overall effect of increasing or decreasing the magnitude of the oscillation probability, i.e., the peak height of the first big oscillation peak. The degree of symmetry breaking is also determined by the difference between NH(Δm^2_{31}) and IH(Δm^2_{31}), i.e., the spectral location of the first big oscillation peak.

Readers may wonder why we consider sign symmetries involving δ_{CP} since we have, throughout this work, assumed a *CP*-conserving scenario. We do so for completeness with the understanding that not all groups utilize the same bounds convention, such that although sign symmetries appear within our *CP*-conserving framework via θ_{13}, for others they may appear via δ_{CP}. We stress that these are, of course, equivalent and equally valid pictures. For now, we continue to utilize the paradigm of setting $\delta_{CP} = 0$ and letting sign information be contained in θ_{13} and turn to looking at the connection between the resulting symmetry under the simultaneous interchange of the mass hierarchy ($\Delta m^2_{31} \rightarrow -\Delta m^2_{31}$) and the sign of θ_{13} ($\theta_{13} \rightarrow -\theta_{13}$) and the four solutions picture.

Significance of Sign Symmetry

Although at least two other previous works hint at the existence of this symmetry, neither followed up on it with published work. Latimer *et al.* [55] comments, "Let us take as a typical set of parameters derived from oscillation data [parameters using $+\theta_{13}$]. This set of mass-squared differences is an example of the regular [normal] hierarchy. It is known that there is a set of parameters with an inverted mass hierarchy that yield oscillation probabilities which are nearly equivalent…we may calculate these nearly equivalent parameters [which include $-\theta_{13}$]" (p. 3). Similarly Gluza *et al.* [54] comments that "…we can find a practical reason for introducing $\pm\delta m^2$'s. We have just shown that using various schemes is equivalent to using the (123) [normal hierarchy] scheme with different values of θ_{ij} angles in the parameter space" (p. 165).

However, we were the first to point out in numerous talks summarized by Ernst *et al.* [53] that the symmetry exists and that it impacts the analysis of the data in a *CP*-conserving framework. We analyzed the data over θ_{13}, θ_{23}, Δm^2_{32}, marginalizing the solar parameters. We found that MINOS neutrino disappearance data dominated the Δm^2_{32} final result, Daya Bay dominated the θ_{13} final result, and Super-K solar dominated the θ_{23} final result. The inverse hierarchy was preferred by the value of θ_{13}. "We…[found] four distinct and isolated minima, one for each value of the hierarchy and the sign of θ_{13}, as implied by the symmetry" (p. 8). The global preference was for the inverse hierarchy and negative θ_{13}.

Therefore, this work indicated the link between the neutrino mass hierarchy and the sign of θ_{13} via linear terms and as a result of the near-symmetry between sign interchanges of the large mass-squared difference and the mixing angle θ_{13}. It also continued our group's ongoing program to seek out the impact of linear terms in the oscillation probability on the extraction of phenomenological parameters using a bounds paradigm not used by other groups. Without the novel bounds paradigm, we might not have identified this sign-based symmetry, since so much of the field has focused on numeric-based symmetries. Without the symmetry, we might not have discovered the link between the neutrino mass hierarchy and the sign of the surprisingly large mixing angle θ_{13}. Therefore, we concluded that the novel bounds paradigm merited continued use and that the pattern of matter symmetry breaking in accelerator data was a meaningful feature that impacted the extraction of oscillation parameters from the global data.

Other Relevant Previous Work

A few other studies previously done by our group merit mentioning here as they will help round out the picture of neutrino oscillations within the new paradigm including $\pm\theta_{13}$. We briefly review these works below.

Neutrino Mass Hierarchy

Roa *et al*. [61] performed a study using the novel paradigm to determine the effect of hierarchy on parameter extraction and hierarchy preference. For large θ_{13} interference terms that can be used to determine the neutrino mass hierarchy become larger, though they are still negligible in vacuum. The authors pointed out that, "If θ_{13} is sufficiently nonzero, then matter effects provide the most promising avenue by which one might determine neutrino hierarchy" (p. 1). For earth-crossing neutrinos, resonances occur (MSW-type) due to the matter density in the core and mantle. The resonances only exist for neutrinos in the normal hierarchy or for antineutrinos in the inverse hierarchy. Therefore, in principle, for large enough θ_{13}, data at the L/E and matter density where resonances can occur could distinguish the absence/presence of resonances to determine the hierarchy. This occurs in the Super-K data. However, they also pointed out that the resonances give information about the hierarchy and magnitude of θ_{13}, but not the sign of θ_{13} (linear terms are too small in the resonance region for atmospheric data). Therefore, they conducted a three parameter fit (Δm_{32}^2, θ_{23}, θ_{13}) with both hierarchies including Super-K data (sensitive to resonances) and MINOS and Chooz data (sensitive to θ_{13}). Many of the results mirror those already discussed, so we neglect repeating them here and focus only on those findings regarding the hierarchy. They found negative nonzero θ_{13} was preferred for both hierarchies, i.e., this preference for negative θ_{13} was hierarchy independent and due to the Super-K sub-GeV *e*- excess. They sourced the hierarchy differences between results for each parameter (such as the Δm_{32}^2 being higher for the IH than for the NH) as due to MSW matter effects. They concluded that the data at that time "[had] statistically insignificant implications for…[the] neutrino hierarchy" (p. 3) and that to get statistically significant implications from atmospheric data would need large nonzero mixing angles and either a reduction of the error bars or an increase in the data.

Mixing Angle Correlations

Latimer and Ernst [59] undertook an analytic study of the relationship between the mixing angles θ_{13} and θ_{23}. Two big questions in the field were: is θ_{13} nonzero and how close to $\pi/4$ is θ_{23}? They found that at the ideal L/E to maximize sign of θ_{13} effects there were correlations between θ_{13} and θ_{23} measurements. They used the novel parameterization of treating θ_{23} using the parameter ϵ, where $\theta_{23} = \pi/4+\epsilon$, such that negative ϵ indicates θ_{23} lies in the first octant and positive ϵ indicates θ_{23} lies in the second octant. At the time, this was seen as a way to quantify the deviation of θ_{23} from maximal mixing at $\pi/4$. They used mock data and a Gaussian chi-squared to assess how a measurement of P_{ee} and $P_{\mu\mu}$ at 270 MeV and 4000km (the ideal baseline to maximize linear θ_{13} effects) would affect the extraction of θ_{13} and θ_{23}. In particular, they were seeking a possible link between the sub-GeV *e*- excess in Super-K and their model. They found the following correlation: if the excess proved true, i.e., remained statistically significant in future data, then for $\theta_{13} = 0$, θ_{23} lay in the first octant, while for θ_{23} maximal, θ_{13} was found to be positive. They also noted "…that these mock data indicate a preference for positive θ_{13} and first octant θ_{23}" (p. 6). Therefore, this work suggested a link between sign of θ_{13} as well as its magnitude and θ_{23}. The neutrino mass hierarchy was found to play a negligible role, as a 3% correction to θ_{13}.

Escamilla-Roa *et al.* [63] then performed a quantitative study that, in part, examined the correlations between mixing angles. This was a three-neutrino analysis with Super-K, Chooz, K2K, and MINOS and they found a θ_{13}-ϵ correlation. A preference for negative θ_{13} allowed θ_{23} to be in the second octant and changed the shape of the θ_{13}-θ_{23} allowed region. They saw some sensitivity to the octant from Super-K, even though it is a small effect: because it is correlated with θ_{13}, which is also a small effect, the sensitivity was not washed out. Super-K dominated the θ_{23} measurement so much that adding in other experiments hardly changed the results. Their analysis found a statistically insignificant indication of positive ϵ, i.e., θ_{23} greater than $\pi/4$, the error on θ_{23} depended on the value of θ_{13}, and a negative θ_{13} was preferred with asymmetric bounds. K2K, Chooz, and MINOS gave symmetric results (no linear term sensitivity), so the asymmetry was due to Super-K. The allowed region for θ_{13} and θ_{23} favored negative θ_{13} so long as linear terms were included in the calculation (reinforcing their importance). The authors concluded by saying, "No longer is the contour symmetric about a particular value of θ_{23}; hence, the true value of this mixing angle will impact the allowed region for the θ_{23} mixing angle. In particular, the allowed region for θ_{23} shrinks as θ_{13} approaches positive values. In the future, should a reactor neutrino experiment confirm a nonzero value for $|\theta_{13}|$, it will have interesting consequences for the allowed value of θ_{23}" (p. 6).

Implications: Synergy between Mass Hierarchy and Sign of θ_{13}

We are now in a position to summarize the present picture of neutrino oscillations within the unique framework of setting the *CP*-phase to zero and letting the mixing angle θ_{13} run over the positive and negative valued parameter space from $[-\pi/2, \pi/2]$. In Table 14 we summarize the set of small effects, discussed in this chapter, that are detectable using this unique paradigm. Based on our previous work, we can now write down a "chain of effect" on the extraction of various neutrino phenomenological properties.

The Daya Bay reactor data (statistically strongest reactor data set) offers the strongest constraint on the magnitude of θ_{13}. Knowing the magnitude of θ_{13}: (1) sets the peak spectrum for the long baseline data analysis, (2) sets the scale of linear terms in the long baseline and atmospheric data analysis, and (3) sets correlations between θ_{13} and θ_{23} in joint reactor and long baseline analysis. Having set the location of the peak spectrum leads to the T2K $P_{\mu e}$ long accelerator data setting the hierarchy (as the statistically dominant long baseline data set), which in turn leads to setting the sign of θ_{13}, which in turn leads to a preference for θ_{23} via correlations.

Roa *et al*.'s [61] hierarchy work lacked information about the sign of θ_{13} because there was not enough LBL data and no set magnitude of θ_{13} because not enough reactor data had been gathered yet. Hence, the hierarchy link was not strong in this early work. Also we were not aware of the symmetry. Hence, Cogswell's [62] work neglected two solutions out of four and so, unbeknownst to us at that time, missed out on a big part of the full picture. Similarly, at the time that work was carried out we still lacked LBL data for the sign of θ_{13} and reactor data for the magnitude of θ_{13}. However, our later discovery of the symmetry linked the hierarchy and linear in θ_{13} terms as dependent physics. Hence, this earlier work clearly needed updating, a main driver of the present research.

Table 14. Small effects detectable within new bounds paradigm.

Mixing Angle Correlations

- Sign of θ_{13} affects extracted octant of θ_{23} and its error bars
- For negative θ_{13}, first octant θ_{23} preferred
- For positive θ_{13}, second octant θ_{23} preferred

Atmospheric Resonances

- Fitting electron excess in earth-crossing, sub-Gev Super-K bins affects extraction of θ_{13}
- Normal hierarchy solutions require positive θ_{13}
- Inverse hierarchy solutions require negative θ_{13}

Neutrino Mass Hierarchy

- Peak heights change for first big oscillation peak in long baseline appearance data
- Resolved by determining absolute neutrino flux with small errors

Sign of θ_{13}

- Peak spectrum shifts for first big oscillation peak in long baseline appearance data
- Resolved by reducing errors on neutrino energy spectrum and smart choice of energy binning
- Leads to existence of four *CP*-conserving solutions: one per hierarchy and sign θ_{13} combination

Linear Terms in Oscillation Probability

- Linear terms are interferences terms between two mass scales and are first order in θ_{13}
- Most visible at large baselines L and low energies E
- Leads to enhanced MSW matter effects in long baseline appearance data
- Leads to correlations between linear θ_{13} and θ_{23} effects

- Leads to sensitivity of earth-crossing (very long baseline), low energy data to mass hierarchy

Symmetry of the Oscillation Probability

- Sign-symmetry exists in electron neutrino appearance oscillation probability under simultaneous interchange of hierarchy and sign θ_{13}
- Long baseline appearance data is sensitive to pattern of symmetry breaking

More importantly this older body of work showed real evidence of the utility of this new bounds paradigm that we have previously implemented because it makes answering the hierarchy question and determining the sign of θ_{13} dependent questions in the *CP*-conserving three-neutrino framework.[10] Therefore, we continue our project of examining the world's data using these alternative bounds. Having modeled some of the physics, explored the impact, and done an early analysis of older neutrino oscillation data we now re-analyze newer, more relevant data with reduced errors, increased neutrino counts, and at new baselines and energies designed to be more sensitive to θ_{13}, θ_{23}, Δm^2_{32}, and matter effects.

---

[10] Note, using the traditional bounds which do not include negative θ_{13} implies that this makes determining the hierarchy and the *CP*-phase (which now contains negative values) dependent questions.

CHAPTER III

TECHNICAL ANALYSIS OF DATA

In this chapter we present the analysis method implemented to conduct this study:

1. Generated code that reproduced published experimental results.
2. Implemented desired physics in reproduction code.
3. Extracted oscillation properties.
4. Identified physics origins of extracted properties.

For reference, additional technical details are presented in Appendices B and C. We now discuss each of the above aspects of the research in turn.

Generated Code

To conduct our analysis we extended existing FORTRAN legacy code developed by our collaboration. The existing body of code consisted of a set of statistical subroutines, oscillation probability subroutines, and a method for determining experimental features by estimating them from published observations via calibration. The base recipe for generating a code that reproduced published experimental results was to compile all the inputs to the published analysis, select a set of benchmark published data points to match and build the code, adjusting the collection of implemented subroutines and parameter inputs until a desired level of agreement between the code's outputs and the selected benchmark points was achieved. When possible, the most recent published articles were used. Where merited, data presented in pre-prints were sometimes used. Furthermore, when necessary, additional information from dissertations was also included, particularly lengthy oscillation equations and technical details such as errors on the energy per bin.

The selection of benchmark data points from each publication, i.e., the points which the outputs from our developed code had to match in order for a reproduction to be declared completed, was driven by the extent of the data presented in a given publication: the more data and figures provided the more benchmarks were used. The minimum set of benchmarks matched included the best fit mixing parameter values extracted and their 90% C.L. errors. Additional benchmarks points were included for data such as 2-5 points from a chi-squared curve or allowed region (not including the best fit and error values), or sums of predicted number of events.

The base set of code consisted of a set of subroutines designed to apply a (Gaussian or Poisson) chi-squared analysis to extract a set of best fit mixing parameters by comparing the observed number of neutrino signal events to the predicted number of neutrino events under the hypothesis that neutrino oscillations exist and are characterized by an oscillation probability. This part of the analysis is discussed in the next three sections.

Base Code

Predicted Signal

The oscillation probability is calculated as a function of energy for a set of oscillation parameters, $P_{\mu e}\left(E, \theta_{jk}, \Delta m_{jk}^2\right)$. The predicted number of events can be found by calculating the integral of the product of the detection efficiency, number of events for the case of no oscillations, and oscillation probability as functions of energy over the desired energy range [as previously stated, see Eq. (10)]. Our goal was to reproduce published analyses, not construct our own models of each experiment. Therefore, for Poisson statistics, which compares event counts per energy bin, rather than inputting models for each of the terms in Eq. (10) we simply approximated the signal as a product of the oscillation probability and the predicted (theory) number of no oscillation events per energy bin,

$$S_{signal}^{theory} \cong N_{no\ osc}^{MC} \times P_{\nu_\alpha \rightarrow \nu_\beta}^{theory} \tag{58}$$

Using the Monte Carlo (MC) no oscillation prediction per energy bin in the far detector served as a calibration factor that could be multiplied by the oscillation probability per energy bin and then tuned using one or several constants designed to adjust overall norms for various elements of the calculation. The use of the published no oscillation prediction given by the Monte Carlo, which takes into account aspects of the physics such as the interaction cross-sections, near-to-far detector systematic errors, and the near-to-far event spectrum ratios, allowed us to include this technical information without specifying its form. The result of numerically calculating Eq. (11) is the total number of signal neutrino events resulting from oscillations for a given energy bin and given set of parameters. For Gaussian (normal) statistics the scenario is significantly simplified as the oscillation probability itself can be directly compared to the data, so no calculation of signal events is needed, only the oscillation probability needs to be calculated.

Fitted Data

The next step in the analysis was to determine the best fit values. The standard statistical approach to finding a best fit value for neutrino oscillation mixing parameters is known as a contour-based unified analysis, or, the Feldman-Cousins approach [66]. This method was designed to treat time-independent, discrete counting data with symmetric errors such as the observation of a small number of particle events with large background and systematic experimental errors. In the Feldman-Cousins prescription, the best fit value of the mixing angle is obtained by minimizing a chi-squared test statistic that varies with the fit parameter(s) of interest, here $\chi^2(\vec{\boldsymbol{y}})$. The chi-squared value is a measure of the goodness-of-fit between the data and the theoretical prediction, which depends on a set of mixing parameters $\vec{\boldsymbol{y}}$.

For Poisson statistics, the simplest chi-squared is calculated via [67]

$$\chi^2(\vec{\boldsymbol{y}}) = 2\left[s(\vec{\boldsymbol{y}}) + b - n + n\ln\left(\frac{n}{s(\vec{\boldsymbol{y}}) + b}\right)\right] \tag{59}$$

where $s(\vec{\boldsymbol{y}})$ is the total number of predicted signal events found from Eq. (10), b is the total number of observed background events, and n is the total number of observed signal events. The best fit value of $\vec{\boldsymbol{y}}$ occurs when chi-squared is a minimum. Therefore, the best fit value of $\vec{\boldsymbol{y}}$ can be calculated by numerically sampling the chi-squared values over a range of $\vec{\boldsymbol{y}}$ to find the minimum, $\chi^2_{min}(\vec{\boldsymbol{y}}^{\,best})$.

Systematic errors are incorporated into the chi-squared calculation by including nuisance fit parameters and adding systematic error terms,

$$\chi^2(\vec{\boldsymbol{y}}) = 2\left[\kappa s(\vec{\boldsymbol{y}}) + \beta b - n + n\ln\left(\frac{n}{\kappa s(\vec{\boldsymbol{y}}) + \beta b}\right)\right] + \left(\frac{\beta - 1}{\sigma_b}\right)^2 + \left(\frac{\kappa - 1}{\sigma_s}\right)^2 \qquad (60)$$

where κ is a fitted normalization on the predicted number of signal events, β is a fitted increase or reduction in the observed background, σ_b is the error on the background, and σ_s is the error on the signal normalization. The systematic errors are treated as nuisance parameters and first fitted at each sampling of $\vec{\boldsymbol{y}}$ using a numerical SIMPLEX[11] algorithm in FORTRAN before minimizing $\chi^2(\vec{\boldsymbol{y}})$. SIMPLEX assigns values to the nuisance parameters by searching for the minimum chi-squared over a two-dimensional grid of the nuisance parameter space at a fixed value of the mixing parameters. After each cycle of the SIMPLEX subroutine, the search grid is made smaller based on the results of the previous cycle until the variance in the chi-squared converges to the desired level of precision, i.e., until changing the nuisance values further has little effect on the chi-squared. For the present analysis, the convergence cut-off was a variance of 10^{-5} between successive values of $\chi^2(\vec{\boldsymbol{y}})$. The final fitted nuisance parameters at each value of $\vec{\boldsymbol{y}}$ are then included into the full minimization over $\vec{\boldsymbol{y}}$ by re-calculating the chi-squared at each sampling.

For Gaussian statistics the oscillation probability $P(E)$ is equivalent to the ratio $R(E)$ of the observed to predicted number of events as a function of neutrino energy. Therefore, the χ^2 can be written in the form,

$$\chi^2(\vec{\boldsymbol{y}}) = \sum_{i=1}^{N}\left(\frac{R_i(E) - P^i(E)}{\sigma}\right)^2 \qquad (61)$$

where σ is an overall statistical and systematic error[12] and i is the ith neutrino energy bin.

---

[11] Based on *Numerical Recipes* [68].

[12] Alternatively, the bin errors could be used, σ_i.

Determined Bounds

To obtain an upper bound on a parameter a $\Delta\chi^2$contour is first constructed. This contour plots the relative difference over the sampling range between the chi-squared at each value of the fit parameters and the minimum chi-squared at the best fit. For the present case, the $\Delta\chi^2$ is given by

$$\Delta\chi_i^2 = \chi_i^2(\vec{\boldsymbol{y}}) - \chi_{min}^2(\vec{\boldsymbol{y}}^{\,best}) \tag{62}$$

where $\Delta\chi_i^2$ is the chi-squared difference for the i^{th} value of $\vec{\boldsymbol{y}}$ in the sampling range. A plot of all of the $\Delta\chi_i^2$ values as a function of the fit parameters forms the contour, whose absolute minimum $\Delta\chi_{min}^2$ will always be at zero since the minimum is fitted to the data. For a one parameter fit the contour will be a curve, for a two-parameter fit an (open or closed) region.

There are two uses for a $\Delta\chi^2$ contour plot. The first use is to extract the upper bound and allowed values of the fit parameter at a given confidence level. This can be achieved by simultaneously plotting the data-derived contour and the horizontal line $\Delta\chi_{\mathrm{CL}}^2$. Values of $\Delta\chi_{\mathrm{CL}}^2$ for different confidence levels are obtained from statistical tables and are based on the number of parameters fitted in the chi-squared equation. The upper bound is then given by the fit parameter value at the intersection of the $\Delta\chi^2$ curve and the $\Delta\chi_{\mathrm{CL}}^2$ line and the allowed values are all those for which $\Delta\chi_i^2 < \Delta\chi_{\mathrm{CL}}^2$.

The second use of the $\Delta\chi^2$ contour is to infer values preferred by the data. In the case of neutrino oscillations, both one-parameter ranges and two-parameter regions are plotted. One-parameter contours for $\vec{\boldsymbol{y}}$ are usually upward parabolic and centered around the best fit $\vec{y}$ obtained from analysis. If the contour is skewed to the left, it indicates a preference for a smaller and/or negative value of $\vec{y}$, depending on the values in the sampling range. Conversely, skew to the right indicates that the data prefers larger and/or positive values of $\vec{y}$. Hence, the shape of the $\Delta\chi^2$ curve can reveal information about the range of fit parameter values preferred by a data set, e.g., small or large, positive or negative. Additionally, the width of the chi-squared curve, especially at a confidence level line, indicates how strongly the preferred values are constrained by a particular data set: the narrower the width of the curve the more strongly constrained the values, the wider the width of the curve, the less constrained.

For a two-parameter search the allowed region is most often roughly elliptical. The location of the minimum within the region is indicative of preferred values: an off-center minimum indicates a preference or “tendency toward” a particular subset of the allowed region, while a central minimum indicates no particular preference. The smaller the region’s area the more constrained the value, the larger the less constrained. Additionally, the tilt of the ellipse indicates the strength and nature of correlations between the two parameters: a strong tilt indicates a non-negligible correlation while no tilt indicates a negligible correlation.

Code Tuning

The above gives the general recipe applied for conducting the research. During the code generation phase significant effort went into developing the reproduction codes, which varied greatly between experiments, experiment types, and updated data releases of the same experiment. In the next sections we detail the modifications, or “tuning,” to the base code set to successfully generate reproduction codes that reproduce published results. The majority of these code modifications were designed to address one of two needs: (1) matching the particular set of benchmarks for a given experiment, and/or (2) determining the best way to include the dominant systematic error in a given code.

In all cases the tuning amounted to adjusting one of three features of the results curve or region to match the publication: (1) fitting the location of the minimum, (2) fitting the width of the allowed curve or region, and/or (3) fitting the location of the allowed curve or region in the one- or two-dimensional parameter space.

Signal Calibration

Signal calibration included various multiplicative constants added to aspects of the calculation and used to set the location of the minimum and/or the allowed region, i.e., to shift the minimum, curve, and/or region up or down and/or left or right by increasing or decreasing the multiplicative constant. In cases where no Monte Carlo no oscillation prediction was supplied an alternative method for calibrating the reproduction code was used by extracting the energy- and bin-dependent factors that the experimentalist multiplied by the oscillation probability using the best fit curves provided in publications,

$$r_{calib}^{bin} \cong \frac{S_{best\,fit}^{bin}}{P_{\nu_\alpha \to \nu_\beta}^{bin}} \tag{63}$$

where r_{calib}^{bin} is the derived calibration norm per energy bin, $S_{best\,fit}^{bin}$ is the published best fit number of signal events per energy bin, and $P_{\nu_\alpha \to \nu_\beta}^{bin}$ is the oscillation probability used by the experimental collaboration . This calibration factor could then be multiplied by a new oscillation probability, P_{theory}, to generate a predicted signal. This method captured the order of magnitude bin dependence of experimental factors not clearly listed in publications or beyond the scope of the codes applied here, for example the particular details of the detection efficiencies per bin. It should be noted that this method and subroutine were applicable because many experimental errors were largely energy-dependent and mostly uncorrelated between energy bins.

In some cases an additional shift on the energy was needed in order to set the best fit minimum in the required location. This was done through a simple multiplicative factor r_{flux}, which was an overall multiplicative norm and not bin-dependent,

$$\tilde{S}^{theory}_{renormed} \cong r_{flux} \times S^{theory}_{unormed} \tag{64}$$

where the result of Eq. (64) could then simply be substituted into the relevant equations needing the theoretically predicted number of signal events. In other cases a shift in the overall energy scale (again, bin-independent) was needed to set the minimum, which was similarly done via r_{Escale}

$$\tilde{E}_{renormed} \cong r_{Escale} \times E_{unormed} \tag{65}$$

Furthermore, it was often possible to help set the minimum by dropping the lowest energy bins (provided they contained no events) because the minimum was often "inferred" from the data by the slope of the line between the first big oscillation maximum and the lower energy nearest minimum, rather than by the location of the first big oscillation peak itself. Therefore, dropping bins could adjust the slope of the line and thereby the fit the minimum.

Nuisance Handling

The use of the minimization subroutine included errors on the experimental nuisance parameters, namely the norms on the flux σ_S (signal), background σ_b (when included), and energy scale σ_E. Each of these errors could be used to tune the width of the allowed curve or region: increasing these errors increased the width, decreasing them decreased the width of the resulting curve and/or region. In the case of the energy, published data is presented in histogram fashion, arbitrarily divided into strict energy bins. However, this is not representative of the true errors in the energy resolution of a given experiment. For experiments where the energy resolution is significant, i.e., on the order of a few percent of the energy bin width or more, the spread in the energy at the edges of the bin should be taken into account. In this work this was done by fitting a Gaussian energy distribution over each bin and averaging the oscillation probability over the normally-distributed energy function. The extent of the effect of the energy resolution on the bin calculations is then partly captured by the width of the Gaussian. The error on this added energy shift was then encompassed via the equation

$$\sigma_E^{bin} = \frac{a}{\sqrt{E_{midpoint}^{bin}}} + d \times E_{midpoint}^{bin} \tag{66}$$

where a and d are both hand-set calibration values in percent determined by trial-and-error.

Implemented Physics

Once the reproduction code was completed and verified then the next step in the analysis was to drop in the desired physics we wished to analyze. In the case of this work this was a minimal change as our two primary goals were to: (1) implement a full, exact, three-flavor matter oscillation probability, and to (2) re-conduct the analysis over a joint positive-negative θ_{13} search space. The oscillation probability was only adjusted for those experiments where the values of the full, exact three-flavor probability in matter differed from the equation implied by the reference publication. For those cases where it did not, as confirmed by numerical calculation and comparison of the decimal level difference, the original probability used in the reproduction was retained. In those cases where it did differ by an unacceptable level a legacy code was used to calculate the full, exact, *CP*-conserving three-flavor oscillation probability for a constant density (one- or two-layer) matter profile. The subroutine adapts the algebraic formalism of Ohlsson and Snellman [69] and uses direct matrix manipulation to facilitate code run time.

Extracted Properties

The next step was to run the updated code to generate the best fit values and allowed parameter curves or regions for individual experiments, sets of data, and the global data set. In order to combine data sets a post-processing of the output of each individual data set occurred in order to take into account the errors on fixed mixing parameters via an external marginalization program. For combined data sets, after marginalization, best fit parameters and parameters bounds could then be estimated.

Unlike the bounds determination method discussed above, an additional post-processing code was used to determine the bounds on the extracted parameters. This additional code was implemented to account for the fact that the bounds determination method defined above is intended for use with Gaussian statistics, i.e., analyses that produced symmetric results curves, whereas a number of experiments we analyzed produced distinctly asymmetric final curves. Therefore, we developed a small code to calculate the error bars for the asymmetric case. The tables of numerical results, allowed parameter range curves, and allowed parameter regions generated as a result of this phase of the code implementation cycle constitute the primary research products generated by this work.

Combined Data

To investigate the implications of the world's data for neutrino mixing properties individual experimental data sets were combined in various groupings and as a whole.

Sum Test

The simple statistical sum test provides a time-efficient method of synthesizing the world's data into one global data set over which best fit and upper bound values may be obtained using the same statistical methods applied to individual experimental data sets [70]. The sum test permits any number of data sets to be combined into one data set by adding the $\chi^2(\vec{\boldsymbol{y}})$ values for each individual data set i at every sampling over the parameter space of $\vec{\boldsymbol{y}}$ across a set of N data sets, i.e.,

$$\chi^2_{global} = \sum_{i=1}^{N} \chi^2_i(\vec{y}) \qquad (67)$$

where i labels the separate experimental data sets.

This method is computationally simple and intuitive; since the χ^2 test statistic is, by construction, always positive-valued, the minimum sum over a set of χ^2's (i.e., χ^2_{global}) is obtained when each $\chi^2_i(\vec{y})$ in the set is individually minimized. The relative effect of each individual $\chi^2_i(\vec{y})$ on χ^2_{global} is determined by the relative size of the χ^2 values. Given that these χ^2's include systematic errors in their calculation, the sum over a set of experimental χ^2's automatically takes into account the relative weighting that each individual data set should have in the global set based on the relative statistical strength of each experiment. Furthermore, once $\chi^2_{global}(\vec{y})$ is calculated, the best fit and upper bound values for $\vec{y}$ are obtained using the same analysis method as for an individual experiment.

Marginalization

In order to eliminate parameters not under immediate study, while still accounting for the error in their known values, a standard marginalization technique of integrating the likelihood function over the parameters not being examined was used. In the present case, these nuisance parameters were other mixing parameters not being examined. Marginalizing calculates the integral average of the statistical measure over the allowed range of the parameter to be marginalized away, thereby providing an independent extraction of the parameter of interest [71].

Estimated Errors

To estimate errors for the final asymmetric allowed curves and regions we developed a simple recipe [72] to integrate over the allowed parameter range values to determine the points on the curve at which a certain percentage of the total solution space was covered, i.e., to determine the percent confidence levels from the shape of the curve. This was used to find errors for the final results, rather than using Gaussian error table values and looking for the line crossings between the chi-squared curves and the allowed parameter range curves at set values, such as $\Delta\chi^2 = 2.71$ for a one parameter analysis at the 90% confidence level, which was the method used to match reproduction codes.[13] Using our error estimation method the total area under the curve is determined by the allowed bounds on the parameter under investigation. The confidence level bounds are then the points at which at a certain percentage of the allowed solution space is contained within the area under the curve where the line between the two bounds intersects the chi-squared function, which need not necessarily define a horizontal line. The need for such an error calculation was particularly evinced by the asymmetric shape of the θ_{13} chi-squared curves for the reactor data.

Identified Origins

The final phase of the research was, in light of the numeric results generated in the previous phase, to re-examine aspects of the data in order to determine the factors,

---

[13] This is the method most often used by others in published work.

either the physics or the experimental or statistical features, which drove the results. Unlike the previous phases this phase followed no algorithm or recipe but was devised on a case-by-case basis using insight and trial-and-error. The primary way to seek drivers of numerical results was to devise a hypothesis based on insight then qualitatively test the likelihood that it was a causal driver of a particular result by intentionally tuning the data. In other words, data was intentionally skewed to assess whether or not perceived relationships between certain drivers and certain outcomes appeared to be true. It should be understood that the majority of this work produced qualitative rather than quantitative understanding. However, two quantitative assessments were also used as a result: (1) determination of the relative probabilities that a particular set of properties, from among a finite set of options, was likely to represent the true solution, and (2) a graphical presentation of the relative contribution of each individual experiment to the global result. These two quantitative assessments and the insights into the drivers of the outcomes constitute the primary contribution of this work to this area of research.

CHAPTER IV

FINDINGS

In this chapter we present and discuss our findings regarding the mixing angles θ_{13} and θ_{23}, the mass splitting Δm^2_{32}, and the neutrino mass hierarchy. In particular, we are interested in the significance of the symmetry paradigm in the results obtained. We utilize the following data sets in the analysis: Daya Bay reactor data [10], RENO reactor data [11], MINOS muon neutrino long baseline appearance [41] and disappearance data [73], MINOS anti-neutrino data [74], and T2K muon neutrino long baseline appearance [75] and disappearance data [76].

We also include atmospheric Super-K data [78]. This data contains many of the small effects in which we are interested. However, there is little agreement on the implications of these effects. Rather than discuss their implications, we incorporate the data by only including their effects on constraining the bounds of θ_{23} and Δm^2_{32}. We do this by using a Gaussian likelihood function with the width of the Gaussian taken from the Particle Data Group [78]. This approach differs from our previous preliminary results [53]. There we used the results from our own model of Super-K atmospheric data [63]. This result contained a strong preference for negative θ_{13}, something different from other's results (which also do not agree among each other). Until there is some level of agreement in the field, we will bypass this debate by including the implications of the atmospheric Super-K data that are generally accepted as described above. This is the reason why, as we shall see, our present results no longer show a strong preference for negative θ_{13}.

Mixing Angle θ_{13}

First we discuss the one-parameter implications of a three-parameter analysis for the neutrino mixing angle θ_{13}, see Figure 10. The mixing angle θ_{12} and Δm^2_{21} have been fixed, while θ_{23} and Δm^2_{32} have been marginalized out, and δ_{CP} was set to 0 rads. We find the normal hierarchy, positive θ_{13} provides the best fit to the data. Notice that the broken symmetry is evident in this result. The symmetry pair of normal hierarchy-positive θ_{13} (blue solid) and its partner inverse hierarchy-negative θ_{13} (green dash) lie the lowest and, hence, are the most likely while the other symmetry pair normal hierarchy-negative θ_{13} (orange dot-dash) and its symmetry partner inverse hierarchy-positive θ_{13} (red dot) lie the highest. This preference occurs at roughly the 90% C.L. level ($\Delta\chi^2 = 2.71$). Also, θ_{13} is well constrained by the data, which can be seen from the steepness of the $\Delta\chi^2$ curve in Figure 10 with a clear valley around the minimum near $\theta_{13} \sim 0.16$ rads. While the existence of four distinct solutions matches our previous findings, the preference for $\{\text{NH}, +\theta_{13}\}$ is new to this work.

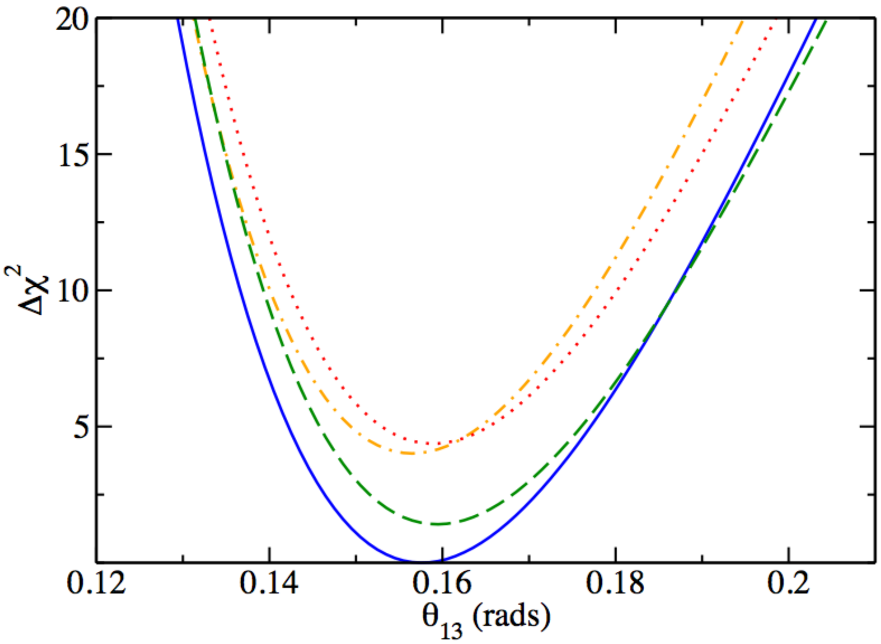

Figure 10. Final result for the mixing parameter θ_{13}. The curves are as follows: blue solid is NH and positive θ_{13}; green dash is IH and negative θ_{13}; orange dot-dash is NH and negative θ_{13}; and red dot is IH and positive θ_{13}.

We find this result for θ_{13} is mostly driven by the Daya Bay experiment, as illustrated by Figure 11. Daya Bay has a well-defined minimum and stringent bounds on θ_{13} while RENO contributes little to the bounds and prefers a slightly larger value of θ_{13}. In a joint reactor analysis, Daya Bay (blue dash curve) clearly dominates RENO (red dot-dash curve) when combined (black solid curve). This result is expected, since Daya Bay has much higher statistics and much smaller errors than RENO. The best fit values for θ_{13} with errors are presented for each of the four cases in the Table 16.

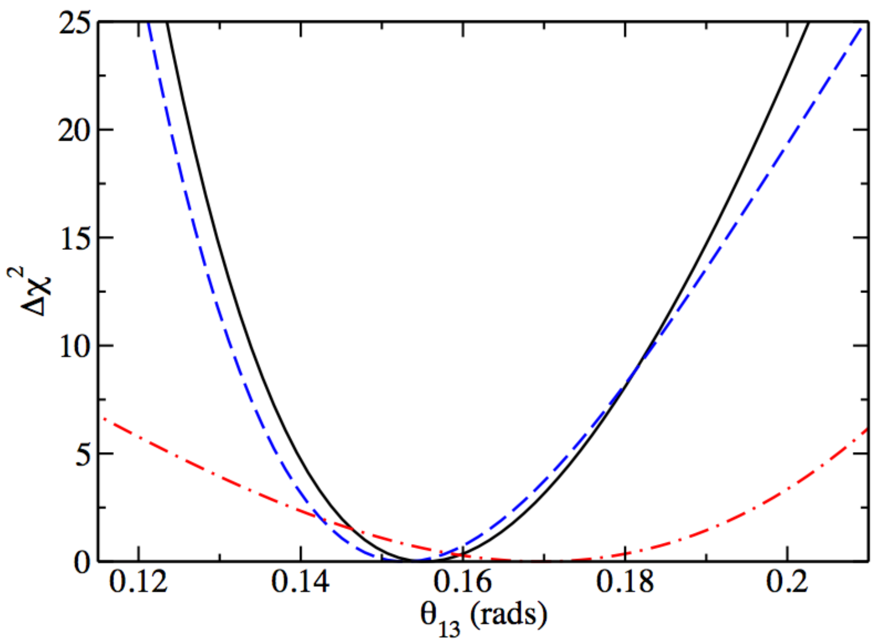

Figure 11. Contribution of experiments to the final result for θ_{13}. The curves are as follows: blue dash is Daya Bay; red dot-dash is RENO; and black solid is both experiments combined.

Mixing Angle θ_{23}

Next we discuss the one-parameter implications of a three-parameter analysis for the neutrino mixing angle θ_{23}. The mixing angle θ_{12} and Δm^2_{21} have been fixed, while θ_{13} and Δm^2_{32} have been marginalized out, and δ_{CP} was set to 0 rads. It is most informative to discuss our investigation of θ_{23} in two steps: first examining the result with the long baseline appearance data excluded, then discussing the results with the long baseline appearance data included. In the previous section we found the mixing angle θ_{13} was mostly determined by the Daya Bay reactor experiment, i.e., the final result for θ_{13} was very close to the result of Daya Bay by itself while the remaining experiments had very little impact.

On the other hand, as we shall see, the two parameters θ_{23} and Δm^2_{32} are determined from a combination of experiments and their distinctive interplay. The MINOS and T2K long baseline muon neutrino disappearance experiments, Super-K atmospheric experiment treated as described above, and the MINOS antineutrino disappearance experiment serve mainly to determine θ_{23} and Δm^2_{32}. Once these two parameters have been determined, due to the presence of the symmetry, there exist four distinct solutions or predictions. To a reasonable approximation, the T2K and MINOS experiments then determine the hierarchy and the sign of θ_{13} via their agreement or disagreement with each of the four predictions.

We present our results in Figure 12 for the parameter θ_{23} and the analysis that contains all of the relevant experiments except the long baseline appearance T2K and MINOS. The first noticeable feature is that there exists a double minimum with the curves approximately symmetric about the maximal mixing angle of $\pi/4$. The double minimum arises because of a broken symmetry about the maximal mixing value. This has not been previously observed, most likely because the MINOS collaboration and others use approximate oscillation probabilities whose leading terms in $\sin^2 2\theta_{23}$ are exactly symmetric about $\pi/4$. A manuscript that investigates this phenomenon is in preparation.

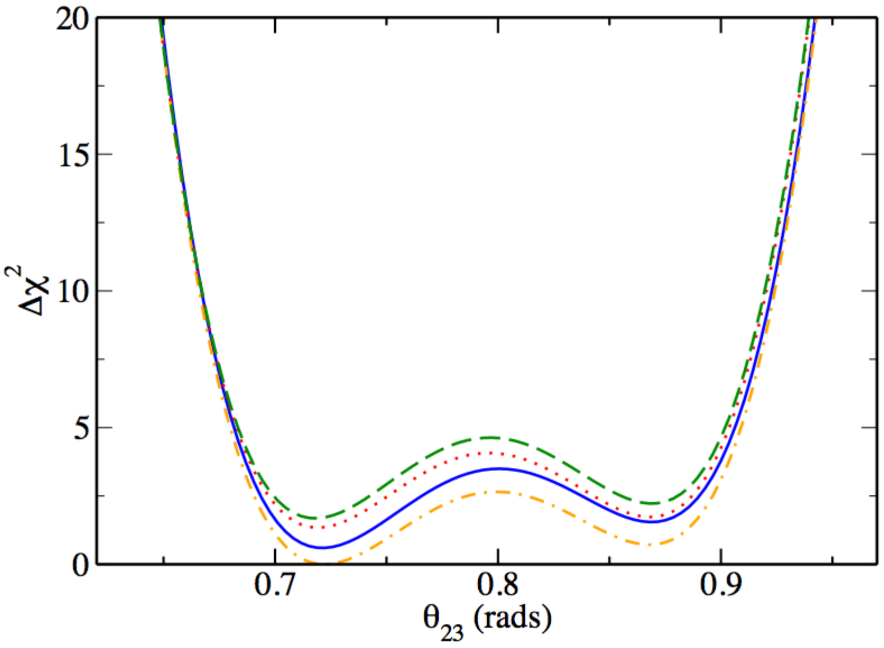

Figure 12. Intermediate result for the mixing parameter θ_{23}. The curves are as follows: blue solid is NH and positive θ_{13}; green dash is IH and negative θ_{13}; orange dot-dash is NH and negative θ_{13}; and red dot is IH and positive θ_{13}. Curves exclude the T2K and MINOS appearance data.

The second new phenomenon in the curves is that the results are both hierarchy and sign of θ_{13} sensitive. In the most recent T2K manuscript [77] the hierarchy dependence was first observed. As they examined only positive θ_{13} solutions (as is customary), they could not have recognized the sign of θ_{13} dependence. One can conjecture the existence of a pure hierarchy broken symmetry as the two normal hierarchy curves lie below the two inverse hierarchy curves.

In Figure 13 we present the total analysis for the parameter θ_{23}. Although the $\Delta\chi^2$ between the four cases is significant, $\Delta\chi^2 \sim 5$, it is difficult to extract clean information because of the double minimum structure of the $\Delta\chi^2$ curve. Notice the ordering of the curves and the relative spacing between the curves is consistent between the θ_{13} results, Figure 10, and the θ_{23} results, Figure 13.

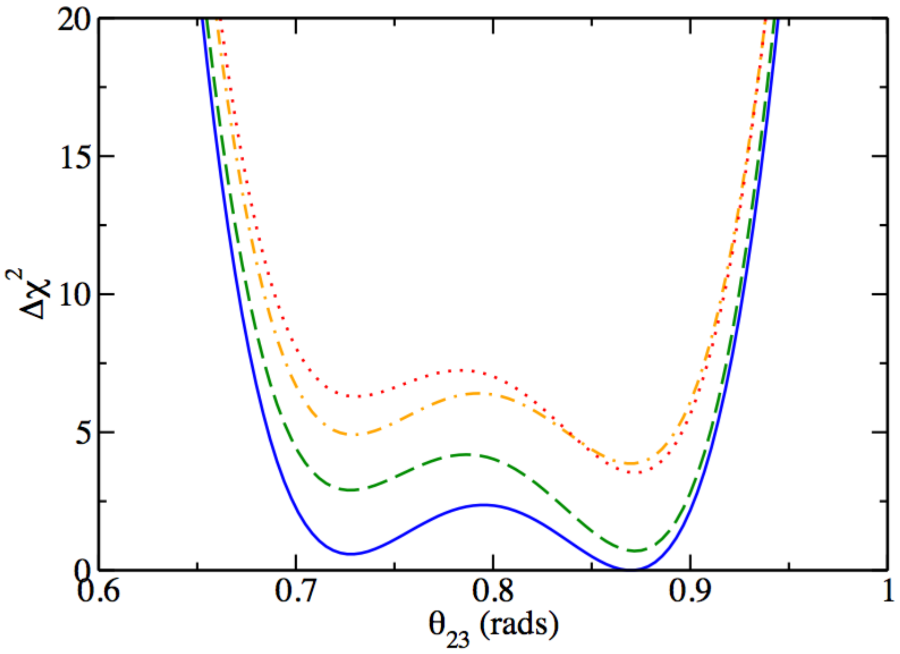

Figure 13. Final result for the mixing parameter θ_{23}. The curves are as follows: blue solid is NH and positive θ_{13}; green dash is IH and negative θ_{13}; orange dot-dash is NH and negative θ_{13}; and red dot is IH and positive θ_{13}.

It is important to note that the broken symmetry is evident in the final result. The symmetry pair normal hierarchy-positive θ_{13} and inverse hierarchy-negative θ_{13} lie lowest while the other symmetry pair, normal hierarchy-negative θ_{13} and inverse hierarchy-positive θ_{13}, form a pair at higher $\Delta\chi^2$. This preference occurs at roughly the 90% C.L. level. Again we find the normal hierarchy, positive θ_{13} provides the best fit to the data. The presence of a global minimum near $\theta_{23} \sim 0.86$ rads (second octant) is clear in Figure 13, as is the existence of a local minimum at $\theta_{23} \sim 0.73$ rads (first octant). Furthermore, the relative locations of the global and local minima are the same for all four solutions.

While the existence of four distinct solutions matches our previous findings, the preference for {NH, +θ_{13}} when extracting θ_{23} is new to this work. Also, unlike our most recent previous work with θ_{23} [53], this work shows a clear, though statistically insignificant, global minimum rather than a symmetric set of double global minima.

The addition of the long baseline T2K and MINOS appearance experiments provides significant sensitivity to the hierarchy and sign of θ_{13}, as can be seen by the increase in the separation between the individual curves from Figure 12 to Figure 13. The oscillation probability $P_{\mu e}$ measured by these experiments has leading order terms that distinguish between hierarchies and sign θ_{13} so that this sensitivity is expected.

The challenge is that quality data is difficult to obtain because the peak of $P_{\mu e}$ at the L/E value being used in T2K and MINOS is only ~ 6%. This leads to limited statistics for finite running time. MINOS was designed to measure $P_{\mu\mu}$ and obtain a value of the mass squared difference Δm^2_{32}. To maximize the incident flux, the detector is located on-axis at the peak of the beam. This gives a significant background when trying to detect the few electron neutrinos being produced. As a result, the background is unfortunately a significant fraction of the signal in the MINOS experiment. To reduce the background, the T2K detector is located off-axis. The background is forward peaked and thus misses the detector. However, the signal is also forward peaked although less so than the background. Hence, the incident flux on the detector is diminished by going off-axis leading to a limited signal. The present data from T2K only observes a total of 28 electron neutrinos.

In Figure 14 we repeat the results of this analysis for the normal hierarchy-negative θ_{13}, the best fit case, together with the contribution of individual experiments to this result. First, looking at the minima we see that the double minimum structure arises from the MINOS neutrino (red dot-dash) and the MINOS antineutrino (maroon dot) disappearance experiments. The T2K disappearance experiment (blue dash) has very shallow minima. The Super-K (violet dot-dash-dash) results have a flat single minimum near maximal mixing.

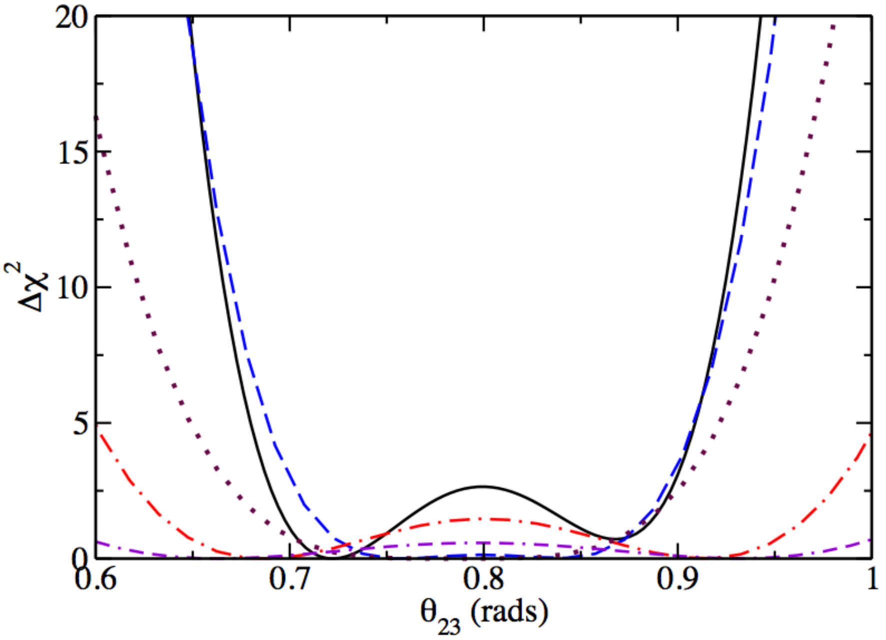

Figure 14. Contribution of experiments to the best fit result {NH, -θ_{13}} for θ_{23}. The curves are as follows: blue dash is T2K disappearance; red dot-dash is MINOS disappearance; violet dot-dash-dash is Super-K; and maroon dot is MINOS antineutrino disappearance; and black solid is all experiments combined.

Second, looking at the bounds we see that the T2K disappearance data (blue dash) dominates the bounds and to a lesser extent the MINOS antineutrino disappearance data (maroon dot). This is a recent finding, in agreement with the trend in the literature that shows that the most stringent constraint previously set by Super-K is being superseded by the most recent T2K data. This result was expected as T2K is gaining statistics at the L/E relevant to the extraction of θ_{23}. Super-K is no longer the leading experiment in determining the value of θ_{23}; the lead is now the two long baseline disappearance experiments.

Lastly, a comparison of Figure 13 and Figure 14 shows that the octant of the global and local minima changes between these two plots. This is due to the fact that the full final result presented in Figure 13 includes the T2K and MINOS neutrino disappearance data while the combined result in Figure 14 (black solid curve) does not. Again this demonstrates that these two data sets play an important role in the extraction of θ_{23}, even though they are not individually sensitive to this mixing parameter. Since they are more sensitive to mass hierarchy effects than the other data sets it is possible that mass hierarchy effects partly help set the octant of θ_{23}. This global result is, therefore, a good example of the often subtle interplay between data sets. The best fit values for θ_{23} with errors are presented for each of the four cases in Table 16.

Atmospheric Mass-Squared Difference

We now turn to discussing the one-parameter implications of a three-parameter analysis for the atmospheric mass-squared difference Δm^2_{32}. The mixing angle θ_{12} and Δm^2_{21} have been fixed, while θ_{13} and θ_{23} have been marginalized out, and δ_{CP} was set to 0 rads. As in our examination of θ_{23}, we proceed in two steps. We begin by examining the results with the T2K+MINOS long baseline appearance data excluded. These results are given in Figure 15. We see that the results are sensitive to hierarchy and sign θ_{13} as were the θ_{23} results. The sensitivity to hierarchy was pointed out in Ref. [77], while the sensitivity to the sign of θ_{13} is new. The ordering of each case and the relative magnitude of the splittings are similar to those found for θ_{23}.

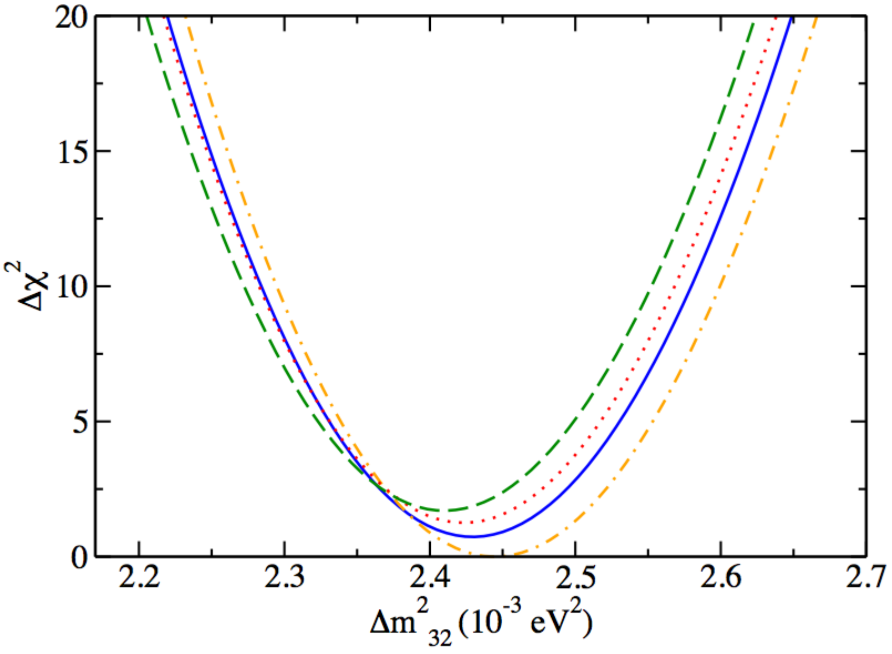

Figure 15. Intermediate result for the atmospheric mass splitting. The curves are as follows: blue solid is NH and positive θ_{13}; green dash is IH and negative θ_{13}; orange dot-dash is NH and negative θ_{13}; and red dot is IH and positive θ_{13}.

Yet again, as our final result we find that the normal hierarchy, positive θ_{13} provides the best fit to the data and yet again the symmetry pair containing {NH, $+\theta_{13}$} is preferred, as demonstrated by the relative locations of the blue-green (solid, dash) and red-orange (dot, dot-dash) curves, see Figure 16. This preference occurs at roughly the

90% C.L. level. This shows good agreement between the three analyses (θ_{13}, θ_{23}, and Δm^2_{32}) as to the preferred solution. Also, Δm^2_{32} is well constrained by the data, which can be seen from the steepness of the $\Delta\chi^2$ curve in Figure 16 with a clear valley around the minimum near $\Delta m^2_{32} \sim 2.43 \times 10^{-3}$ eV^2. While the existence of four distinct solutions matches our previous findings, as already mentioned, the preference for {NH, +θ_{13}} is new to this work. The best fit values for Δm^2_{32} with errors are presented in Table 16.

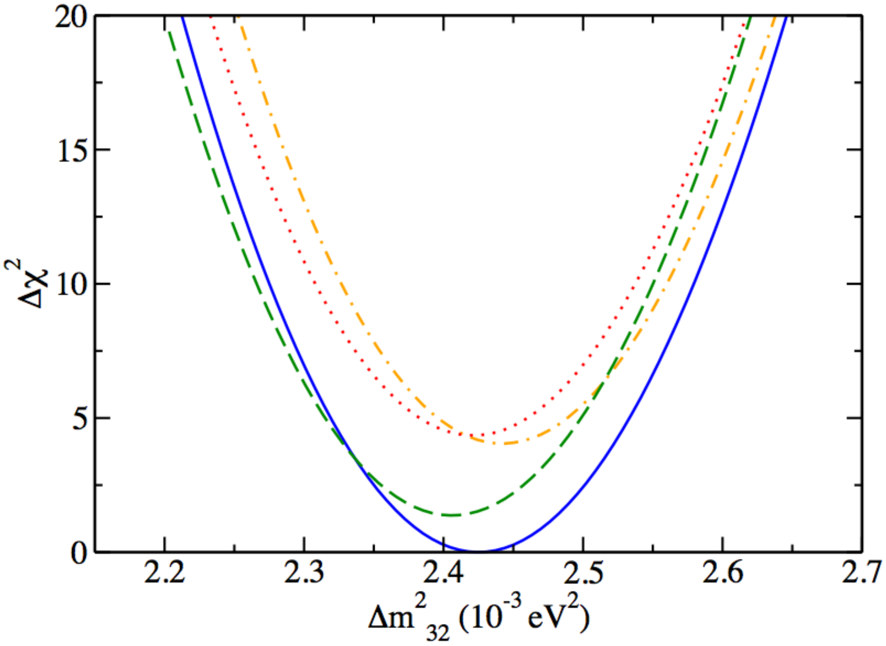

Figure 16. Final result for the atmospheric mass splitting. The curves are as follows: blue solid is NH and positive θ_{13}; green dash is IH and negative θ_{13}; orange dot-dash is NH and negative θ_{13}; and red dot is IH and positive θ_{13}.

The contribution of individual experiments to these results is pictured in Figure 17. The final result is an interesting consequence of a combination of T2K (blue dash) and MINOS (red dot-dash) disappearance with Daya Bay [10] (green dot-dot-dash) playing a significant role. There is tension between these three experiments as can be seen by the location of each minimum, MINOS at 2.32×10^{-3} eV^2, T2K at 2.56×10^{-3} eV^2, and Daya Bay at 2.53×10^{-3} eV^2. The results of the Super-K atmospheric and the MINOS antineutrino data are negligible.

The breakdown of contributions to the global final result for Δm^2_{32} is not as clear as it was for the case of θ_{13} and θ_{23}. At first glance, the set of experiments included here may not seem to be in good agreement, as seen by the spread of the locations of the minima of the curves in Figure 17. However, from the scale of the plot it is clear that they are all in decent agreement, but that no single experiment drives the location of the global minimum. Similarly, no single experiment drives the lower or upper bounds of the global result (solid black curve). By implication, the result for Δm^2_{32} is clearly determined by a complex and subtle interplay between all the relevant data sets.

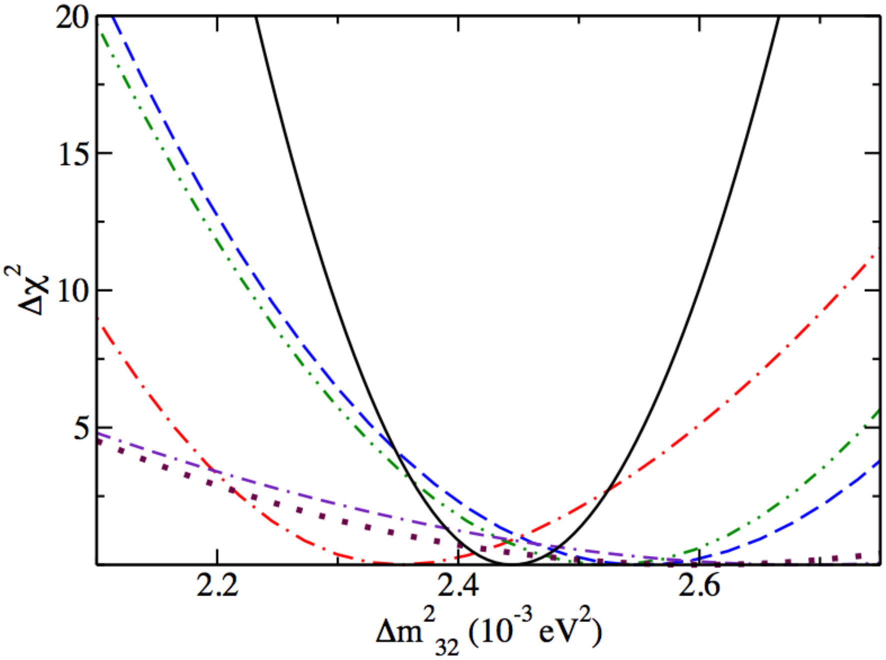

Figure 17. Contribution of experiments to the final result for the atmospheric mass splitting. The curves are as follows: blue dash is T2K disappearance; red dot-dash is MINOS disappearance; green dot-dot-dash is Daya Bay; violet dot-dash-dash is MINOS antineutrino disappearance; maroon dot is Super-K; and black solid is all experiments combined.

Something that is clear in Figure 17 is that combining experiments is a very non-linear process. The individual chi-squareds do not simply add. This is because the addition of a single experiment induces a response where the minima of each parameter and especially the errors on each of the parameters change, usually decreasing. Having reduced errors on the parameter other than the one being examined can lead to a reduced error on the parameter being examined.

Multiple Solutions

As we have stressed repeatedly throughout this work, a large portion of the contribution of this research comes from highlighting that there clearly exist four solutions for the *CP*-conserving case when analyzing neutrino oscillation data in a full three-neutrino framework with matter effects. Secondly, we have pointed out that the data can distinguish between these four solutions. This was clearly seen in the one-parameter analyses for θ_{13}, θ_{23}, and Δm^2_{32}. It can also clearly be seen in the two-parameter implications of a three-parameter analysis between all possible pairs of these three mixing parameters, as illustrated in Figure 18 through Figure 20.

Figure 18 presents the 90% C.L. ($\Delta\chi^2 = 4.61$) allowed region for Δm^2_{32} and θ_{13}. The allowed region is calculated with respect to the local minimum for each of the four solutions. If we were to use $\Delta\chi^2$ defined with respect to the best fit minimum {NH, $+\theta_{13}$} only that minimum would be present. The region is a well-defined ellipse with a gentle tilt, indicating minimal correlations between these two parameters. All four solutions have roughly the same allowed region.

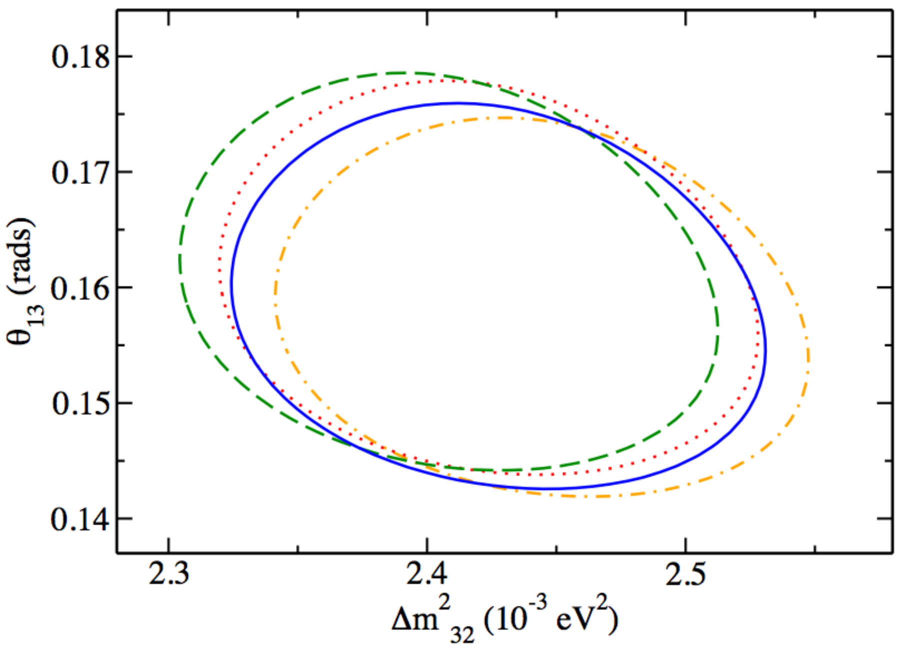

Figure 18. Final 90% C.L. allowed region for the atmospheric mass splitting and θ_{13}. The curves are as follows: blue solid is NH and positive θ_{13}; green dash is IH and negative θ_{13}; orange dot-dash is NH and negative θ_{13}; and red dot is IH and positive θ_{13}.

In Figure 19 we give the 90% C.L. ($\Delta\chi^2 = 4.61$) allowed region for θ_{23} and θ_{13}. The region is a well-defined hourglass. All four solutions have roughly the same allowed region. The preferred case, {NH, + θ_{13}} (blue solid curve) and the case for {NH, - θ_{13}} (orange dot-dash curve) are more symmetric than then other two solutions. This may suggest that some sort of inverse hierarchy effect, perhaps a linear in θ_{13} effect, is at play in the data. The hourglass shape is indicative of the two minima, one local and one global, seen earlier in the one-parameter analysis plot for θ_{23} (see Figure 13). The location of the pinched in portion of the hourglass shape is significant: this occurs near the three-neutrino maximal mixing angle defined in Ref. [79]. This is a unique finding presented here for the first time and not yet, to the best of our knowledge, previously mentioned anywhere in the literature.

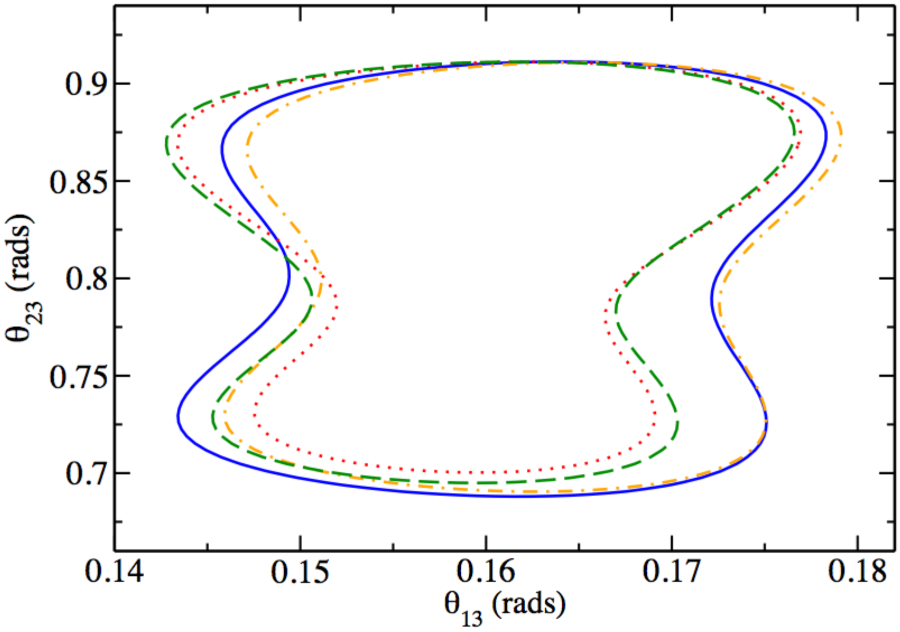

Figure 19. Final 90% C.L. allowed region for θ_{13} and θ_{23}. The curves are as follows: blue solid is NH and positive θ_{13}; green dash is IH and negative θ_{13}; orange dot-dash is NH and negative θ_{13}; and red dot is IH and positive θ_{13}.

The final allowed region for θ_{23} and Δm^2_{32} is shown in Figure 20. Once again there are clearly four solutions (curves) visible and all are roughly the same shape. Also, the double lobe shape of the allowed region is again driven by the double minima in θ_{23}.

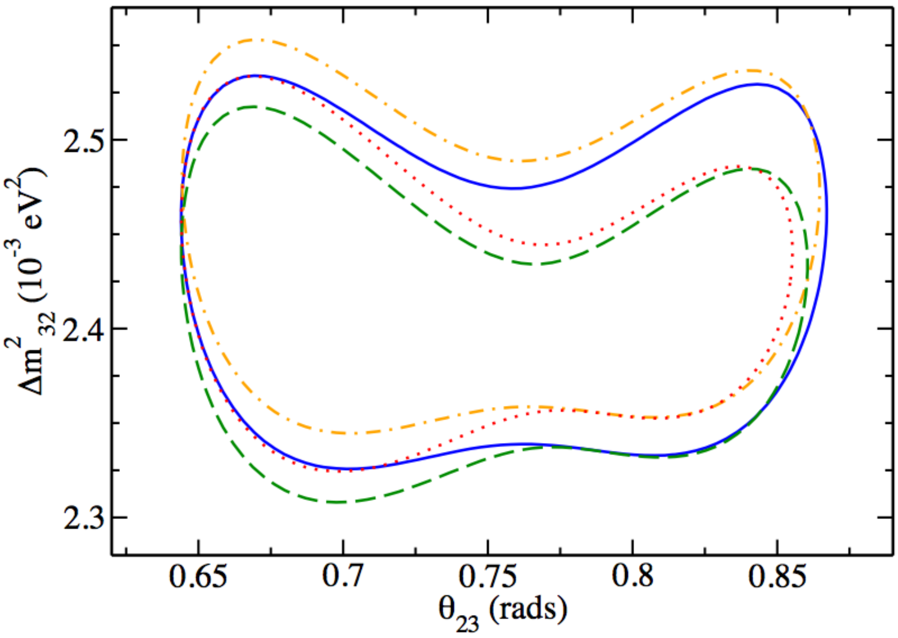

Figure 20. Final 90% C.L. allowed region for θ_{23} and the atmospheric mass splitting. The curves are as follows: blue solid is NH and positive θ_{13}; green dash is IH and negative θ_{13}; orange dot-dash is NH and negative θ_{13}; and red dot is IH and positive θ_{13}.

We also examine the question of the relative importance of the MINOS appearance data with respect to the T2K appearance data when analyzing the data using the symmetry paradigm that contains four solutions, see Figure 21.

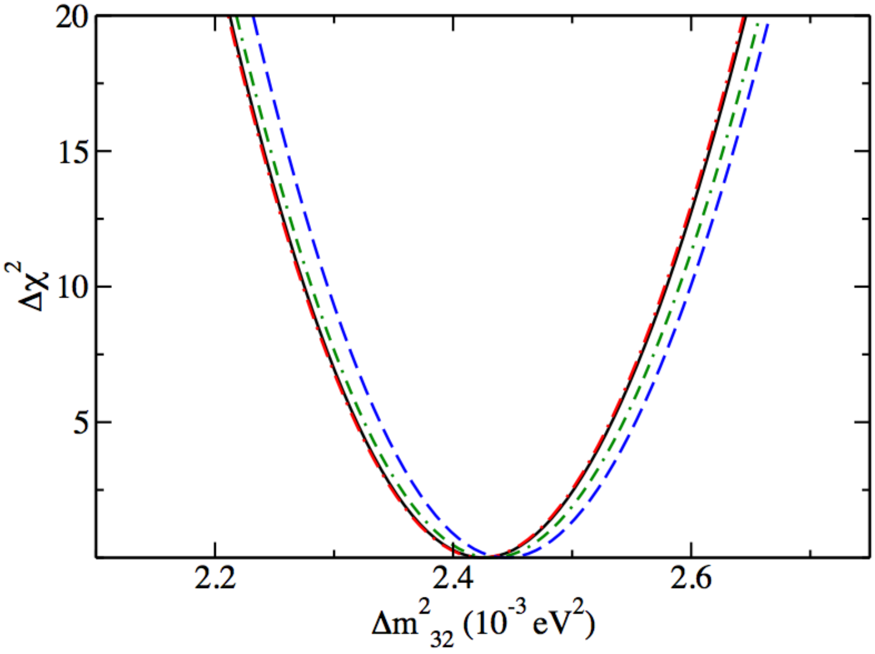

Figure 21. Contribution of appearance data to the {NH, +θ_{13}} final result for the atmospheric mass splitting. The curves are as follows: black solid is all; blue dash is all minus T2K/MINOS appearance; red dot-dash includes T2K; green dot-dash-dash includes MINOS.

The solid black curve is the final result for the full analysis for the parameter Δm^2_{32}. Compare this to the blue dash curve generated by all the experiments except the T2K and MINOS appearance data. We see that the appearance data alters the results, but by a small amount. The green dot-dash-dash curve includes the MINOS data, but not the T2K data. Note that MINOS alone moves the blue dash curve a fraction of the way to the full results. However, the red dot-dash curve, which represents incorporation of T2K and not MINOS, falls nearly on top of the black curve, the full answer. This could be interpreted as T2K being dominant and MINOS being negligible.

In Figure 22 we perform the same investigation for θ_{13}. The long baseline appearance experiments do not alter the value of θ_{13} much, only increasing it from 0.157 rads to 0.158 rads.

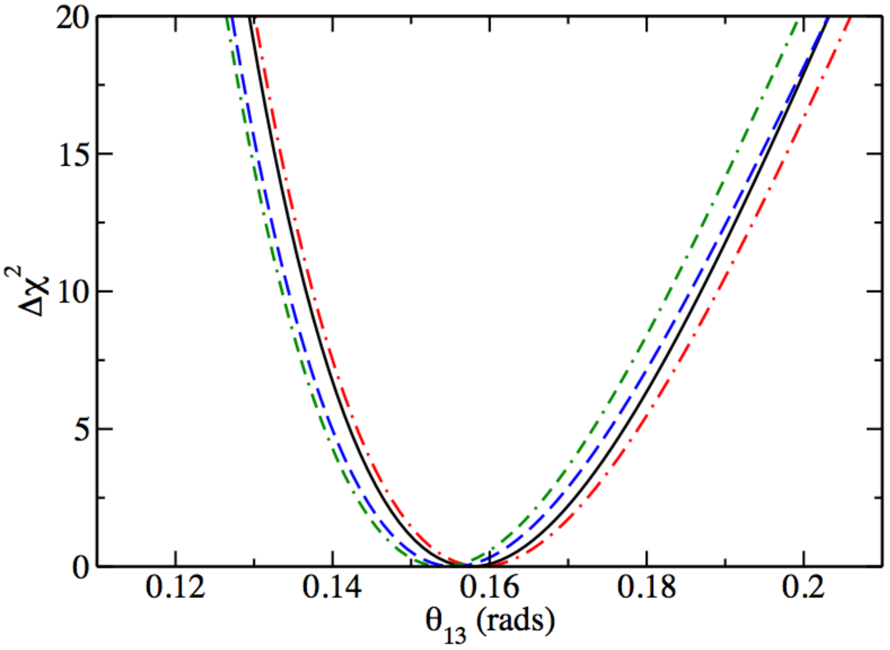

Figure 22. Contribution of appearance data to the {NH, +θ_{13}} final result for θ_{13}. The curves are as follows: black solid is all; blue dash is all minus T2K/MINOS appearance; red dot-dash includes T2K; green dot-dash-dash includes MINOS.

In Figure 23 we show the same curve except it is for the parameter θ_{23}. The mixing angle θ_{23} is the least determined of the mixing parameters and, due to the double minima, the least interpretable of the results. The order of the curves differs at each minima. On the right side, the solid black and red dot-dash are equal, indicating that the inclusion of only T2K reproduces the full results. On the left side you find that the blue dash curve (omitting both T2K and MINOS) is equal to the green dot-dash-dash curve (MINOS only included). If this was a linear system then, as implied by the relative positions of the curves in the right hand side, the full results would match the T2K results only and the inclusion of the MINOS results would be negligible. However, this pattern is not reproduced on the left hand side implying non-linear behavior. The addition of an experiment leads to each of the three parameters responding in its own individual way giving a change that is not at all intuitive.

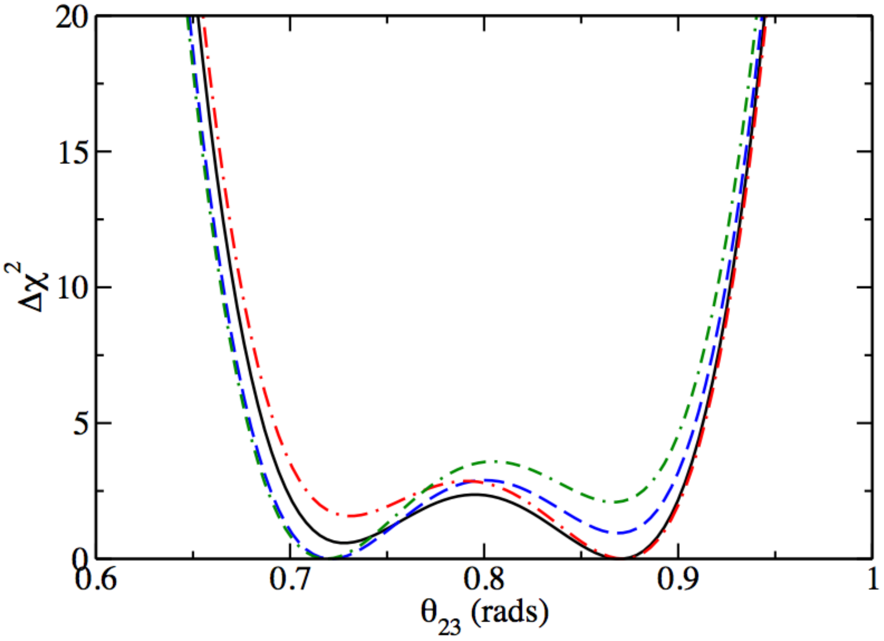

Figure 23. Contribution of appearance data to final {NH, +θ_{13}} result for θ_{23}. The curves are as follows: black solid is all; blue dash is all without T2K/MINOS appearance; red dot-dash includes T2K; green dot-dash-dash includes MINOS.

Summary of Results

We present in Table 15 and Table 16 results of our analysis of the mixing parameters θ_{13}, θ_{23}, and Δm^2_{32} and the value of the minimum χ^2 for each of the four cases of hierarchy and sign θ_{13}. In Table 15 we present results for the intermediate analysis, the analysis in which we omit the T2K and MINOS long baseline experiments. In Table 16 we present the results for the full analysis.

Table 15. Intermediate mixing parameter values (without long baseline appearance data) with 90% C.L. errors and minimum χ^2.

Mass Hierarchy	Sign of θ_{13}	θ_{13} (rads)	θ_{23} (rads)	Δm^2_{32} (10^{-3} eV^2)	χ^2_{min}
Normal	Positive	$0.156^{+0.014}_{-0.012}$	$0.722^{+0.174}_{-0.032}$	$2.43^{+0.08}_{-0.08}$	0.73
Normal	Negative	$0.156^{+0.014}_{-0.012}$	$0.722^{+0.174}_{-0.032}$	$2.44^{+0.08}_{-0.08}$	0.0
Inverse	Positive	$0.156^{+0.014}_{-0.011}$	$0.719^{+0.181}_{-0.032}$	$2.42^{+0.08}_{-0.08}$	1.25
Inverse	Negative	$0.157^{+0.014}_{-0.012}$	$0.719^{+0.181}_{-0.032}$	$2.41^{+0.08}_{-0.08}$	1.70

We see in Table 15 that for the intermediate analysis, the parameters θ_{13} and Δm^2_{32} are well determined and do not have great sensitivity to hierarchy or sign θ_{13}. For θ_{23} the numbers in the Table do not adequately describe the double minimum structure of the χ^2. The minimum that is the lower of the two minima is the absolute minimum. The errors are the distance from the minimum to the value of $\chi^2 = 2.71$. Going to smaller values, this is small. Going to larger values, this goes beyond the other minimum and is large.

Table 16. Final mixing parameter values with 90% C.L. errors and minimum χ^2.

Mass Hierarchy	Sign of θ_{13}	θ_{13} (rads)	θ_{23} (rads)	Δm^2_{32} (10^{-3} eV^2)	χ^2_{min}
Normal	Positive	$0.158^{+0.014}_{-0.012}$	$0.868^{+0.039}_{-0.178}$	$2.42^{+0.08}_{-0.08}$	0
Normal	Negative	$0.157^{+0.014}_{-0.011}$	$0.868^{+0.036}_{-0.167}$	$2.44^{+0.08}_{-0.08}$	4.18
Inverse	Positive	$0.159^{+0.014}_{-0.011}$	$0.872^{+0.032}_{-0.142}$	$2.42^{+0.08}_{-0.08}$	4.48
Inverse	Negative	$0.160^{+0.014}_{-0.012}$	$0.872^{+0.032}_{-0.160}$	$2.40^{+0.08}_{-0.08}$	1.50

In Table 16 we present our final results for the analysis using all the data. We see that the parameters θ_{13} and Δm^2_{32} change very little. The appearance data contributes little to their determination. The difference between the four cases is now much larger than it is for the intermediate analysis. $P_{\mu e}$ is much more sensitive than is $P_{\mu\mu}$ to hierarchy and sign θ_{13} as expected. We also see in the full results the signature of the two-fold symmetry. The two best fit cases, {NH, +θ_{13}} and {IH, -θ_{13}}, are one of the symmetry pairs and the other two solutions, {NH, -θ_{13}} and {IH, +θ_{13}}, the other symmetry pair are nearly degenerate. This pattern indicates that the information in the T2K appearance data (T2K dominates for the appearance channel) is spectral. Further distinction between individual cases within a symmetry pair requires better knowledge of the magnitude of the cross-section.

We also see a distinct change in the value of θ_{23} from its value for the intermediate analysis. Although the numbers in the Tables are quite different, the change is actually small. The appearance data alter two things: the minimum corresponding to the larger value of θ_{23} is now the absolute minimum and the difference between each of the solutions has increased.

Since the parameters θ_{13} and Δm^2_{32} are not changed by appearance data, ignoring θ_{23} for the moment, how do these experiments distinguish between hierarchy and sign θ_{13}? The answer arises from the fact that for a given set of mixing parameters, the oscillation probability $P_{\mu e}$ is different for each of the four cases of hierarchy and sign θ_{13}. The experiments other than the appearance experiments fix the mixing parameters and give four distinct predictions for the appearance experiments. The level of agreement between the data and each of the four experiments then determines the preference for each of the four cases.

In Table 17 we compare our results with the results from three recent global analyses. There is good general agreement. For θ_{23}, we include the location of the two minima if results are given by the authors for a second minima. All but Capozzi *et al.* [80] report a second minimum, but Gonzalez-Garcia *et al*. [27] do not report any distinction between the hierarchy and Forero *et al.* [22] find two solutions only for the normal hierarchy. We include for completeness our results for negative θ_{13} although no one else has provided any information on these two solutions. The T2K collaboration [76] finds a single minima for θ_{23} at 0.90 rads. The only qualitative difference is that we find the absolute minimum to lie above $\pi/4$ while Capozzi *et al*. find the minimum below $\pi/4$ to be lowest.

Table 17. Comparison of our results with three other recent global analyses. Others give only the positive θ_{13} solutions. They, however, do include the *CP*-phase δ_{CP}. The column θ_{23} < (θ_{23} >) represent a solution with θ_{23} less than (greater than) $\pi/4$. NH: normal hierarchy; IH: inverse hierarchy.

	Δm^2_{32} (10^{-3} eV^2)		θ_{13} (rads)		θ_{23} < (rads)		θ_{23} > (rads)	
	NH	IH	NH	IH	NH	IH	NH	IH
Gonzalez-Garcia [27]	2.47	2.43	0.151	0.151	0.698	--	0.880	--
Forero [22]	2.55	2.43	0.157	0.159	0.712	--	0.899	0.886
Capozzi [80]	2.43	2.38	0.153	0.156	0.722	0.740	--	--
This work (+θ_{13})	2.42	2.42	0.158	0.159	0.726	0.730	0.868	0.872
This work (-θ_{13})	2.44	2.40	0.157	0.160	0.726	0.730	0.868	0.872

In Table 18 we present the probability that each of the four choice is correct. To calculate the probability of a solution being correct, we must maintain the relative magnitude of the chi-squareds for each of the four cases, as we have done in the chi-squared graphs. We are then quantifying that the better the fit, the smaller the chi-squared. In marginalizing from *N* parameters to *N*-1 parameters we are making the assumption that the likelihood function for *N* parameters (not necessarily normalized) is given in terms of the *N*-parameter chi-squared function we have calculated by fitting our model to the data.

$$\mathcal{L}\,(a_1, \ldots, a_n) \equiv \exp\,\{-\chi^2\,(a_1, \ldots, a_n)/2\} \tag{68}$$

The assumption being made is that $\mathcal{L}$ is a probability distribution. Practitioners do not mention it, but this is a Bayesian approach and is not unique. For a given parameter a_i, you are free to choose a prior. The practice is to choose a parameter and take the prior to be a constant.

Without any additional assumptions, when you are down to $N = 1$ and four cases you simply marginalize one more time. You calculate $\mathcal{L}(a)$ from $\chi(a)$ and if you have maintained the relative magnitudes for $\chi_i(a)$, $i = 1,4$, the number $N_i(a) \equiv \int da\ \mathcal{L}_i(a)$ is the probability that case i is correct once you normalize by dividing by $\sum_{i=1}^{4} N_i(a)$. Notice that this is not ambiguous if you have no correlations or if you have Gaussian statistics.

Table 18. Percent probability of being the true solution for each of the four solutions.

Mass Hierarchy	Sign of θ_{13}	Probability of Being True Solution
Normal	Positive	58.6 %
Normal	Negative	7.2 %
Inverse	Positive	6.3 %
Inverse	Negative	27.9 %

Although the normal hierarchy, positive θ_{13} solution is preferred, this is still at a statistically insignificant level (58.6% probability of correctness). However, all three analyses of each of the three mixing parameters we examined agreed on {NH, $+\theta_{13}$} being the preferred solution, showing good convergence. The next best solution is the {IH, $-\theta_{13}$} solution, the symmetry partner to the best fit solution. The symmetry is broken into individual cases by matter effects but its presence is clear.

CHAPTER V

CONCLUSIONS

In this chapter we present some concluding remarks and discuss our suggestions for how to build on the work presented here as well as what the research presented herein implies for the analysis of upcoming neutrino oscillation data.

Summary: Indications from the Alternative Analysis Paradigm

In this work we have used an alternative paradigm, allowing the bounds on the mixing angle θ_{13} to roam from $-\pi/2$ to $+\pi/2$, in order to analyze the world's neutrino oscillation data. Throughout we used a full, exact, calculation of the three-neutrino oscillation probabilities. This allowed us to extract values for the mixing parameters θ_{13}, θ_{23}, and Δm^2_{32} as well as to seek hints of the neutrino mass hierarchy using the most recent MINOS, T2K, Daya Bay, and RENO data as well as constraints on θ_{23} from Super-Kamiokande data.

Using this analysis paradigm to study neutrino oscillation data highlighted the existence of four distinct solutions in the case of *CP*-conservation, one for each sign of θ_{13} and neutrino mass hierarchy combination. This represents a thorough analysis in the *CP*-conservation framework that allows the chi-squared values for each case to be presented and maintains their relative value. The relative values allow the extraction of the probability of each of the four cases being correct. This is in contrast to the traditional presentation in the literature of only two solutions in the *CP*-conserving picture, one for each hierarchy assuming θ_{13} is positive and setting δ_{CP} to 0. Using the traditional bounds, a thorough *CP*-conserving analysis must include one solution each for each mass hierarchy and for $\delta_{CP} = 0$ and π and to extract a quantitative estimate of the preference for a particular hierarchy since the relative values of the chi-squareds need to be maintained.

Furthermore, using this alternative analysis paradigm to explore the oscillation probabilities led to the discovery of a broken four-fold symmetry in the limit of $\theta_{13} = 0$. The symmetry is broken by non-zero θ_{13} into two, two-fold symmetries. This symmetry is the simultaneous interchange of hierarchy and the sign of θ_{13}. This symmetry is then broken further by matter effects. Note that to understand this symmetry, one needs to include all four solutions. It is this fact that cements our preference for having the bounds on θ_{13} extend from $-\pi/2$ to $+\pi/2$.

We find that long baseline disappearance data ($P_{\mu\mu}$) show a small sensitivity to hierarchy and sign θ_{13}. The hierarchy sensitivity was pointed out by the T2K collaboration [44]. This effect does not satisfy the above symmetry. The symmetry applies to the long baseline appearance ($P_{\mu e}$) data, the larger symmetry breaking effect. The conclusions of this work are contained in Table 16 and Table 18, the extracted mixing parameters and the probabilities that each of the four cases is the correct one. Note that each of the four cases yields a separate, non-overlapping solution. This allows us to add probabilities. Thus the symmetry pair {NH, $+\theta_{13}$} + {IH, $-\theta_{13}$} is 58.6% + 27.9% = 86.5% probable to be the correct symmetry pair, with the other pair {NH, $-\theta_{13}$} + {IH, $+\theta_{13}$} is 7.2% + 6.3% = 13.5% likely to be correct.

Although broken, the presence of the symmetry in the final results tells us that the dominant information in the T2K appearance experiment is the spectral information. Future data, in order to distinguish between the individual cases within a pair, will have to improve on the knowledge of the absolute magnitude of the data. Furthermore, we find that positive θ_{13} is preferred over negative θ_{13} by 64.9% to 35.1%. Most interestingly, the normal hierarchy is preferred over the inverse hierarchy by 65.8% to 34.2%.

Other Avenues for Continued Research

We now turn to discussing possible lines of further research in the broader field of neutrino oscillation phenomenology, as they relate to the global analysis presented here.

Gather Mass Hierarchy Data

Gathering additional insight into the correct neutrino mass hierarchy is still an essential goal of the field. Within our analysis paradigm, identifying the correct mass hierarchy combined with knowing the preferred pair of solutions would then automatically constrain indications for *CP*-violation. The NOνA long baseline accelerator experiment has recently begun running and will soon be producing data. This experiment's extended baseline, through the earth's mantle, means it has strong matter effects and hence is sensitive to both hierarchy effects and the *CP*-phase. Therefore, we look forward to being able to include this data set in future work using either the alternative analysis paradigm presented here or in more traditional analysis frameworks.

Gather *CP*-Phase Data

Any insight into the possible magnitude of the *CP*-phase would be invaluable to implementing future symmetry paradigm analyses. Again, similarly to the situation with mass hierarchy information, in our analysis paradigm knowledge about the *CP*-phase combined with knowledge of θ_{13} would constrain the possible neutrino mass hierarchy. In particular, much as with θ_{13} just ten years ago, we are encouraged as a field to begin trying to answer the question, is the *CP*-phase non-zero? Any such indications will be crucial information to help determine the correct mass hierarchy, regardless of the analysis paradigm used, since matter hierarchy effects and *CP*-phase effects are easily convoluted in an analysis of the data. This implies that one possible avenue of research is to pursue treating the *CP*-phase not as a tangential parameter to be marginalized or floated, but as the primary parameter to be fitted in future global analyses. This is another area of research we are actively engaged in as we are currently working to extend the treatment presented here to include δ_{CP} as an additional fourth mixing parameter fitted in the global analysis.

Address Speculative Fundamental Questions

On a more theoretical level, it would be insightful to examine how the mass hierarchy is implemented in matter effects in order to ensure that the correct physics is extrapolated. For example, answering the question, Does and/or should the sign of matter potential terms change under a change in the neutrino mass hierarchy?, particularly in approximate expansion equations sometimes used to analyze oscillation data, is crucial to correctly implementing the analysis paradigm presented here in a study of the oscillation data. It would also be very interesting to attempt to trace the source of the broken symmetry found in the $P_{\mu e}$ oscillation probability. Since this is the first major work using the symmetry analysis paradigm there is a lack of theoretical groundwork, including determining whether or not the vacuum symmetry is generated by some fundamental physical symmetry of either the mixing matrix or the mass matrix and if so how it is broken by large nonzero θ_{13}.

Last Remarks: Future Data and the Alternative Analysis Paradigm

Given the convenience and ease of using the bounds convention implemented in this work and the ability to generate four hypotheses that can be cleanly tested, we see it as a valuable next step for the field to consider analyzing experimental results using the symmetry-sensitive analysis paradigm discussed here, in addition to more traditional analyses methods. This essentially doubles the amount of information gathered from the data with minimal adaption to accommodate the new analysis mode. It also permits a big picture view of whether or not different analysis approaches converge to similar answers, a crucial guide to extracting mixing parameter values based on small effects as well as a being a measure of the robustness of various interpretations of the data. In other words, we find that using an alternative analysis paradigm provides yet another useful tool for fully exploring the world's neutrino oscillation data and we look forward to using it as a probe of future oscillation data in the hunt to complete the picture of neutrino oscillation phenomenology.

APPENDICES

For documentation purposes we present in the following Appendices a number of technical details relating to this work including additional figures and tables of inputs, which while completing the picture present in the main body of this work, are likely of interest only to the reader seeking particular technical details.

APPENDIX A

Re-Framing the Analysis Paradigm: Figures of the Oscillation Probability

Here we present, in alphabetical order, oscillation probability plots for all the experiments included in this work. These are for the full, exact, three-flavor oscillation probability in matter (assuming one constant density layer), over the entire energy range accessible to the experiment, in all cases. In Table 19 we give the inputs used for all plots alike. In Table 20 we give experiment-specific inputs used to generate the plots. We show the full energy range here, for thoroughness. For Super-Kamiokande plots are reproduced from our previously published work [61]. The oscillation probabilities are plotted differently to the other experiments as Super-K does not have a fixed L or E, but rather a variable L/E making it extremely difficult to plot it in its entirety. However, the reproduced plots shows the main features highlighted in this work, namely, the existence of four solutions and a sensitivity to linear and hierarchy effects. For all plots, except Super-K, the curves are as follows: blue (solid) is NH and positive θ_{13}; green (dash) is IH and negative θ_{13}; orange (dot-dash) is NH and negative θ_{13}; and red (dot) is IH and positive θ_{13}.

Table 19. Table of inputs used in all oscillation probability plots.

Parameter	Value
θ_{12}	0.592 rads
θ_{13}	0.157 rads
θ_{23}	0.785 rads
δ_{CP}	0.0 rads
Δm_{21}^2	7.50×10^{-5} eV^2
Δm_{32}^2	2.32×10^{-3} eV^2
Δm_{31}^2	$\Delta m_{21}^2 + \Delta m_{32}^2$
matter density	2.6 g/cm^3

Table 20. Table of experimental inputs used for oscillation probability plots.

Experiment	Baseline L	Energy Range E
Daya Bay	1042.5 m	1×10^{-4} – 12.0 MeV
MINOS	735 km	1×10^{-3} – 10.0 GeV
RENO	1089 m	1×10^{-4} – 12.0 MeV
T2K	295 km	1×10^{-3} – 2.0 GeV

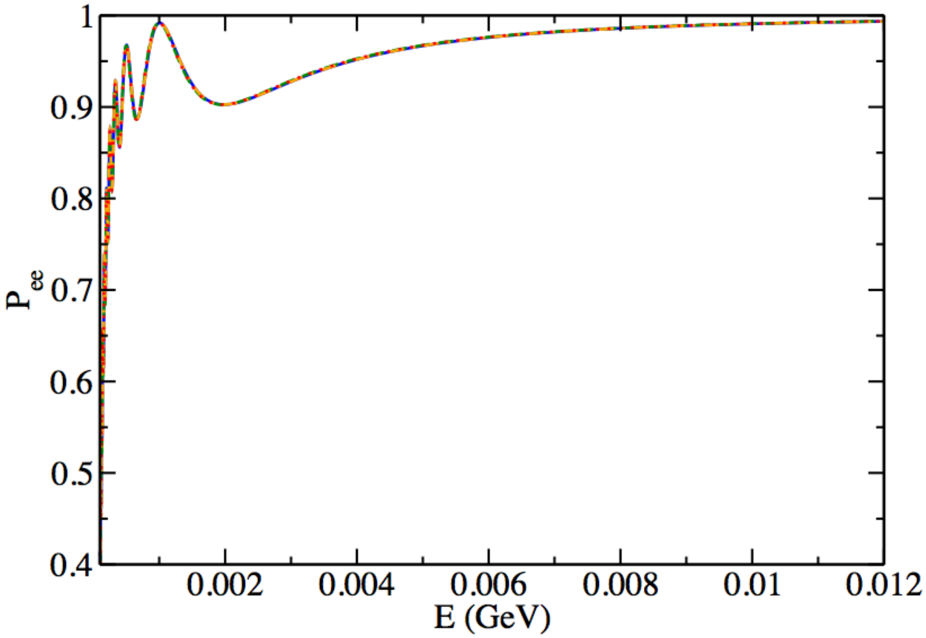

Figure 24. Four solutions for Daya Bay antineutrino disappearance probability. The curves are as follows: blue solid is NH and positive θ_{13}; green dash is IH and negative θ_{13}; orange dot-dash is NH and negative θ_{13}; and red dot is IH and positive θ_{13}.

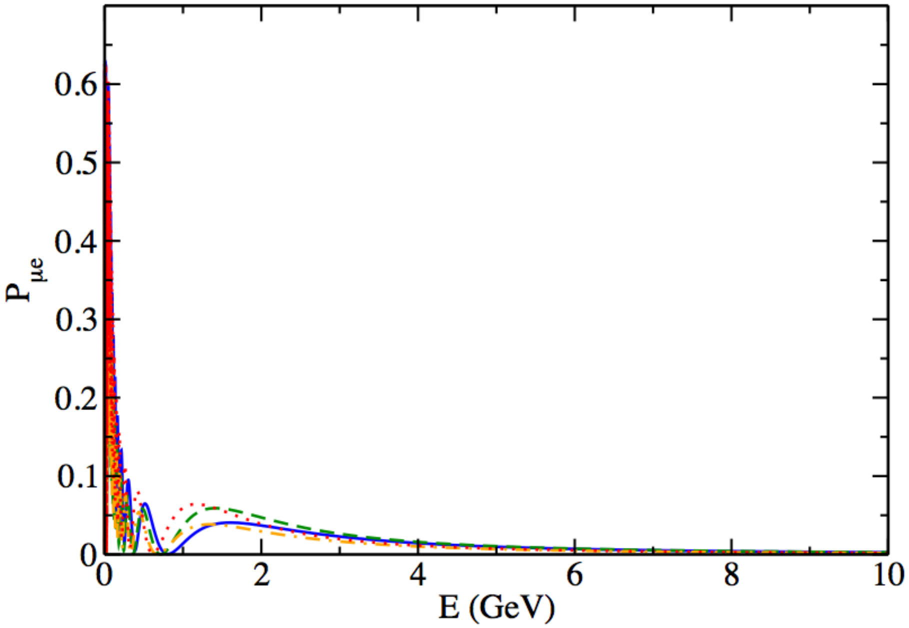

Figure 25. Four solutions for MINOS antineutrino appearance probability. The curves are as follows: blue solid is NH and positive θ_{13}; green dash is IH and negative θ_{13}; orange dot-dash is NH and negative θ_{13}; and red dot is IH and positive θ_{13}.

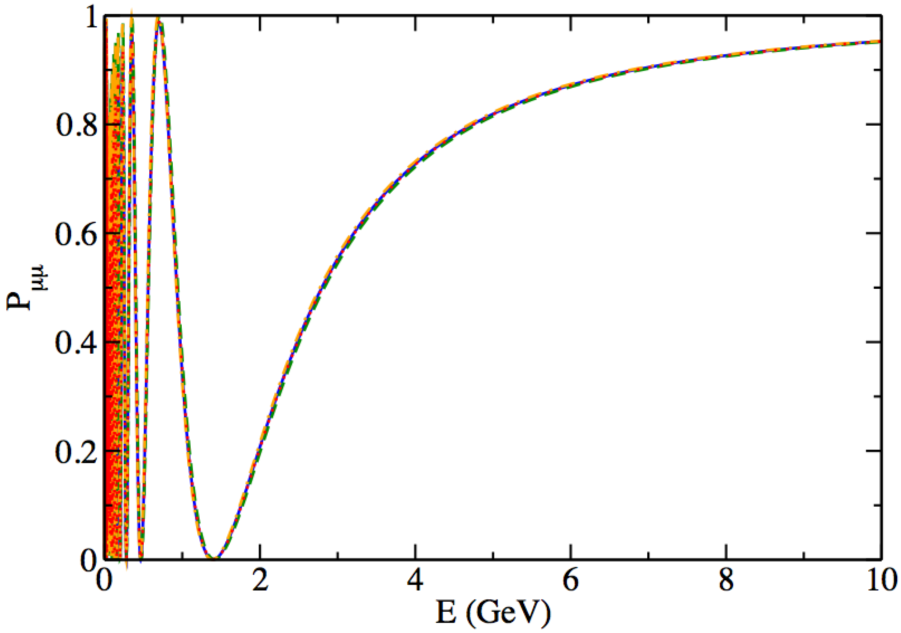

Figure 26. Four solutions for MINOS antineutrino disappearance probability. The curves are as follows: blue solid is NH and positive θ_{13}; green dash is IH and negative θ_{13}; orange dot-dash is NH and negative θ_{13}; and red dot is IH and positive θ_{13}.

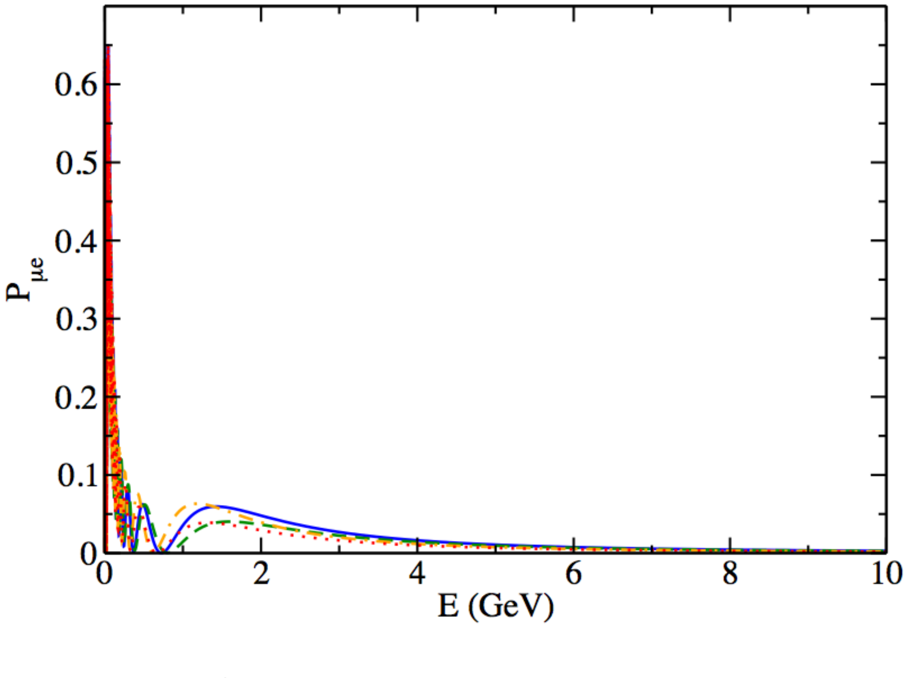

Figure 27. Four solutions for MINOS neutrino appearance probability. The curves are as follows: blue solid is NH and positive θ_{13}; green dash is IH and negative θ_{13}; orange dot-dash is NH and negative θ_{13}; and red dot is IH and positive θ_{13}.

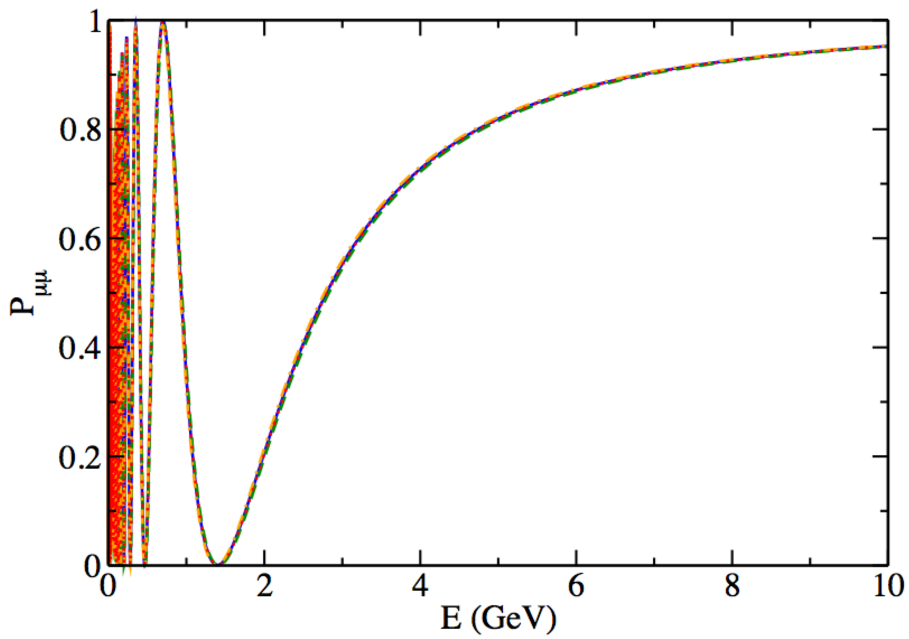

Figure 28. Four solutions for MINOS neutrino disappearance probability. The curves are as follows: blue solid is NH and positive θ_{13}; green dash is IH and negative θ_{13}; orange dot-dash is NH and negative θ_{13}; and red dot is IH and positive θ_{13}.

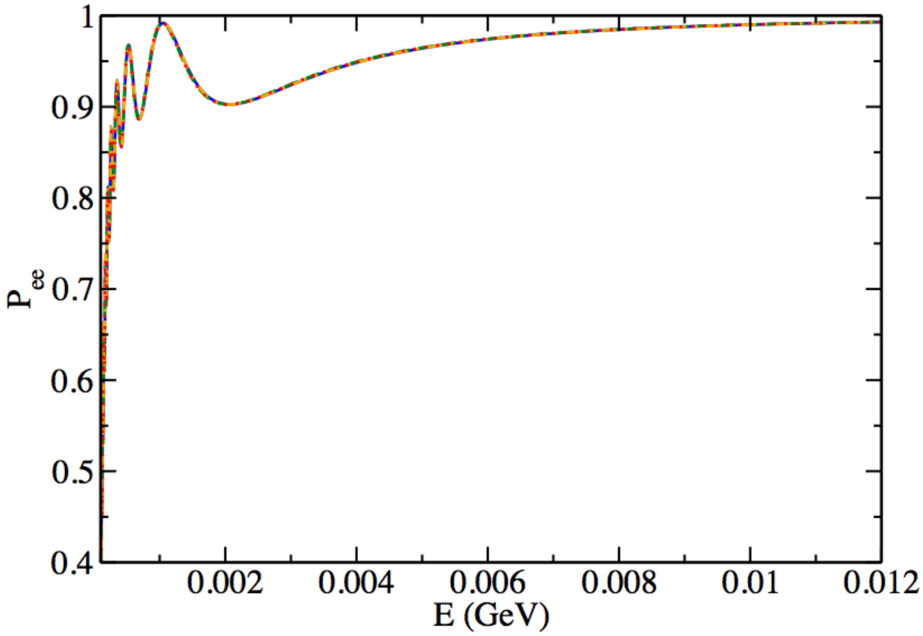

Figure 29. Four solutions for RENO antineutrino disappearance probability. The curves are as follows: blue solid is NH and positive θ_{13}; green dash is IH and negative θ_{13}; orange dot-dash is NH and negative θ_{13}; and red dot is IH and positive θ_{13}.

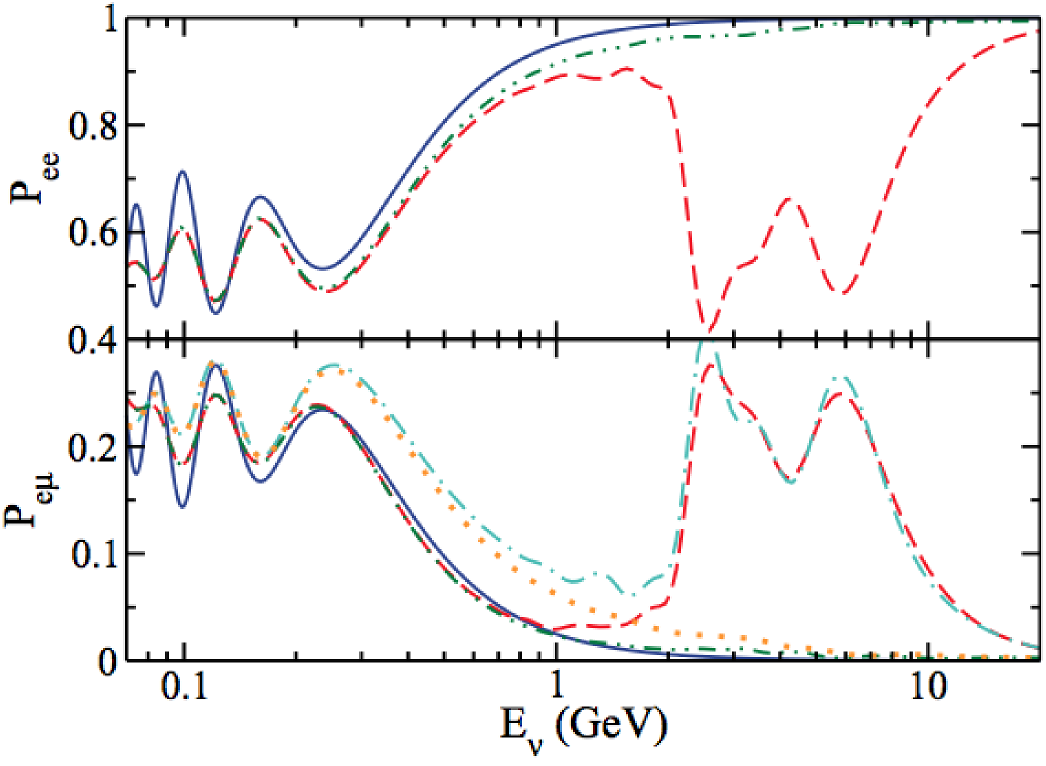

Figure 30. "The oscillation probabilities P_{ee} and $P_{e\mu}$ vs neutrino energy for [earth's-diameter crossing neutrinos] of the Super-K experiment…The (blue) solid curves are for both hierarchies and for $\theta_{13} = 0$; the (red) dashed curves are for the NH and $\theta_{13} = +0.15$; the (green) dot-dot-dashed curves are for the IH and $\theta_{13} = +0.15$. For $P_{e\mu}$, the (turquoise) dot-dashed curve is the NH and $\theta_{13} = -0.15$; the (orange) dotted curve is the IH and $\theta_{13} = -0.15$." Reproduced from Escamilla-Roa *et al.* [61].

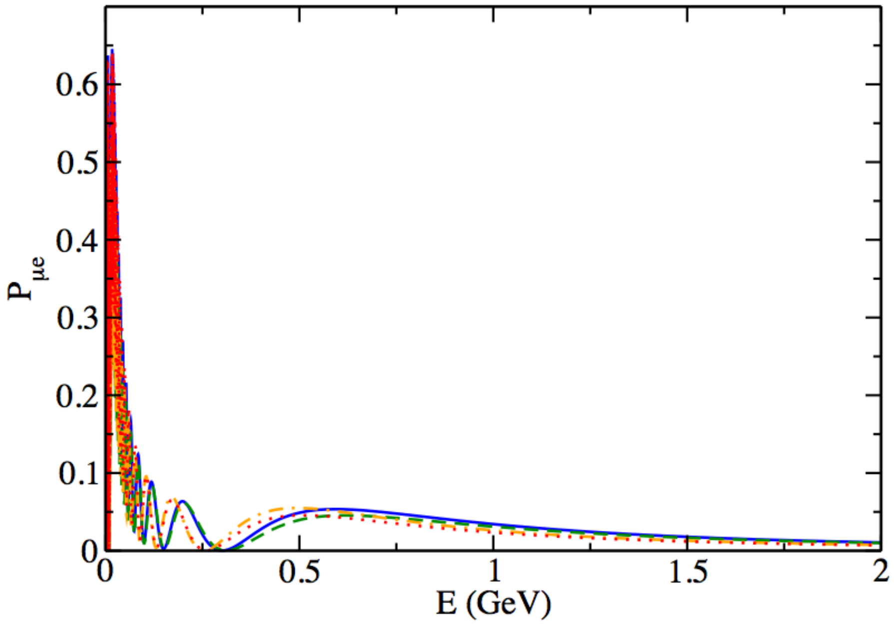

Figure 31. Four solutions for T2K neutrino appearance probability. The curves are as follows: blue solid is NH and positive θ_{13}; green dash is IH and negative θ_{13}; orange dot-dash is NH and negative θ_{13}; and red dot is IH and positive θ_{13}.

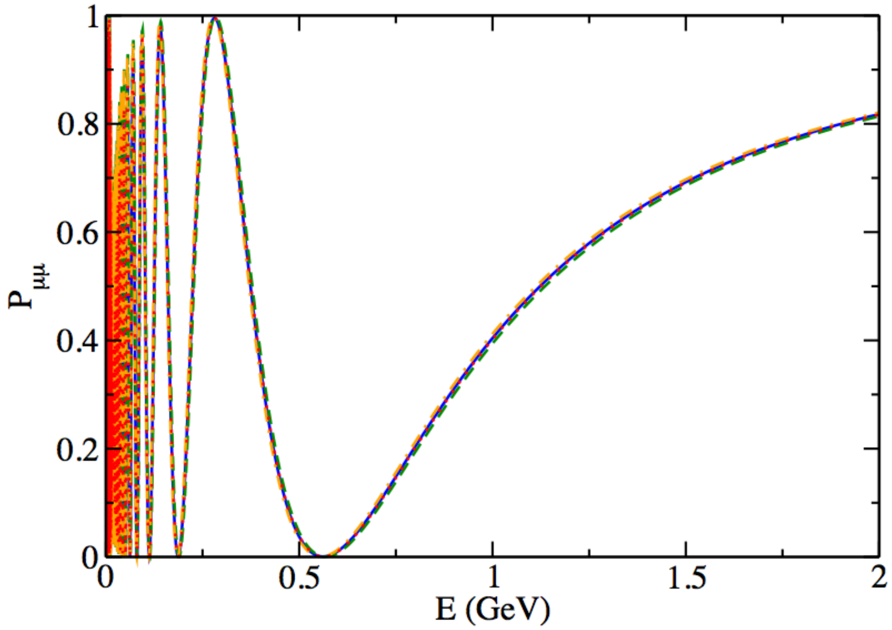

Figure 32. Four solutions for T2K neutrino disappearance probability. The curves are as follows: blue solid is NH and positive θ_{13}; green dash is IH and negative θ_{13}; orange dot-dash is NH and negative θ_{13}; and red dot is IH and positive θ_{13}.

APPENDIX B

Technical Analysis: Calibration Oscillation Probabilities

All reproduction codes, except for Super-K, utilized neutrino oscillation probabilities whose use was implied by, inferred from, or stated in published articles, dissertation, talks, and pre-prints. For reference, we list the oscillation probabilities initially used to match codes to published results. Experiments are listed in alphabetical order.

Daya Bay [10]

$$\begin{aligned} P_{\bar{\nu}_e\rightarrow\bar{\nu}_e} = 1 - {} & \cos^4\theta_{13}\sin^2 2\theta_{12}\sin^2\Delta_{21} \\ & - \sin^2 2\theta_{13}\left(\cos^2\theta_{12}\sin^2\Delta_{31} + \sin^2\theta_{12}\sin^2\Delta_{32}\right) \end{aligned} \tag{69}$$

where

$$\Delta_{ji} \equiv 1.267\Delta m_{ji}^2\left(\text{eV}^2\right)\left[\frac{L(\text{m})}{E(\text{MeV})}\right] \tag{70}$$

$$\sin^2\Delta_{ee} \equiv \cos^2\theta_{12}\sin^2\Delta_{31} + \sin^2\theta_{12}\sin^2\Delta_{32} \tag{71}$$

such that the parameter extracted was $\left|\Delta m_{ee}^2\right|$.

MINOS Antineutrino Disappearance [74]

$$P_{\nu_\mu\rightarrow\nu_\mu} = 1 - \sin^2 2\bar{\theta}\sin^2\left(\frac{1.267\Delta\bar{m}^2\left[\text{eV}^2\right]L[\text{km}]}{E[\text{GeV}]}\right) \tag{72}$$

such that the parameters extracted were $\sin^2 2\bar{\theta}$ and $\left|\Delta\bar{m}^2\right|$.

MINOS Neutrino Appearance [67]

$$
\begin{aligned}
P_{\mu e} = {} & s_{23}^2 \frac{\sin^2 2\theta_{13}}{C_{13}^2} \sin^2 C_{13}\Delta \\
& + c_{23}^2 \frac{\sin^2 2\theta_{12}}{C_{12}^2} \sin^2 \alpha C_{12}\Delta \\
& - 2\alpha s_{12}^2 s_{23}^2 \frac{\sin^2 2\theta_{13}}{C_{13}^2} \sin C_{13}\Delta \left[\Delta \frac{\cos C_{13}\Delta}{C_{13}} (1\text{-}A \cos 2\theta_{13})\text{-}A \frac{\sin C_{13}\Delta}{C_{13}} \frac{(\cos 2\theta_{13}\text{ -}A)}{C_{13}}\right] \\
& + \alpha s_{13} \sin 2\theta_{12} \sin 2\theta_{23} \frac{\sin C_{13}\Delta}{A C_{13}^2} \times \\
& \quad \{\cos \delta \, [C_{13} \sin(1+A)\Delta\text{-} (1\text{-}A \cos 2\theta_{13}) \sin C_{13}\Delta]\text{-}\ C_{13} \sin \delta \, [\cos C_{13}\Delta - \cos(1+A)\Delta]\} \\
& - s_{13} \frac{\sin 2\theta_{12}}{C_{12}} \sin 2\theta_{23} \frac{(1\text{-}\alpha) \sin \alpha C_{12}\Delta}{\left(1+A\text{-}\alpha+A\alpha c_{12}^2\right)} \times \\
& \quad \left\{\sin \delta \, [\cos \alpha C_{12}\Delta - \cos(A+\alpha\text{-}2)\Delta] + \cos \delta \left[\sin(A+\alpha\text{-}2)\Delta - \sin \alpha C_{12}\Delta \right.\right. \\
& \qquad \left.\left. \times \left(\frac{\cos 2\theta_{12} - (A/\alpha)}{C_{12}} - \frac{\alpha A C_{12}}{2(1\text{-}\alpha)} \frac{\sin^2 2\theta_{12}}{C_{12}^2}\right)\right]\right\} \\
& - 2\alpha s_{13} \sin 2\theta_{12} \sin 2\theta_{23} \cos(\Delta+\delta) \frac{\sin A\Delta}{A} \frac{\sin(A\text{-}1)\Delta}{(A\text{-}1)}
\end{aligned}
\tag{73}
$$

where

$$\alpha \equiv \frac{\Delta m_{21}^2}{\Delta m_{31}^2} \tag{74}$$

$$\Delta \equiv \frac{\Delta m_{31}^2 L}{4E} \tag{75}$$

$$A \equiv \frac{VL}{2\Delta} \tag{76}$$

$$C_{12} \equiv \sqrt{\sin^2 2\theta_{12} + [\cos 2\theta_{12}\text{-}(A/\alpha)]^2} \tag{77}$$

$$C_{13} \equiv \sqrt{\sin^2 2\theta_{13} + (A - \cos 2\theta_{13})^2} \tag{78}$$

such that the parameter extracted was $2\sin^2\theta_{23}\sin^2 2\theta_{13}$.

MINOS Neutrino Disappearance [73]

$$P_{\nu_\mu \to \nu_\mu} = 1 - \sin^2 2\theta \sin^2\left(\frac{\Delta m^2 L}{4E}\right) \tag{79}$$

such that the parameters extracted were $\sin^2 2\theta$ and $\left|\Delta m^2\right|$.

RENO [11]

$$P_{survival} \approx 1 - \sin^2 2\theta_{13} \sin^2\left(\frac{1.267\Delta m_{31}^2 L}{E}\right) \tag{80}$$

such that the parameter extracted was $\sin^2 2\theta_{13}$.

T2K Appearance [75]

The full, exact, three-flavor oscillation probability with matter effects was used, see Chapter I Eqs. (7)-(9), such that the parameter extracted was $\sin^2 2\theta_{13}$.

T2k Disappearance [76]

The full, exact, three-flavor oscillation probability with matter effects was used, see Chapter I, Eqs. (7)-(9), such that the parameters extracted were $\sin^2\theta_{23}$ and Δm_{32}^2 (NH), Δm_{31}^2 (IH).

APPENDIX C

Technical Analysis: Tables of Code Inputs

In this Appendix we compile tables of all the numerical inputs used in the code to reproduce published experimental results as discussed in Chapter III. Note, for all cases the *CP*-phase was set to $\delta_{CP} = 0.0$ rads (*CP*-conserving) and the earth's matter potential used was $V = 3.78\times10^{-14}\,\rho \cdot \mathrm{eV}^2$, where ρ is the earth's matter density in g/cm^3. Due to the large number of data sets, we do not list values for items such as mixing parameters, baselines, energies, or data points, which were taken directly from values listed in the relevant publications. Here we only list those items which would be needed to reproduce our analysis and which were determined by us and not published elsewhere, such as the errors included, the scale factors added, the type of χ^2 equation used and so on. We present the experiments in alphabetical order. Note, scale factors and errors are presented in decimal form, not percent, throughout.

Table 21. Daya Bay input parameters used in analysis.

Electron Antineutrino Disappearance

- Data taken from [10]: Figure 4, top panel
- All data points used
- Used Gaussian χ^2
- Scaled signal per bin by factor $r_{flux} = 1.013$
- Included systematic errors:
  - Flux $(1-P_{ee})$ $\sigma_{flux} = 0.085$
- Benchmarks matched: full fit; best fit $\sin^2 2\theta_{13}$ and 68.3% C.L. lower and upper bounds

Table 22. MINOS antineutrino disappearance input parameters used in analysis.

Muon Antineutrino Disappearance

- Data taken from [74]: Figure 3
- Used 22 out of 13 bins; dropped first bin with 0 counts
- Used Poisson χ^2
- Scaled signal per bin by factor r_{flux} = nuisance parameter fitted by minimization routine
- Overall energy scale included, $E_{scale} = 1.02$
- Included systematic errors
  - Flux $\sigma_{flux} = 1.00$
  - Energy $\sigma_{Energy} = C\sqrt{E} = 0.27\sqrt{E}$
- Calibrated prediction to match best fit result
  - $Theory$ = predicted signal
  - r_f = scale factor to fit minimum = 0.975
  - b_f = background counts per bin
  - $P_{e\mu}^{av}$ = full, exact, three-neutrino oscillation probability in matter per bin
  - $P_{e\mu}^{cal}$ = calculated for published best fit mixing parameters

$$Theory = r_f \times b_f \times \frac{P_{e\mu}^{av}}{P_{e\mu}^{cal}}$$

- Gauss-Hermite integration (Gaussian E distribution) used to calculate predicted signal per bin
- Benchmarks matched: best fit $\sin^2 2\overline{\theta}$ and $\Delta\overline{m}^2$

Table 23. MINOS neutrino appearance input parameters used in analysis.

Electron Neutrino Appearance

- Data taken from [41]: Figure 2
- All data points used (used first 4 bins and merged last 3 bins as in Figure 2, bottom panel)
- Used Poisson χ^2
- Scaled signal per bin by factor r_{flux} = nuisance parameter fitted by minimization routine
- Included systematic errors:
    - Flux $\sigma_{flux} = 0.319$
- Calibrated prediction to match best fit result
    - $Theory$ = predicted signal
    - r_f = scale factor to fit minimum = 1.46
    - N_{cal} = calibration factor for each bin from Figure 5 histogram
    - $P_{e\mu}^{av}$ = full, exact, three-neutrino oscillation probability in matter per bin
    - $P_{e\mu}^{cal}$ = calculated for NH and positive θ_{13}

$$Theory = r_f \times N_{cal} \times \frac{P_{e\mu}^{av}}{P_{e\mu}^{cal}}$$

- Benchmarks matched: best fit $\sin^2 2\theta_{13}$ and 90% C.L. lower and upper bounds

Table 24. MINOS neutrino disappearance input parameters used in analysis.

Muon Neutrino Disappearance

- Data taken from [73]: Figure 1, top left panel
- All data points used
- Used Poisson χ^2
- Scaled signal per bin by factor r_{flux} = nuisance parameter fitted by minimization routine
- Overall energy scale included, $E_{scale} = 1.04$
- Included systematic errors
    - Flux $\sigma_{flux} = 1.00$
    - Energy $\sigma_{Energy} = \left(A/\sqrt{E} + BE^{bin}_{midpoint}\right)C = \left(0.510/\sqrt{E} + 0.02E^{bin}_{midpoint}\right)0.32$
- Calculated predicted signal using Monte Carlo no oscillation prediction
    - $Theory$ = predicted signal
    - r_f = scale factor to fit minimum = 1.045
    - $MC_{no\ osc}$ = published far detector Monte Carlo no oscillation prediction
    - $P_{\mu\mu}$= full, exact, three-neutrino oscillation probability in matter per bin
    - b_f = background counts per bin

$$Theory = r_f \times MC_{no\ osc} \times P_{\mu\mu} + b_f$$

- Gauss-Hermite integration (Gaussian E distribution) used to calculate predicted signal per bin
- Benchmarks matched: best fit $\sin^2 2\theta$ and Δm^2; 7 points from the 90% C.L. solid allowed region curve in Figure 3

Table 25. RENO input parameters used in analysis.

Electron Antineutrino Appearance

- Data taken from [11]: Figure 4, top panel
- All data points used
- Used Gaussian χ^2
- Calculated theoretical signal by averaging spectral data calculation from Figure 4, top panel, for each detector at weighted baselines given in Figure 3, bottom panel
- Scaled signal per bin by factor $r_{flux} = 0.01658$
- Included systematic errors:
    - Near detector $\sigma_{\mathrm{ND}} = 0.01360$
    - Far detector $\sigma_{\mathrm{FD}} = 0.01129$
- Benchmarks matched: Figure 3, top panel, best fit $\sin^2 2\theta_{13}$ and upper and lower bounds at $\sin^2 2\theta_{13} = 0.00$ and 0.20

Table 26. Super-K input parameters used in analysis.

Super-K Restriction on θ_{23} and Δm^2_{32}

- Data fitted [76]: blue allowed region in Figure 4
- Represented restriction using a normal data distribution:

$$\chi^2 = \left(\frac{\Delta m^2_{32,dist} - \Delta m^2_{32,fit}}{\sigma_{\Delta m^2}}\right)^2 + \left(\frac{\sin^2 2\theta^{dist}_{23} - \sin^2 \theta^{fit}_{23}}{\sigma_\theta}\right)^2$$

- Included systematic errors:
    - Mixing angle $\sigma_\theta = 0.0326$
    - Mass-splitting $\sigma_{\Delta m^2} = 0.2352\times10^{-3}$

Table 27. T2K neutrino appearance input parameters used in analysis.

Electron Neutrino Appearance

- Data taken from [75]: Figure 4
- Used 22 of 25 data points (for published fit region below 1250 MeV); dropped first 3 bins
- Used Poisson χ^2
- Scaled signal per bin by factor r_{flux} = nuisance parameter fitted by minimization routine
- Included systematic errors
    - Flux $\sigma_{flux} = 0.099$
- Benchmarks matched: best fit $\sin^2 2\theta_{13}$ and upper and lower bounds at 68% C.L.

Table 28. T2K neutrino disappearance input parameters used in analysis.

Muon Neutrino Disappearance

- Data taken from [76]: Figure 2
- Used 16 out of 18 bins; dropped first 2 bins with 0 counts
- Used Poisson χ^2
- Scaled per bin and treated as nuisance parameter fitted by minimization routine
    - r_{flux} = overall norm multiplying predicted signal
    - r_{Ebin} = multiplies energy per bin
- Overall energy scale included, $E_{scale} = 1.07$
- Gaussian energy resolution function included
    - $\sigma_{Energy} = C + A\sqrt{E} = 0.105 + 1.06\sqrt{E}$
- Published analysis ran over two disconnected regions ($\sin^2 2\theta_{23} < \pi/4$ and $\sin^2 2\theta_{23} > \pi/4$); ran our analysis over one singly connected region ($\theta_{23} = [0, \pi/2]$)
- Included systematic errors
    - Flux $\sigma_{flux} = 0.55$
    - Energy $\sigma_{Energy} = 0.005$
- Benchmarks matched: best fit $\sin^2 \theta_{23}$ and $\left|\Delta m^2_{32}\right|$, asymmetric shape of θ_{23} bounds and elliptical shape of 2-D allowed region in θ_{23}-$\left|\Delta m^2_{32}\right|$

REFERENCES

[1] B. Pontecorvo, Mesonium and anti-mesonium, Sov. Phys. JETP 6, 429 (1957) [Zh. Eksp. Teor, Fiz 33, 549-551 (1957)].

[2] B. Pontecorvo, Neutrino Experiments and the Problem of Conservation of Leptonic Charge, Sov. Phys. JETP 26, 984 (1968) [Zh. Eksp. Teor, Fiz 53, 1717 (1967)].

[3] C. Giunti and C. W. Kim, *Fundamentals of Neutrino Physics and Astrophysics*, (Oxford University Press, New York, NY, 2007).

[4] B. Kayser, Neutrino Phenomenology: Part I, lecture given at International Neutrino Summer School (INSS), Blacksburg, VA (2012).

[5] S. P. Mikheev and A. Y. Smirnov, Resonance oscillations of neutrinos in matter, Sov. Phys. Usp. 30, 759-790 (1987).

[6] L. Wolfenstein, Neutrino oscillations in matter, Phys. Rev. D 17, 2369 (1978).

[7] E. Akhmedov, Parametric resonance of neutrino oscillations and passage of solar and atmospheric neutrinos through the earth, Nucl. Phys. B 538, 25-51 (1999).

[8] E. K. Akhmedov, M. Maltoni, and A. Y. Smirnov, 1-3 leptonic mixing and the neutrino oscillograms of the Earth, J. High Energy Phys., 05 (077), 1-47 (2007).

[9] V. Barger, D. Marfatia, and K. Whisnant, Breaking eightfold degeneracies in neutrino *CP* violation, mixing, and mass hierarchy, Phys. Rev. D 65, 073023 (2002).

[10] F. P. An *et al*. (Daya Bay), Spectral Measurement of Electron Antineutrino Oscillation Amplitude and Frequency at Daya Bay, Phys. Rev. Lett. 112, 061801 (2014).

[11] J. K. Ahn *et al*. (RENO), Observation of Reactor Electron Antineutrino Disappearance in the RENO Experiment, Phys. Rev. Lett. 108, 191802 (2012).

[12] Y. Abe *et al.* (Double Chooz), Background-independent measurement of θ_{13} in Double Chooz, arXiv: hep-ex/1401.5981v1 (2014).

[13] P. Adamson *et al.* (MINOS), Search for Muon-Neutrino to Electron-Neutrino Transitions in MINOS, Phys. Rev. Lett. 103, 261802 (2009).

[14] P. Adamson *et al.* (MINOS), Electron Neutrino and Antineutrino Appearance in the Full MINOS Data Sample, Phys. Rev. Lett. 110, 171801 (2013).

[15] K. Abe *et al.* (T2K), Observation of Electron Neutrino Appearance in a Muon Neutrino Beam, Phys. Rev. Lett. 112, 061802 (2014).

[16] Y. Fukuda *et al.* (Super-K), Atmospheric ν_μ / ν_e ratio in the multi-GeV energy range, Phys. Lett. B 335, 237-245 (1994).

[17] R. J. Davis, D. S. Harmer, and K. C. Hoffman (Homestake), Search for neutrinos from the sun, Phys. Rev. Lett. 20, 1205-1209 (1968).

[18] P. Anselmann *et al.* (GALLEX), Solar neutrinos observed by GALLEX at Gran Sasso, Phys. Lett. B 285, 376-389 (1992).

[19] M. Altmann *et al.* (GNO), Complete results for five years of GNO solar neutrino observations, Phys. Lett. B 616, 174-190 (2005).

[20] B. Aharmim *et al.* (SNO), Eelctron energy spectra, fluxes, and day-night asymmetries of ^{8}B solar neutrinos from measurement with NaCl dissolved in heavy-water detector at Sudbury Neutrino Observatory, Phys. Rev. C 72, 055502 (2005).

[21] T. Araki, K. Eguchi, S. Enomoto, *et al.* (KamLAND), Measurement of Neutrino Oscillation with KamLAND: Evidence of Spectral Distortion, Phys. Rev. Lett. 94, 081801 (2005).

[22] D. V. Forero, M. Tortola, and J. W. F. Valle, Global status of neutrino oscillation parameters after Neutrino-2012, Phys. Rev. D 86, 073012 (2012).

[23] J. N. Abdurashitov *et al.* (SAGE), Measurement of the solar neutrino capture rate with gallium metal. III. Results for the 2002-2007 data-taking period, Phys. Rev. C 80, 015807 (2009).

[24] G. Bellini *et al.* (Borexino), Precision Measurement of the ^{7}Be Solar Neutrino Interaction Rate in Borexino, Phys. Rev. Lett. 107, 141302 (2011).

[25] G. L. Fogli, E. Lisi, A. Marrone, *et al.*, Global analysis of neutrino masses, mixings, and phases: Entering the era of leptonic *CP* violation searches, Phys. Rev. D 86, 013012 (2012).

[26] G. L. Fogli, E. Lisi, A. Marrone, *et al.*, Evidence of $\theta_{13} > 0$ from global neutrino data analysis, Phys. Rev. D 84, 053007 (2011).

[27] M. C. Gonzalez-Garcia, M. Maltoni, J. Salvado, *et al.*, Global fit to three neutrino mixing: critical look at present precision, J. of High Energy Phys. 12 (123), 1-23 (2012).

[28] M. H. Ahn *et al.* (K2K), Measurement of Neutrino Oscillation by the K2K Experiment, Phys. Rev. D 74, 072003 (2006).

[29] M. Apollonio *et al.* (Chooz), Limits on Neutrino Oscillations from the CHOOZ Experiment, Phys. Lett. B 466, 415-430 (1999).

[30] A. Piepke (Palo Verde), Final results from the Palo Verde neutrino oscillation experiment, Prog. Part. Nucl. Phys. 48, 113-121 (2002).

[31] Y. Declais, H. de Kerret, B. Lefievre, *et al*. (Bugey 4), Study of reactor anti-neutrino interaction with proton at Bugey nuclear power plant, Phys. Lett. B 338, 383-389 (1994).

[32] Y. Declais, J. Favier, A. Metref, *et al.* (Bugey 3), Search for neutrino oscillations at 15-meters, 40-meters, and 95-meters from a nuclear power reactor at Bugey, Nucl. Phys. B 434, 503-534 (1995).

[33] A. Kuvshinnikov, L. Mikaelyan, S. Nikolaev, *et al.* (ROVNO 4), Measuring the $\overline{\nu}_e + p \rightarrow n + e^+$ cross-section and beta decay axial constant in a new experiment at Rovno NPP reactor, (In Russian), JETP Lett. 54, 253-257 (1991).

[34] G. Vidyakin, V. Vyrodov, Y. Kozlov, *et al.* (Krasnoyarsk), Limitations on the characteristics of neutrino oscillations, JETP Lett. 59, 390-393 (1994).

[35] H. Kwon, F. Boehm, A. Hahn, *et al.* (ILL), Search for neutrino oscillations at a fission reactor, Phys. Rev. D 24, 1097-1111 (1981).

[36] G. Zacek *et al.* (Gosgen), Neutrino Oscillation Experiments at the Gosgen Nuclear Power Reactor, Phys. Rev. D 34, 2621-2636 (1986).

[37] Z. D. Geenwood *et al.* (SRP), Results of a two position reactor neutrino oscillation experiment, Phys. Rev. D 53, 6054-6064 (1996).

[38] A. Afonin, S. Ketov, V. Kopeikin, *et al.* (ROVNO88), A study of the reaction $\overline{\nu}_e + p \rightarrow e^+ + n$ on a nuclear reactor, Sov. Phys. JETP 67, 213-221 (1988).

[39] K. Schreckenbach, G. Colvin, W. Gelletly, *et al.*, Determination of the anti-neutrino spectrum from u-235 thermal neutron fission products up to 9.5-mev, Phys. Lett. B 160, 325-330 (1985).

[40] T. Mueller, D. Lhuillier, M. Fallot, *et al*., Improved Predictions of Reactor Antineutrino Spectra, Phys. Rev. C 83, 054615 (2011).

[41] P. Adamson *et al.* (MINOS), Improved Search for Muon-Neutrino to Electron-Neutrino Oscillations in MINOS, Phys. Rev. Lett. 107, 181802 (2011).

[42] P. Adamson *et al.* (MINOS), Measurement of the Neutrino Mass Splitting and Flavor Mixing by MINOS, Phys. Rev. Lett. 106, 181801 (2011).

[43] P. Adamson *et al.* (MINOS), Measurement of Neutrino and Antineutrino Oscillations Using Beam and Atmospheric Data in MINOS, Phys. Rev. Lett. 110, 251801 (2013).

[44] K. Abe *et al.* (T2K), Precise Measurement of the Neutrino Mixing Parameter θ_{23} from Muon Neutrino Disappearance in an Off-Axis Beam, arXiv: hep-ex/1403.1532v1 (2014).

[45] Y. Abe *et al.* (Double Chooz), Indication of Reactor $\bar{\nu}_e$ Disappearance in the Double Chooz Experiment, Phys. Rev. Lett. 108, 131801 (2012).

[46] Y. Itow, Recent results in atmospheric neutrino oscillations in the light of large θ_{13}, Nucl. Phys. B Proc. Supp. 235-236, 79-86 (2013).

[47] H. Minakata, Phenomenology of future neutrino experiments with large θ_{13}, Nucl. Phys. B Proc. Suppl. 235-236, 173-179 (2013).

[48] K. Nishikawa, Experimental Prospect, Nucl. Phys. B Proc. Suppl. 235-236, 441-447 (2013).

[49] K. Scholberg and F. L. Villante, Oscillations at low energies, Nucl. Phys. B (Proc. Suppl.) 237-238, 352-357 (2013).

[50] A. Yu. Smirnov, Neutrino 2012: Outlook – theory, Nucl. Phys. B (Proc. Suppl.) 237-238, 431-440 (2013).

[51] F. Jediny (NOνA), NOνA neutrino experiment status, J. of Phys.: Conf. Ser. 490, 012019 (2014).

[52] D. J. Ernst, B. K. Cogswell, H. R. Burroughs, *et al.*, Implications of the nonzero θ_{13} for the neutrino mass hierarchy, J. of Phys.: Conf. Series 403, 012040 (2010).

[53] D. J. Ernst, B. K. Cogswell, H. R. Burroughs, *et al.*, Neutrino oscillations: hierarchy question, arXiv: nucl-th/1303.4790v1 (2013).

[54] J. Gluza and M. Zralek, Parameters' domain in three flavour neutrino oscillations, Phys. Lett. B 517, 158-166 (2001).

[55] D. C. Latimer and D. J. Ernst, Physical region for three-neutrino mixing angles, Phys. Rev. D 71, 017301 (2005).

[56] H. Harari and M. Leurer, Recommending a standard choice of Cabibbo angles and KM phases for any number of generations, Phys. Lett. B 181 (1-2), 123-128 (1986).

[57] D. C. Latimer and D. J. Ernst, Analysis of three-neutrino oscillations in the full mixing angle space, arXiv: nucl-th/0404059v4 (2004).

[58] D. C. Latimer and D. J. Ernst, Neutrino oscillations: Measuring θ_{13} including its sign, Phys. Rev. C 71, 062501(R) (2005).

[59] D. C. Latimer and D. J. Ernst, Correlations between θ_{13} and θ_{23} in a very long baseline neutrino oscillation experiment, Phys. Rev. C 72, 045502 (2005).

[60] J. E. Roa, D. C. Latimer, and D. J. Ernst, Atmospheric, Long Baseline, and Reactor Neutrino Data Constraints on θ_{13}, Phys. Rev. Lett. 103, 061804 (2009).

[61] J. Escamilla-Roa, D. C. Latimer, and D. J. Ernst, Impact of hierarchy upon the values of neutrino mixing parameters, Phys., Rev. C 82, 028501 (2010).

[62] B. K. Cogswell, *Implications of accelerator electron neutrino appearance data and revised reactor fluxes for the sign and value of the neutrino mixing angle theta 13*, M.A. Thesis, Fisk University, Nashville, TN, 2011.

[63] J. Escamilla-Roa, D. C. Latimer, and D. J. Ernst, Implications of the Super-K atmospheric, long baseline, and reactor data for the mixing angles θ_{13} and θ_{23}, Phys. Rev. C 81, 015501 (2010).

[64] D. V. Ahluwahlia, Notes on the Kinematic Structure of the Three-Flavor Neutrino Oscillation Framework, Int. J. Mod. Phys. A 12 (28), 5081-5102 (1997).

[65] D. C. Latimer and D. J. Ernst, On the degeneracies of the mass-squared differences for three-neutrino oscillations, Mod. Phys. Lett. A 20 (22), 1663-1672 (2005).

[66] G. J. Feldman and R. D. Cousins, A Unified Approach to the Classical Statistical Analysis of Small Signals, Phys. Rev. D 57, 3873-3889 (1998).

[67] J. A. A. Boehm, *A Measurement of Electron Neutrino Appearance with the MINOS Experiment*, Ph. D. thesis, Harvard University (FERMILAB-THESIS-2009-17, MINOS-DOC-6010), Cambridge, MA, 2009.

[68] W. H. Press, S. A. Teukolsky, W. T. Vetterling, *et al*., Section 10.4: Downhill Simplex Method in Multidimensions, excerpt in *Numerical Recipes in FORTRAN 77: The Art of Scientific Computing*, (Cambridge University Press, Cambridge, 1992).

[69] T. Ohlsson and H. Snellman, Three flavor neutrino oscillations in matter, J. of Math. Phys. 41 (5), 2768-2788 (2000).

[70] J. A. Koziol and M. D. Perlman, Combining Independent Chi-Squared Tests, J. of the Am. Stat. Soc. 73 (364), 753-763 (1978).

[71] J. O. Berger, B. Liseo, and R. L. Wolpert, Integrated Likelihood Methods for Eliminating Nuisance Parameters, Stat. Sci. 14 (1), 1-28 (1999).

[72] H. R. Burroughs, B. K. Cogswell, J. Escamilla-Roa *et al.*, Calculating error bars for neutrino mixing parameters, Phys. Rev. D 85, 068501 (2012).

[73] P. Adamson, *et al.* (MINOS), Measurement of Neutrino and Antineutrino Oscillations Using Beam and Atmospheric Data in MINOS, arXiv: hep-ex/1304.6335v2 (2013).

[74] P. Adamson, *et al.* (MINOS), Improved Measurement of Muon Antineutrino Disappearance in MINOS, Phys. Rev. Lett. 108, 191801 (2012).

[75] K. Abe, *et al.* (T2K), Observation of Electron Neutrino Appearance in a Muon Neutrino Beam, arXiv: hep-ex/1311.4750v1 (2013).

[76] K. Abe, *et al.* (T2K), Measurement of Neutrino Oscillation Parameters from Muon Neutrino Disappearance with an Off-Axis Beam, Phys. Rev. Lett. 111, 211803 (2013).

[77] K. Abe *et al.* (T2K), Precise Measurement of the Neutrino Mixing Parameter θ_{23} from Muon Neutrino Disappearance in an Off-Axis Beam, Phys. Rev. Lett. 112, 181801 (2014).

[78] J. Beringer *et al.* (Particle Data Group), Review of Particle Physics, Phys. Rev. D 86, 010001 (2012).

[79] B. K. Cogswell, D. C. Latimer, and D. J. Ernst (in preparation).

[80] F. Capozzi, G. L. Fogli, E. Lisi, *et al.*, Status of three-neutrino oscillation parameters, circa 2013, Phys. Rev. D 89, 093018 (2014).